Development of Paper-Based Analytical Devices for Low-cost, Rapid and Straightforward Measurement of Components in Human Whole Blood

安価、迅速、簡便なヒト血中成分測定のための ペーパーデバイスの開発

Takeshi Komatsu

Graduate School of Chemical Sciences Engineering

Hokkaido University

Title Development of Paper-Based Analytical Devices for Low-cost, Rapid and Straightforward Measurement of Components in Human Whole Blood

Author Takeshi Komatsu

Degree Doctor of Philosophy (Engineering)

Supervisor Professor Manabu Tokeshi

CONTENTS

CHAPTER 1 General Introduction

1.1 Microfluidic paper-based analytical device

The first paper presenting a sensor substrate was published by Yogoda in 1937 [1]. This report fabricated a paper spot array using a filter paper and hydrophobic paraffin (Fig. 1.1a) and demonstrated colorimetric detection of Ni^{2+} and Cu^{2+} on the paper spot. It further noted that soaking a fixed volume of reagents into paper spots helps to quantitatively determine the target analytes in the sample. In 1949, Müller et al. reported [2] chromatography for the separation of dyes on a microfluidic channel, which was patterned on the filter paper via paraffin wax (Fig. 1.1b). This confined microchannel provided an improved diffusion rate and reduced quantity of reagent. Subsequently, for half a century, research on paper chromatography has been actively conducted [3–14]. The next breakthrough was reported by Whitesides' group in 2007 [15]; they invented patterned paper for potable bioassay (Fig. 1.1c) and, shortly after, defined a microfluidic paper-based analytical device (μPAD) [16–19]. Subsequently, attention towards μPADs has rapidly increased and many researchers around the world have energetically conducted related research and developed various prototype μPADs.

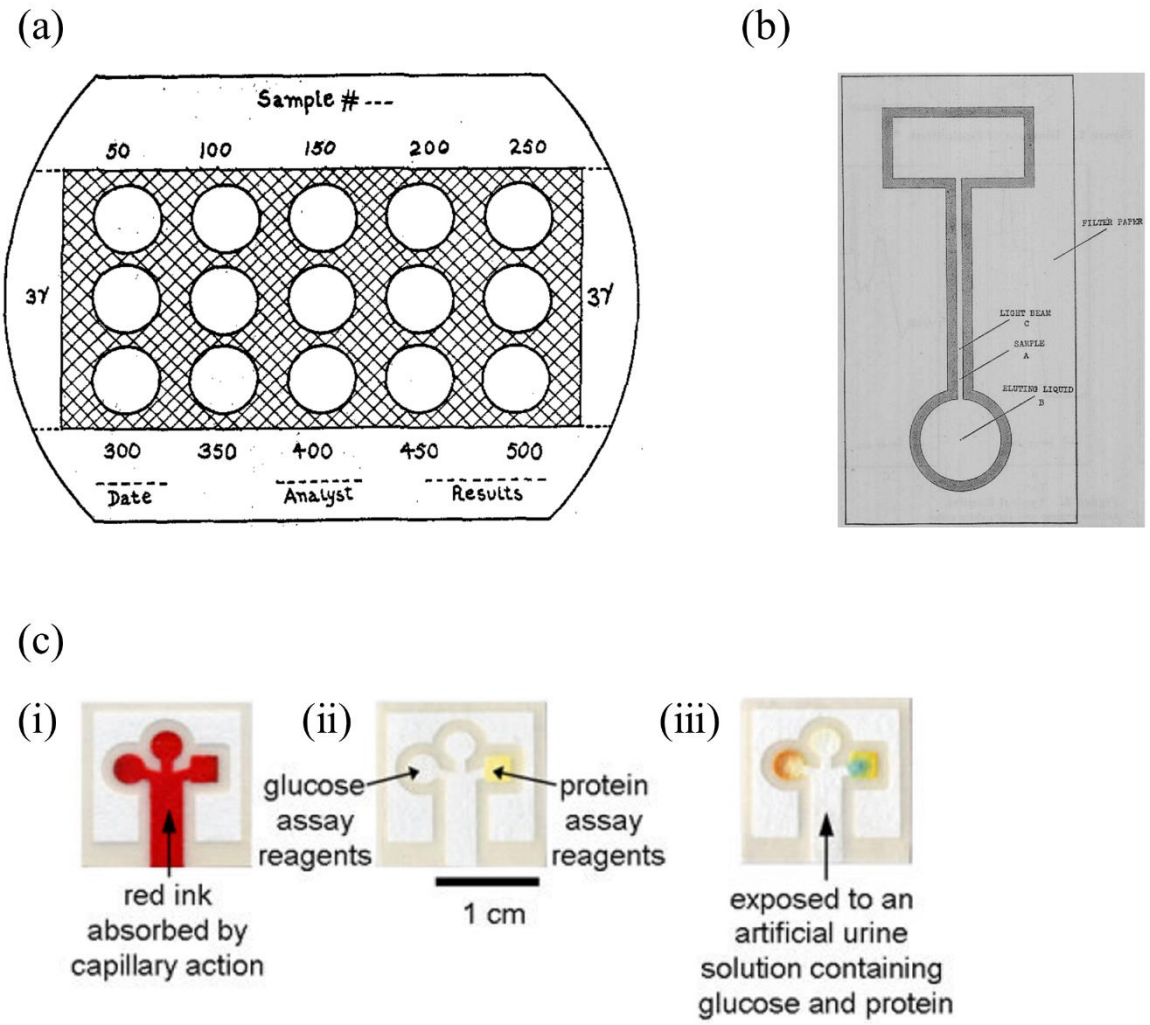

Figure 1.1 History of the use of paper as the sensor material. (a) A paper spot, fabricated with filter paper and paraffin for detection of metal ions by colorimetry. Reprinted with permission from reference [1]. Copyright 1937, American Chemical Society. (b) A microfluidic channel patterned on filter paper for paper chromatography. Reprinted with permission from reference [2]. Copyright 1949, American Chemical Society. (c) First reported microfluidic paper-based analytical device (μPAD) by Whitesides' group: photographs after (i) loading red ink onto the μPAD; (ii) loading detection reagents for glucose and protein onto the μPAD; (iii) detecting glucose and BSA in artificial urine. Reprinted with permission from reference [15]. Copyright 2007, American Chemical Society.

μPADs derive from "miniaturized total chemical analysis systems (μTAS)"; this is a micro/nano biodevice that utilizes semiconductor microfabrication technology, precision synthesis technology, and microfluidic control technology [20–27]. The key feature of "μTAS" is that it can automatically analyze the sample by integrating the entire manipulation processes, including mixing, reacting, separating, and detecting, as shown in Fig. 1.2 [20–27]. Glass and polymers, such as polydimethylsiloxane (PDMS), are the most common materials for fabricating micro or nano features of μTAS via lithography techniques [20–27].

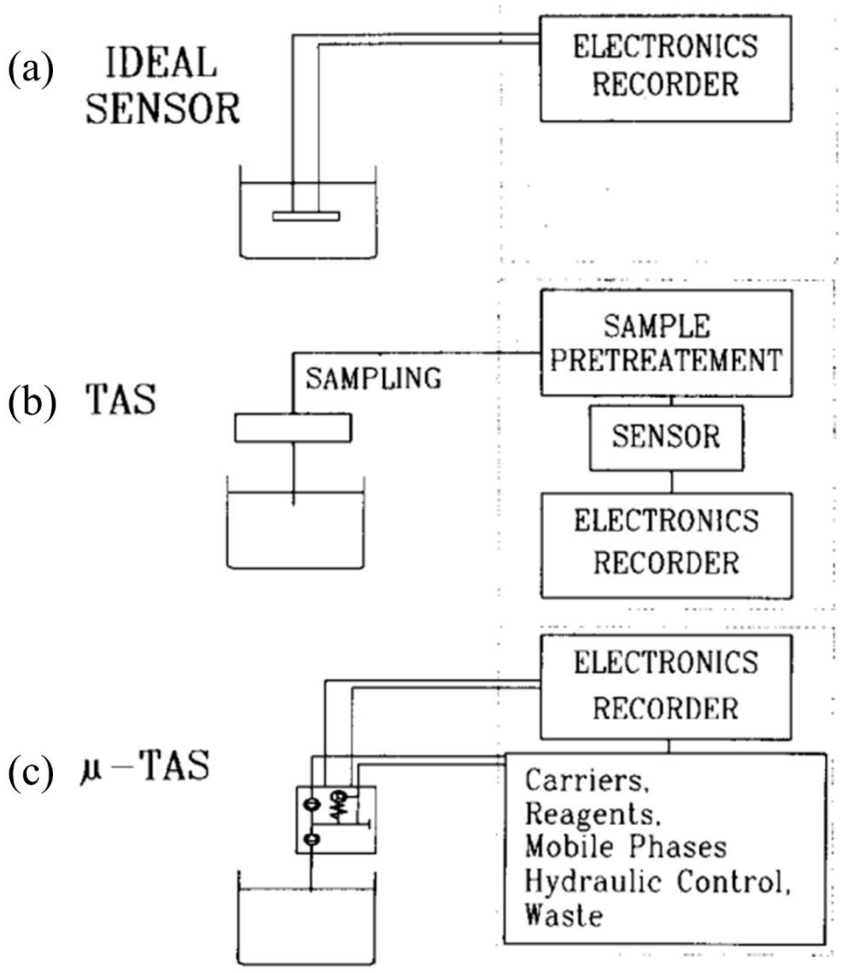

Figure 1.2 Schematic illustration of (a) an ideal chemical sensor, (b) a total chemical analysis system (TAS), and (c) a miniaturized TAS (μTAS). Reprinted with permission from reference [20]. Copyright 1990, Elsevier.

Whitesides' group demonstrated the fabrication of micro-sized patterns on filter paper, via standard photolithography, as an alternative substrate material to provide additional advantages [15–19]. The advantages of the paper material as a sensor substrate are as follows: (i) low-cost, (ii) abundance, (iii) ease of disposability with incineration, (iv) mass productivity, and (v) high chemical/physical stability [28–30]. In addition, the paper material does not require an external instrument for manipulating the liquid samples owing to small pores in the cellulose fibers, which draw up the liquid via capillary forces; this is the biggest feature difference compared with glass and polymer-based devices. Therefore, μPADs are a potential alternative analytical method, combining the advances of digital technologies to provide a society where anyone, anywhere, can conduct facile analyses of, for example, biomarkers, ions, or viruses.

To utilize the advantage of paper materials, many researchers have investigated and developed fabrication methods for achieving high-resolution patterning with low-cost and simple steps (Figure 1.3) [29–32]. The first report of μPAD in 2007 used the standard lithography method; however, this method required many steps and a complicated operation [15]. The developed fabrication methods are classified into four categories; (i) photolithography, (ii) hand craft, (iii) printing, and (iv) cutting (shaping). Photolithography is used in photoresists, photomasks, and UV patterning and fabrication must be conducted in a clean room. Hand craft uses a hydrophobic-ink filled pen (ca. ball-point pen) or a patterning-shape stamp with hydrophobic ink. Thus, this is the most approachable method. In printing, the hydrophobic ink, such as thermoplastic wax and a polymer (UV-curable or thermosetting), is used to print the patterns by a wax printer, an inkjet printer, or mess-screen printing method. The fabrication step is facile and the user can select the ink composition. However, UV-irradiation or heating over 100 °C is required for the formation of the pattern. Cutting used a craft or a laser cutting machine and can be shaped as designed; i.e., the μPAD fabricated by cutting is bare paper, unlike other fabrication methods. These methods are facile and require no expensive instruments and special facilities, which is a reason why research on μPADs is being actively conducted across the world.

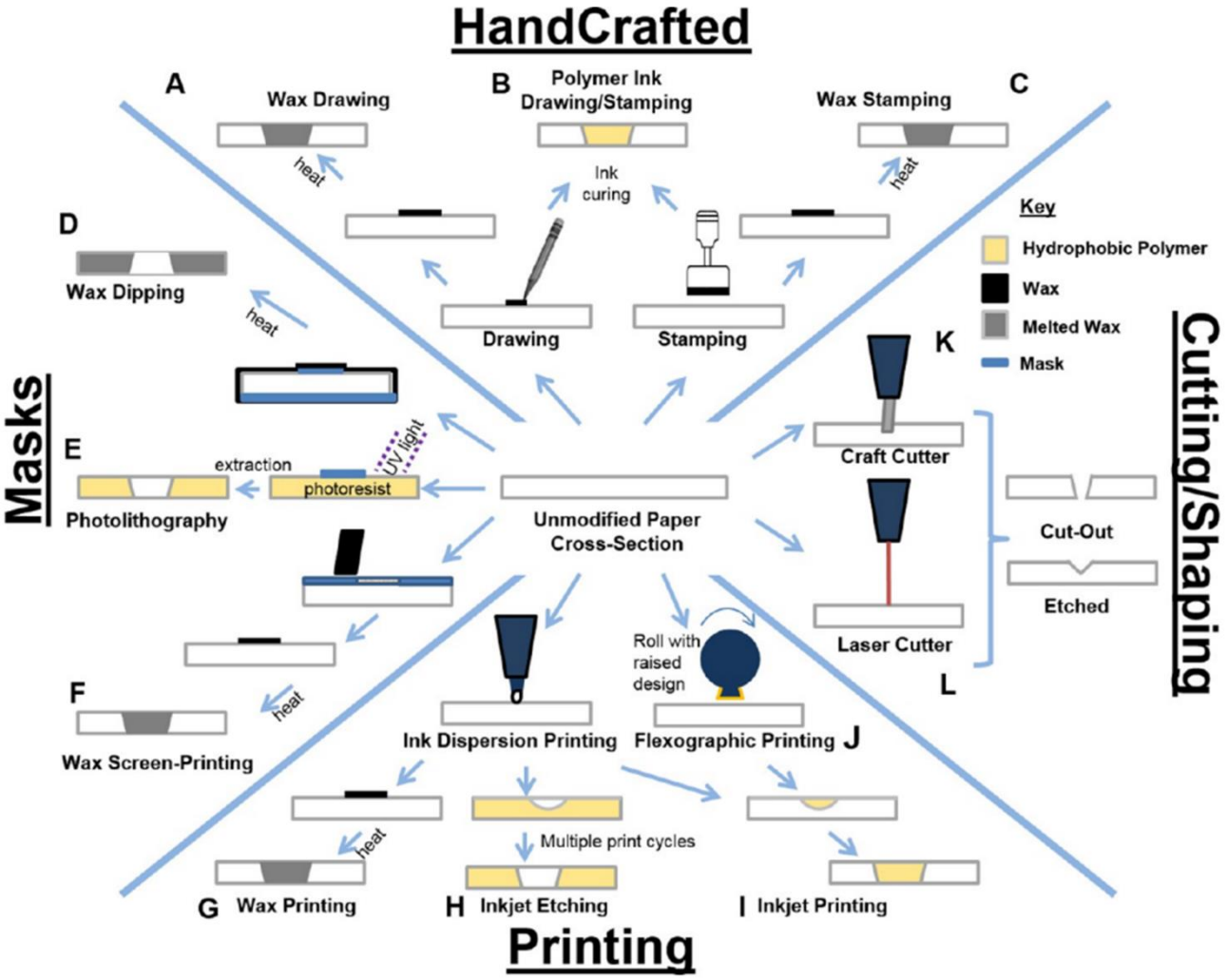

Figure 1.3 Schematic illustration of developed fabrication methods of the μPAD. Reprinted with permission from reference [32]. Copyright 2015 American Chemical Society.

1.2 Applications to blood analysis

Blood analysis within the field of diagnostics is an application of μPADs [28–30, 33, 34]. Commonly, the plasma (or serum) separation and the control of the precise plasma volume is a crucial pretreatment process, required to quantitatively analyze the target analyte [35–37]. In this section, reported technologies for the pretreatment and control of transported liquid volume using paper materials will first be introduced. Next, several reports that have demonstrated the determination of blood components in serum, plasma, and whole blood will be briefly explained by dividing the detection methods into three categories.

Finally, the characteristics of the three detection methods will be compared by focusing on glucose detection, which is used as a common target.

1.2.1 Approach for pretreatment

Blood cells (particularly red blood cells) affect the signal for determining the concentration of target analytes in whole blood [35, 36]. Paper is a porous and commercially available material that can be used for separating the membranes of blood cells. These separated membranes provide the pure plasma via capillary forces while capturing blood cells in the pores formed by non-uniform fibers. Thus, these separated membranes are usually embedded into the μPAD for blood tests. The approach without separated membranes, i.e., the aggregation of red blood cells (RBCs), is effective for separating plasma from whole blood. Yang et al. reported [38] an alternative RBC aggregation technique using antibody pre-loaded paper (Fig. 1.4a). In this technique, RBCs in the whole blood are aggregated with antibodies in the inlet of the paper; hence, only plasma will flow into the μPAD via capillary forces. Nilghaz et al. reported [39] salt-functionalized paper to induce the aggregation of RBCs by controlling osmotic pressure. This mechanism involves the plasma dissolving the salt concentrated on the paper and, as a result, the RBC shape deflates to a thin disk, as shown in Fig. 1.4a. This will encourage the RBCs to contact one-another and form agglomerates; this will enhance the capture efficiency of RBCs via the paper pores, only allowing plasma to migrate into the paper via the capillary force.

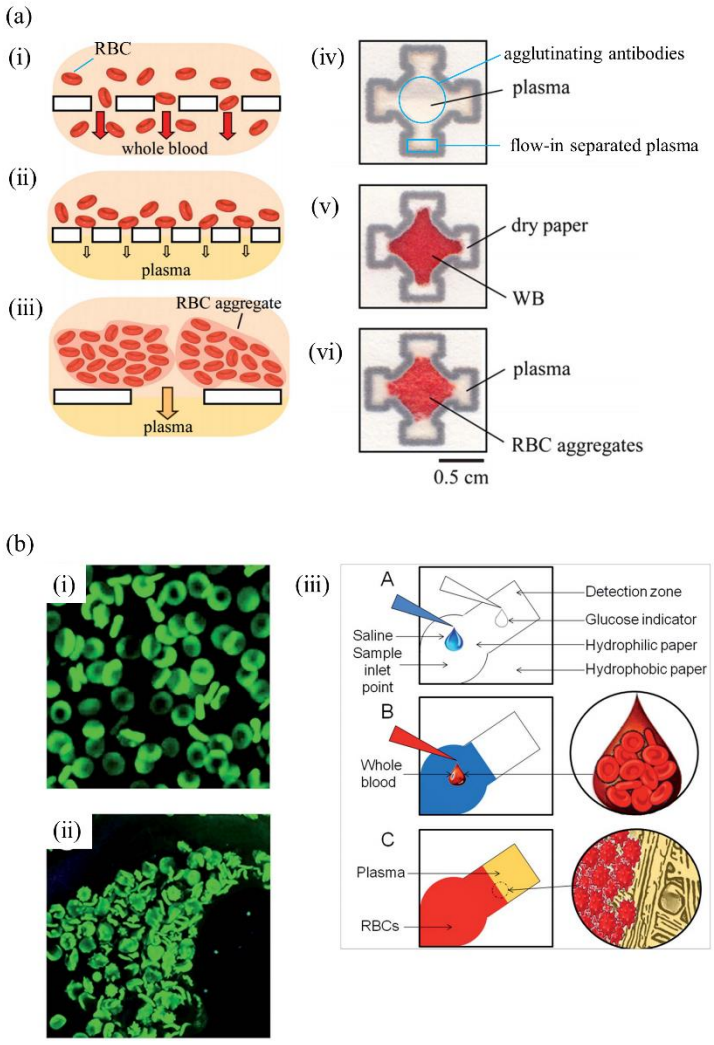

Figure 1.4 Plasma separation technique on paper using agglutination. (a) Schematic illustration of the behavior of the entire blood on (i) typical filter paper, (ii) commercial plasma-separation membrane, and (iii) μPAD with the aggregation-inducing antibody. Photographs of the μPAD after loading with (iv) plasma, (v) whole blood, and (vi) after plasma separation. Reprinted with permission from reference [38]. Copyright 2012, The Royal Society of Chemistry. (b) Salt-functionalized μPAD to induce the aggregation of RBCs by controlling osmotic pressure: confocal micrographs of RBCs on (i) the glass slide under isotonic conditions; (ii) a filter paper functionalized with 0.68 M (4% w/v) saline solution; (iii) schematic illustration of the plasma separation using the salt-functionalized μPAD. Reprinted with permission from reference [39]. Copyright 2015, The Royal Society of Chemistry.

Conversely, the retention of proteins in whole blood should be considered as the target molecule during the separation procedure. Guo et al. reported [40] the approach of plasma separation for providing a low protein loss using synthetic paper. The synthetic paper was fabricated via multi-directional lithography of an off-stoichiometry thiol-ene (OSTE) and its architecture comprises fabricated interlocking micropillar scaffolds as pores. The plasma separation is induced by the capillary separation of plasma and the interlocked micropillar scaffolds by the local aggregation of blood cells due to loading the RBC aggregation antibody on the inlet pad of the synthetic paper [40]. Additionally, to reduce the protein loss in the separated plasma, they combined O_2 plasma treatment with changing the amount of aggregation antibody to provide a high protein recovery of approximately 82 %. Note that the most important point of plasma separation utilizing paper is that only plasma can be transported via the paper, without any external forces. However, the plasma transportation by capillary force of the paper exhibits a trade-off relation with the control of the plasma volume: the transported plasma volume cannot be controlled after loading to the paper. For accurate blood test diagnosis, the use of the precise volume of the plasma is essential as blood tests are dependent on the amount of substance per unit volume of the serum or plasma [37]. Therefore, the challenge is to precisely control the plasma volume during pretreatment, using only paper materials. To date, various approaches have been developed to overcome this challenge. The first is valve techniques to control the approach of liquid samples, as reported by several groups [41–45]. In the technique reported by Li et al. [41], the sample flow is activated and inactivated via manual operation of the valve, as shown in Fig. 1.5a. However, this report requires manual operation by the user and, therefore, is not user friendly. Fu et al. reported [42] a μPAD integrated with an auto-switch system via a temperature-responsive polymer (Fig. 1.5b). The temperature-responsive polymer actuated paper valve can automatically connect or disconnect the two channels responding to the various temperature. Note that these utilize a 2D-design because the single channel is separated into two channels for fabricating the valve.

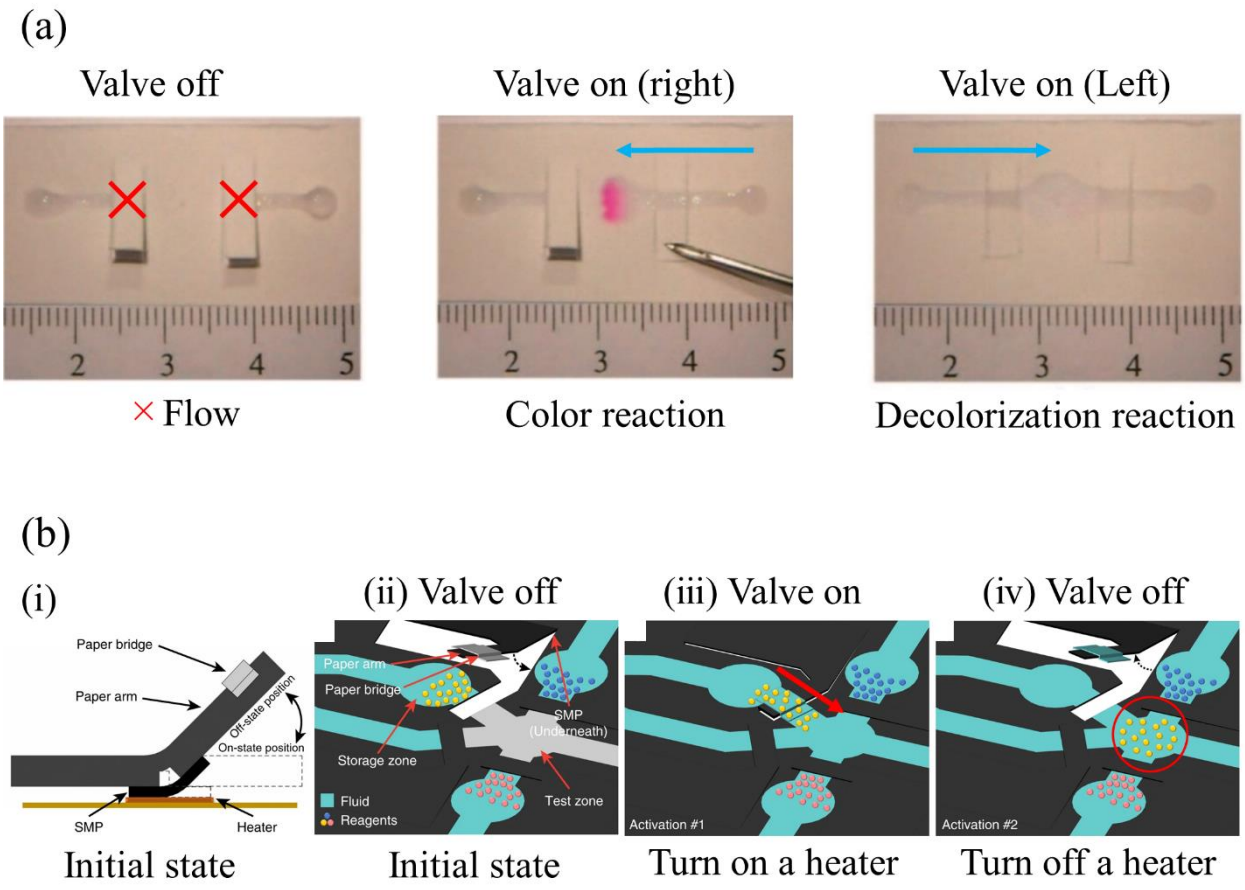

Figure 1.5 2D-valve technique for controlling the liquid volume with paper materials. (a) Manual operating valve fabricated by separating continuous flow channel into two pieces. Reprinted with permission from reference [41]. Copyright 2008, American Chemical Society. (b) The shape-memory polymer actuated paper valve (SMP-valve): (i) details of SMP-valve system; (ii – iv) the procedure of the valve activation in the μPAD. Reprinted with permission from reference [42]. Copyright 2019 Springer Nature.

Martinez et al. [45] reported a different valve technique, involving a 3D-design and a button to control the empty space between two channels, i.e., this empty space plays the role of the valve. For providing the sample, the user manually pushes the button to connect the two channels.

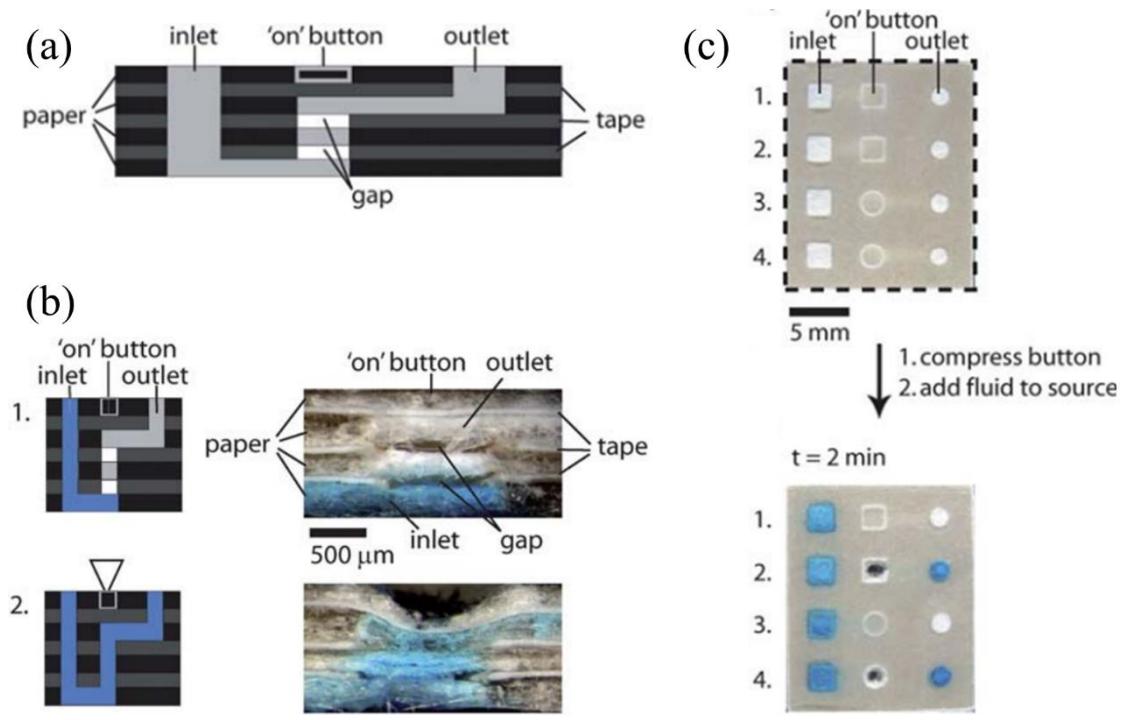

Figure 1.6 3D-valve technique for controlling the liquid volume with paper materials. Cross-section of (a) the design of the μPAD consisted of seven paper layers, (b) mechanism of the liquid flow using the μPAD (left) and photographs after operating the valve with 'on' button of the μPAD, (c) photographs of the μPAD from the top view that demonstrated the liquid flow. Reprinted with permission from reference [45]. Copyright 2010, American Chemical Society.

The second technique utilizes 2D-microfluidic networks [46–48]. Lutz et al. reported [46] the sequential delivery of liquids by connecting a series of paper legs to the inlet of the main channel. The inlets, connected with different leg lengths, were dipped into the liquid reservoir and will disconnect with the reservoir as the volume of liquid reduces due to liquid penetration into the channels (Figure 1.7a). As a result, the supply of liquid depends on inlet length. Additionally, the change in channel length from the detection zone can provide the arrival time delay of the liquid, i.e., the preloaded dye at each inlet can arrive at the detection zone at different times, as shown in Figure 1.7a. Thus, the sequential delivery system of liquids can apply the automatic detection system, which requires multiple loading procedures of various reagents, such as immunoassays. This group demonstrated that an immunoassay required multiple steps by applying this technique [48].

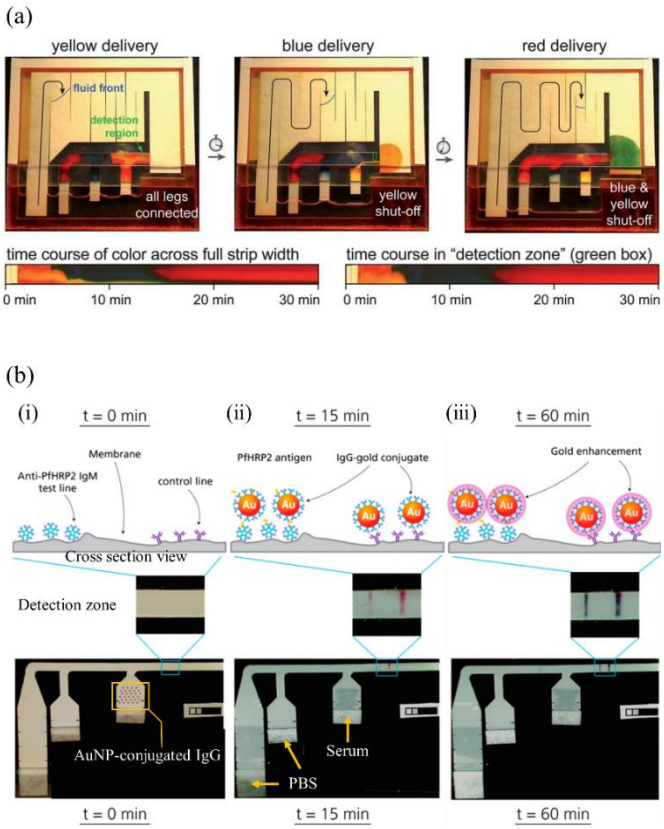

Figure 1.7 2D-microfluidic networks for controlling the liquid volume via paper materials. (a) Autonomous sequential fluid delivery with 2D-microfluidic networks. Each leg wicked liquid from a single buffer source and dried dyes representing reagents create different fluids from each leg. Each colored liquid arrived at a different time at the "detection region" (green box) and was shut off in a timed sequence after delivery. Reprinted with permission from reference [46]. Copyright 2011, The Royal Society of Chemistry. (b) Application of detection PfHRP2 (Ag) in serum with 2D-microfluidic networks of the μPAD. (i) Before loading required liquids to the three legs, anti-PfHRP2 IgM was immobilized as a capture line while goat anti-mouse IgG was used as a control line. Additionally, anti-PfHRP2 IgG-gold conjugate was patterned for rehydration on the right leg (red dots). (ii) 15 min after loading of 30 μL Ag (100 ng/mL)-spiked serum, 40 μL and 100 μL of PBS for the right, middle, and left leg, respectively. (iii) 60 min after complete detection of Ag in serum. Reprinted with permission from reference [48]. Copyright 2014, American Chemical Society.

Regarding the other physical approach, Liu et al. reported [49] the slip PAD for achieving high-throughput chemical sensing. This approach separates the channel (top layer) and several inlets with different liquid samples (bottom layer) and aligned the layers, as shown in Fig. 1.8. The different liquid samples are sequentially transferred into the channel by slipping the bottom layer. Since this design can be easily parallelized on the same paper plane, multiple operations can be performed simultaneously for high-throughput chemical sensing.

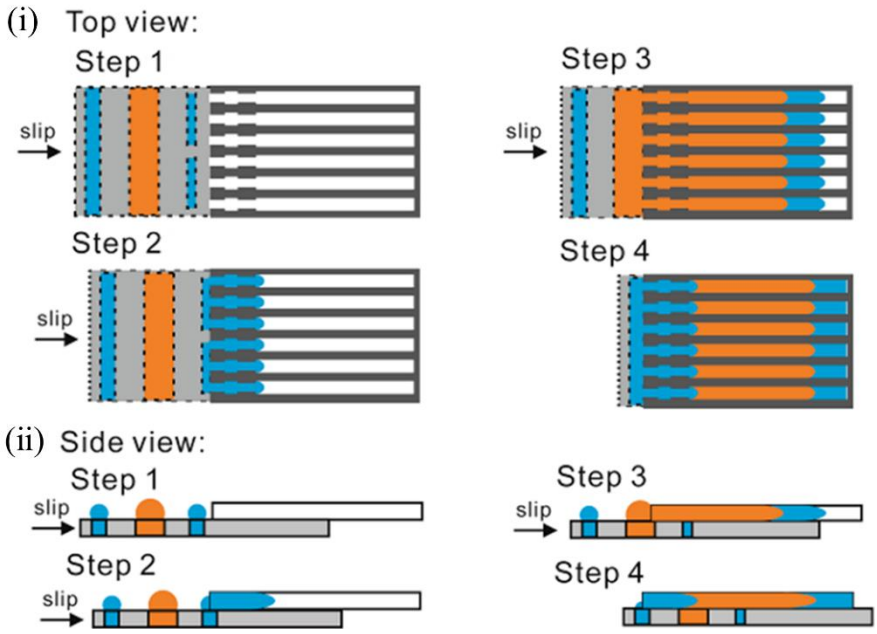

Figure 1.8 Slip design for controlling the liquid volume with paper materials. Schematic illustration demonstrating the operating principle of the SlipPAD for sequential fluidic manipulation. The SlipPAD is comprised of two layers: the bottom layers and the fluidic channels and reservoirs patterned therein, which are highlighted by black dashed lines in the top view. Reprinted with permission from reference [49]. Copyright 2013, American Chemical Society.

As a different method of controlling the fluid volume, various chemical-based approaches have been developed [50]. Lutz et al. reported [50] that treating the paper with sucrose helps delay the fluid, as shown in Fig. 1.9a.

The fluid velocity depends upon the concentration of the treating sucrose solution and the higher concentration delays the transportation of the fluid. Therefore, the transportation time of the fluid can be easily controlled by changing the sucrose concentration of the treatment solution, without complicated channel design. Another approach utilizes a sugar block paste, which can dissolve in the liquid sample [51]. In this approach, the sugar block paste was connected between two paper materials, shutting off the blood supply after the transportation of a certain volume as the paste became destroyed (Fig. 1.9b). Thus, the transfer volume of the liquid depends upon the properties of the sugar block paste and the materials of the sample source pad; the volume was tunable from 10 to 80 μL.

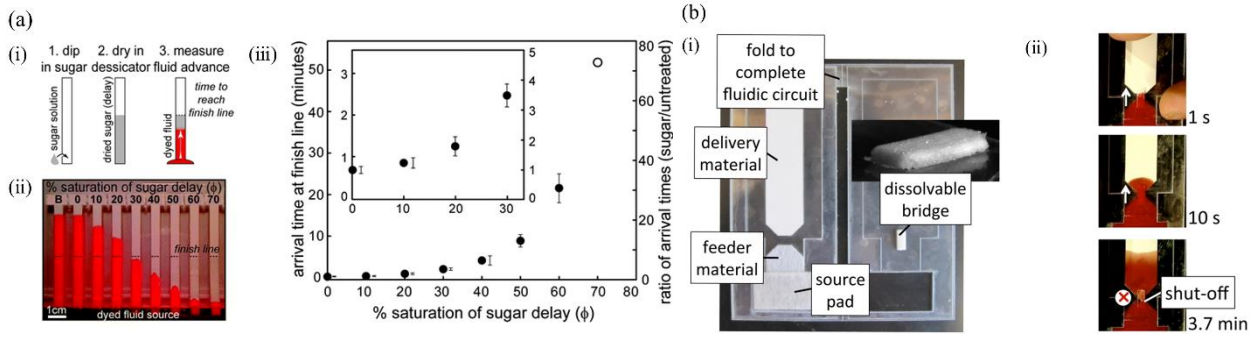

Figure 1.9 Sugar treatment for controlling the liquid volume via paper materials. (a) Liquid control created by sugar treatment of different concentration dried on paper strips. (i) Schematic illustration of an investigation of liquid control using sugar treated paper strip. (ii) Photograph after dipping the legs of sugar-treated strips into the dyed fluid source. "B" indicates an untreated strip and "0 %" indicates a strip dipped in DI water (no sugar). (iii) Quantification of arrival times at the finish line. The arrival time for the untreated strip "B" was 44 s and the maximum delay (treated with 70 % sugar solution) was 53 min. The inset shows detail for shorter delay times. Reprinted with permission from reference [50]. Copyright 2013, The Royal Society of Chemistry. (b) Control of blood volume with a fluidic circuit consisted of a dissolvable sugar bridge and two paper pieces. (i) Photograph of the top view of the fluidic circuit. (ii) Demonstration of the control of the blood volume. The blood supply was stopped at 3.7 min owing to the destroyed sugar bridge (shut off) after loading the whole blood into the source pad. Reprinted with permission from reference [51]. Copyright 2013, American Chemical Society.

1.2.2 Electrochemical detection

Electrochemical detection can provide high measurement performance by measuring electric signals converted from the chemical reaction via external measuring instruments. In 2009, Dungchai et al. first reported [52] the application of electrochemical detection to the μPAD and demonstrated the multianalyte determination of glucose, lactate, and uric acid in human serum, using cyclic voltammetry. The μPAD fabricated by photolithography was modified with carbon ink containing Prussian Blue as the working and counter electrode (WE/CE), silver/silver chloride ink as the reference electrode (RE), and conductive pads by screen printing (Fig. 1.10).

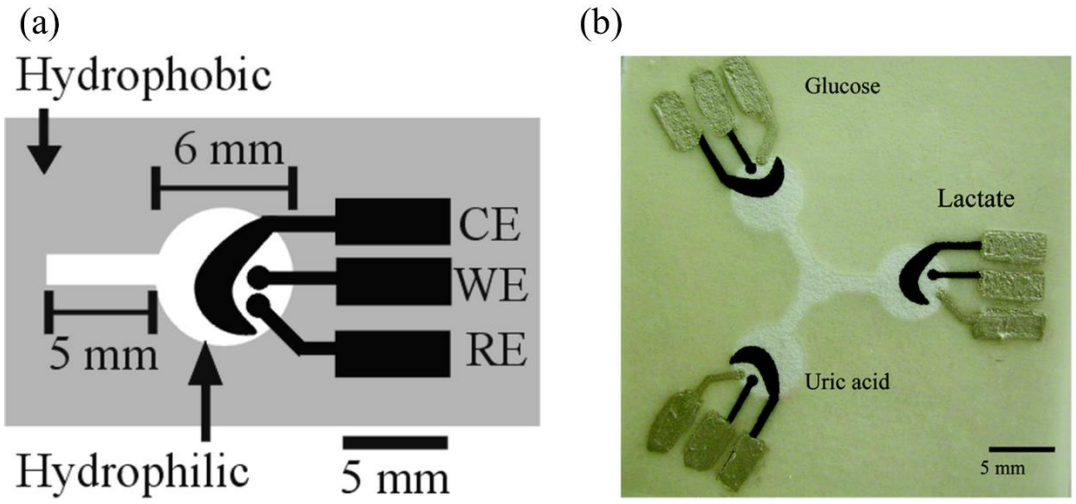

Figure 1.10 First report of the μPAD using electrochemical detection. (a) Device design of the electrochemical detection cell. WE, working electrode; RE, reference electrode; CE, counter electrode. (b) Photograph of the three electrode μPADs. The hydrophilic area at the center of the device wicks the sample into three separate test zones where independent enzyme reactions occur. The device size is 4 cm × 4 cm. Reprinted with permission from reference [52]. Copyright 2009, American Chemical Society.

This report achieved the determination of glucose, lactate, and uric acid, with high measurement performance, using three electrode μPAD: the LODs were 0.21 mM, 0.36 mM, and 1.38 mM, for glucose, lactate, and uric acid respectively. With the exception of uric acid, sufficient measurement performance was achieved for clinical diagnosis. To date, many μPADs have been developed that can detect organic molecules [52–60], proteins [61–66], nucleic acid [67–71], ions [72], and cells [73] as the target analyte in human blood. The most common target is glucose as diabetes is very common worldwide and a major cause of death [52–57]. Nie et al. developed [53] the cartridge-type μPAD for integration with the commercially handheld glucometer (i.e., TRUEtrack from CVS/Pharmacy) and enabled rapid and quantitative detection of glucose, cholesterol lactate, and alcohol (Fig. 1.11a). This μPAD requires ~1 μL sample (blood, plasma, or standard solution) and achieved good measurement performance of glucose in whole blood with high reproducibility (coefficient of variance, CV, 9.1 %) when integrated with the commercial glucometer. Noiphung et al. reported [54] the dumbbell-shaped μPAD that has two plasma separation zones using blood cell separation paper, which is connected to the detection paper using chromatographic filter paper in the center, as shown in Fig. 1.11b. The portions of 200 μL undiluted blood were introduced into two separation zones and the separated plasma arriving at the detection zone in the center will simultaneously contact the commercially reusable electrode. The current relies on the glucose concentration in the whole blood and is measured using chronoamperometry, with an Autolab PGSTAT101 electrochemical analyzer. This μPAD, combined with a commercial reusable Prussian Blue screen-printed electrode, achieved a wide linear range of up to ~33 mM glucose concentration in whole blood (R^2 = 0.987), with high reproducibility (maximum CV, 9.0 %). Kong et al. developed [55] a μPAD combined with paper-disk chromatography and a disposable screen-printed carbon electrode (SPCE), modified with the graphene/polyaniline/gold nanoparticles/glucose oxidase. The paper disk, after loading with a minimum of 2 μL whole blood, is dried in air and laminated to cover the entire electrode. After loading PBS onto the paper disk, the current, a detected signal, of flavin adenine dinucleotide (FAD) in GOD was decreased due to the enzyme-substrate reaction, which was measured using differential pulse voltammetry (DPV). The analytical performance covered the full range of clinically relevant concentrations of glucose in whole blood (0.2 ~ 11.2 mM) and the LOD was 0.1 mM. Canovas et al. reported [56] the μPAD for working as the

potentiometric cell and combined it with the wireless potentiometer for measuring the redox potential induced by the enzymatic reaction. The μPAD was fabricated by combining the paper-based working and reference electrodes to build an entire potentiometric cell using, which also provides a sampling module for simply and rapidly determining glucose in a single drop of blood (~25 μL), as shown in Fig. 1.11c. This report achieved a linear range from 0.3 to 3 mM and the LOD was 0.1 mM. Additionally, through combination with the wireless potentiometer, the redox potential as the detection signal can be displayed on a smartphone via dedicated application software. This is an ideal approach for point of care testing. Unlike the four reports introduced above, Chaiyo et al. developed [57] a μPAD that does not require an enzyme reaction. The SPCE of the μPAD was modified with cobalt phthalocyanine, graphene and an ionic liquid (CoPc/G/IL). Due to a significant synergistic increase of the electrochemical signals using IL, CoPc, and NaOH as supporting electrolyte (0.1 M), the μPAD achieved excellent performance (the linear range was from 0.01 to 1.3 mM) without the enzymatic reaction and the LOD was 0.67 μM. Note that the electrochemical detection requires external measurement instruments, i.e., the electrochemical analyzer for detecting the electric signal.

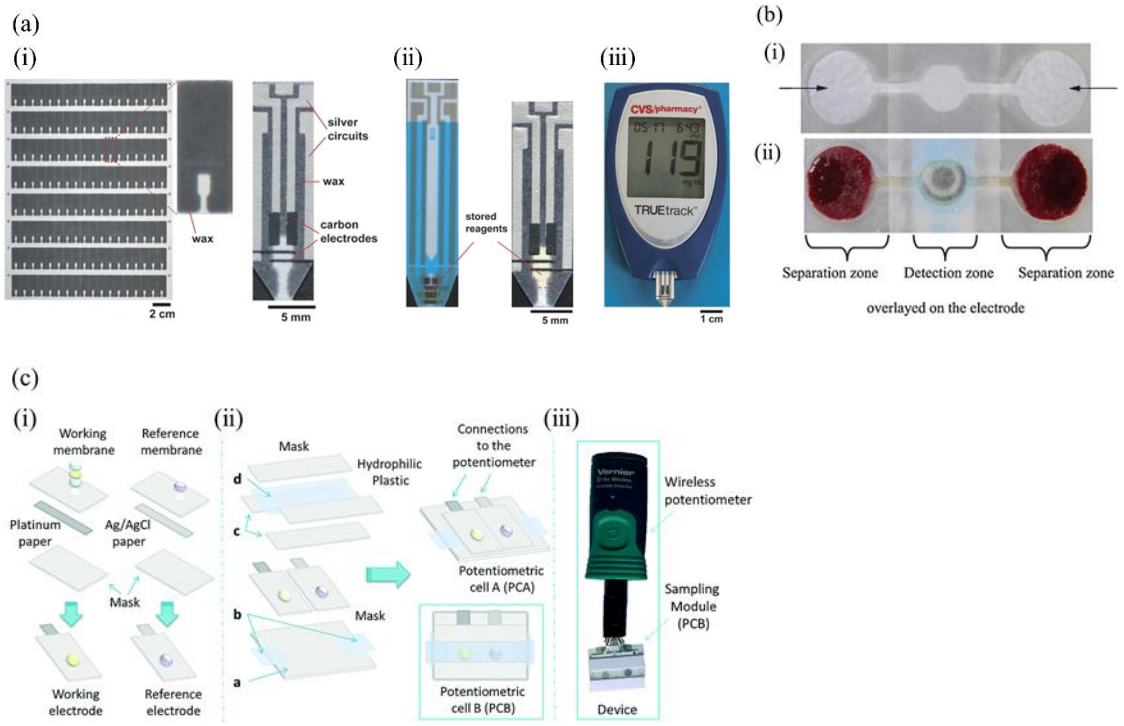

Figure 1.11 Quantitative glucose detection in human whole blood by electrochemical detection. (a) Glucose detection using the cartridge-type μPAD and a commercial glucometer as an electrochemical reader: (i) mass production of the cartridge-type μPAD; (ii) photograph of commercial glucose test cartridge (left) and the cartridge-type μPAD with a wax-defined channel, silver- and carbon-electrode; (iii) glucose measurement using the cartridge-type μPAD with a commercial glucometer. Reprinted with permission from reference [53]. Copyright 2010, The Royal Society of Chemistry. (b) Photograph of (i) the dumbbell-shape μPAD and (ii) after loading whole blood to the dumbbell-shape μPAD and laminated onto the commercially usable electrode. Reprinted with permission from reference [54]. Copyright 2013, Elsevier. (c) Schematic illustration of (a) the fabrication of the working and reference electrode, (b) the μPAD working as a potentiometric cell, and (c) photograph of the μPAD containing the sensor as the sampling cell and the wireless potentiometer. Reprinted with permission from reference [56]. Copyright 2017, The Royal Society of Chemistry.

1.2.3 Fluorescent and luminescent detection

Fluorescent and chemiluminescent detection can achieve good performance when measuring the photo-signals detected by external optical instruments. Fluorescent detection has been applied to numerous biomarker measurements in human whole blood, such as cancer antigens [74, 75], enzymes [76, 77], nucleic acid [78, 79], ions [80], and organic molecules [81, 82]. Regarding the application of fluorescence detection to the μPAD, the detection principle can be categorized into three mechanisms: (i) the fluorescent resonance energy transfer (FRET) for antigens; (ii) loop-mediated isothermal amplification (LAMP) for nucleic acid; (iii) others (aggregation-induced emission fluorogen, carbon/quantum dots) for ions and organic molecules. For glucose detection, Chang et al. developed [82] a μPAD using aggregation-induced emission fluorogens (AIEgen) for facile and sensitive visual detection. The principle of AIE-based strategy for glucose detection is using tetraphenylethene functionalized with the maleimide group (TPE-M), AIEgen, as shown in Fig. 1.12a. The maleimide group in TPE-M reacts with the active thiol group (-SH) of L-cys, breaking the C=C bond and forming a new compound, TPE-M-L, which emits strong fluorescence in its aggregated state and thus acts as the AIEgen. In the presence of hydrogen peroxidase (H_2O_2) produced by the glucose oxidase-catalyzed oxidation of glucose, L-cys was oxidized by H_2O_2 to form cystine, which cannot react with TPE-M, resulting in a subsequent decline in fluorescence intensity. In this report, 1 μL of the mixed solution, including glucose, glucose oxidase, and L-cys, was loaded after the reaction to the μPAD pretreated with 1 μL of 400 μM TPE-M acetonitrile solution. For visual detection, the photograph of the μPAD was taken under UV light illumination (365 nm) in the dark. This group demonstrated that the visual detection range of glucose using the μPAD is 0.01 to 5 mM due to the simple recognition of fluorescent intensity (Fig. 1.12b). However, this method provides a semiquantitative analysis and requires UV light as the excitation light source, as well as a dark place.

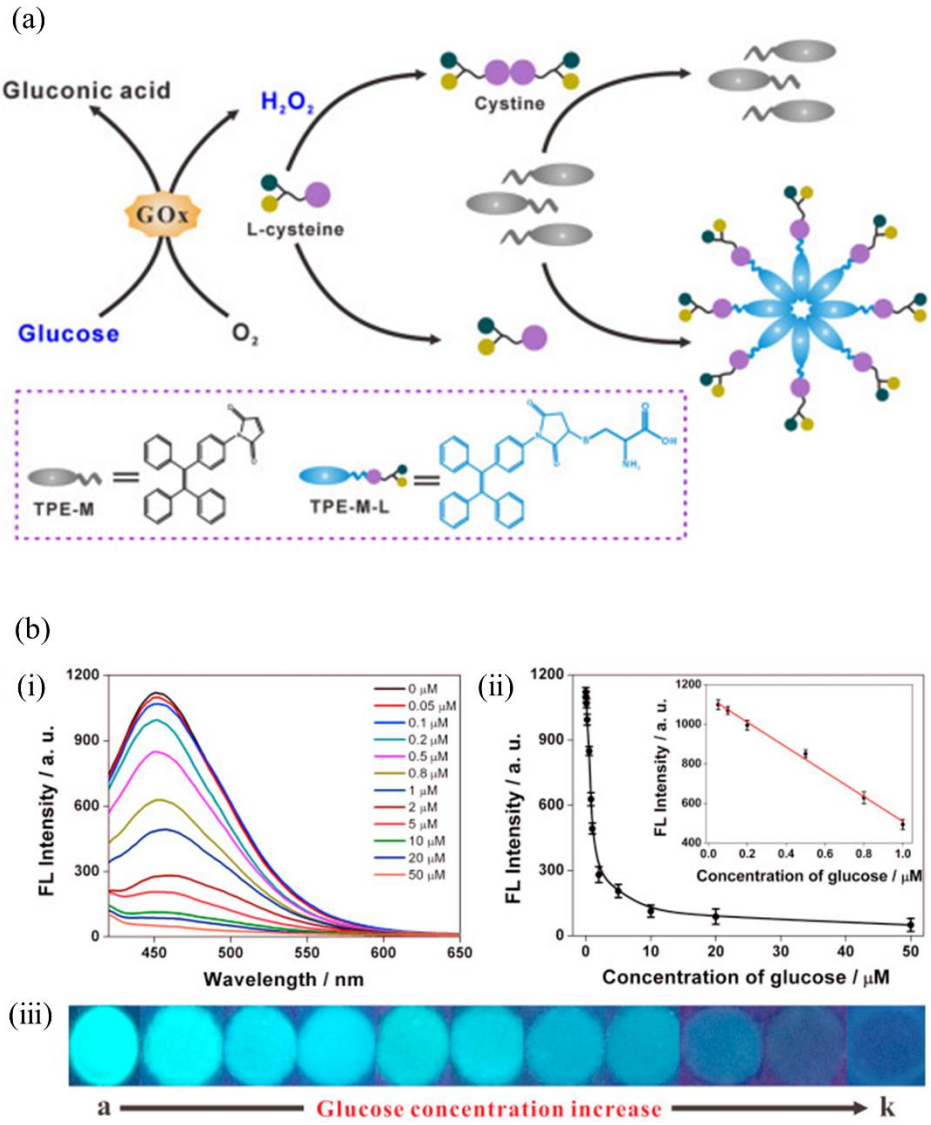

Figure 1.12 Quantitative glucose detection in human serum by fluorescent detection. (a) principle of AIE-based strategy for glucose detection the tetraphenylethene functionalized with the maleimide group (TPE-M). (b) Fluorescence of different glucose concentrations obtained by this strategy. (i) fluorescent spectra and (ii) fluorescent intensity at 460 nm, insert: linear range vs. glucose concentration in this system (results on solution-state using fluorescent spectra). (iii) photographs of the μPAD detected different glucose concentrations. Reprinted with permission from reference [82]. Copyright 2018, Elsevier.

Luminescent detection is categorized into two mechanisms, based on chemistry or biology: chemiluminescence [83–88] and bioluminescence [89, 90]. These detections were also applied to numerous

biomarker measurements in human blood, such as cancer antigens [83–86], organic molecules [87, 88], anti-virus antibodies [89], and nucleic acid [90]. The features of chemiluminescent and bioluminescent detections in the μPAD is the use of immunoassays, based on target (an antigen or organic molecule)-antibody reactions [83–87], and bioluminescence resonance energy transfer (BRET), based on protein-protein interactions against the target [89, 90] as the detection mechanisms, respectively. For glucose detection using chemiluminescence, Li et al. reported [88] a 3D-μPAD comprising the detection layer. At the bottom of the μPAD are four circle-shaped detection zones for detecting glucose (No.1), lactate (No.2), choline (No.3), and cholesterol (No.4), and the auxiliary layer at the top which has the channel connected sequentially to the four detection zones, as shown in Fig. 1.13a. The four detection zones were modified with chitosan, cobalt ion (Co^{2+}), and different kinds of oxidases: glucose oxidase, lactate oxidase, cholesterol oxidase, and choline oxidase for glucose (No.1), lactate (No.2), choline (No.3), and cholesterol (No.4) detection zones, respectively. The chitosan co-immobilizes the Co^{2+} via the chelating reactions between cobalt ion and the amino groups from chitosan and provides good support for enzyme adsorption. Thus, the diluted serum — containing luminol, glucose, lactate, cholesterol, and choline — loaded to the inlet of the top layer arrives sequentially at the No.1 to No.4 detection zones and exhibits chemiluminescence, with different times for achieving multiplexed quantitative analysis (Fig. 1.13b). Focusing on the glucose detection, the linear range was from 0.01 to 1.0 mmol/L and the LOD was 8 μM. Note that this method requires an ultraweak luminescence analyzer for measuring chemiluminescent intensity.

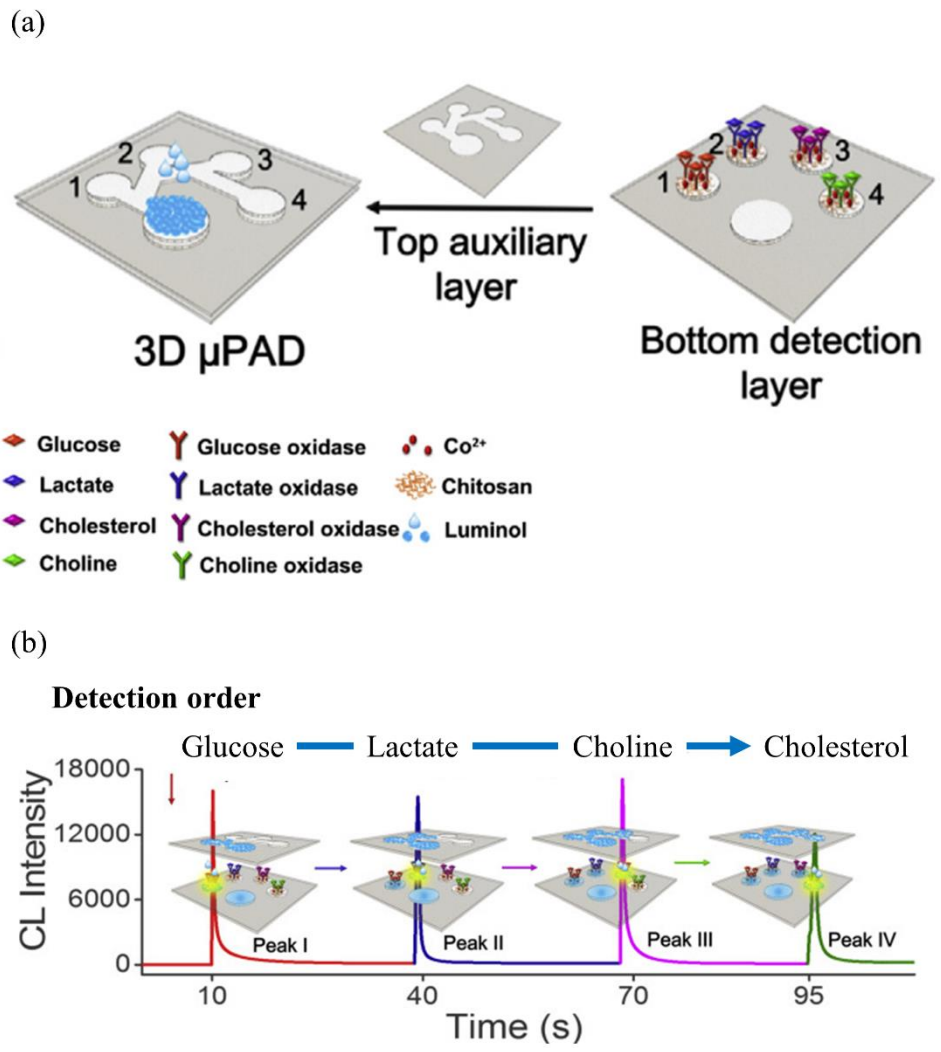

Figure 1.13 Quantitative glucose detection in human serum by chemiluminescent detection. (a) Schematic illustration of the fabrication of 3D-μPAD and details of reagents introduced in each detection zone. No. 1, No. 2, No. 3, and No. 4 detection zones are for glucose, lactate, cholesterol, and choline, respectively. (b) Multi-detection operation mechanism using 3D-μPAD and response chemiluminescent intensity versus time after loading the sample. Reprinted with permission from reference [88]. Copyright 2019, Elsevier.

1.2.4 Colorimetric detection

The first report by Whitesides' group has demonstrated glucose and bovine serum albumin (BSA) detection using standard sample by colorimetry. In 2008, to provide the novel analytical system for the point of care testing, this group proposed colorimetric detection using photographs obtained by cellphone cameras

and analytical computer-software for measuring color intensity. For example, Dong et al. reported [91] the rapid and low-cost measurement of c-reactive protein (CRP) in human blood by integrating the μPAD with a smartphone (Fig. 1.14a). The μPAD can detect CRP by directly loading whole blood and the color development is induced by aggregating the gold nanoparticle-conjugated anti-CRP antibody against the captured CRP at the detection zone (Fig. 1.14b). This report can determine the CRP concentration via smartphones with a dedicated image analysis application (Fig. 1.14c). Therefore, colorimetric detection is the most effective method for achieving point-of-care testing as it does not require large-external instruments (e.g., electrochemical- or optical analyzers) or a restricted environment for optical systems, as compared to other detection methods. Note that the colorimetric detection sometimes requires a small adaptor (such as Fig 1.14d) for providing the same measurement conditions to achieve a suitable measurement performance in diagnostic applications.

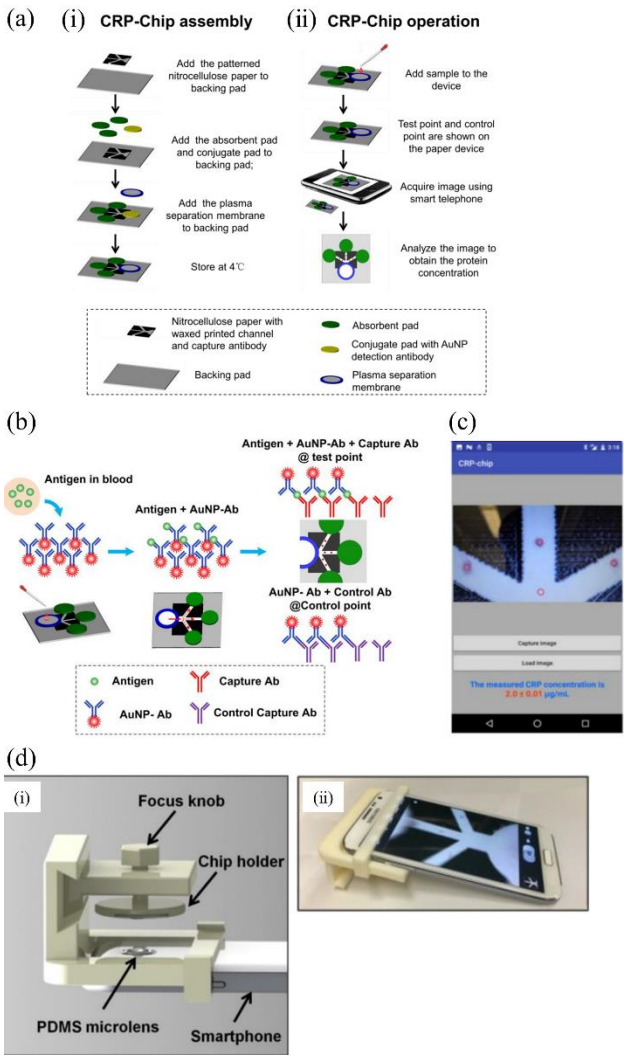

Figure 1.14 Colorimetric quantitative analysis of CRP in whole blood by combing the μPAD with a smartphone. (a) Schematic illustration of the fabrication of the μPAD (left) and the device operation (right). The μPAD can be used for untreated whole blood owing to the integration of a commercially-available blood cell separation membrane. After loading the whole blood at the inlet of the μPAD, the CRP concentration can be determined by image analysis of the smartphone. (b) The detection mechanism of CRP by sandwich immunoassay. One channel function as the control and the other two channels show the color depending on the CRP concentration in whole blood. This study used relative color intensity based on the intensity of the control. (c) Photograph after determination of the CRP concentration with a smartphone. (d) (i) Illustration of a portable adapter for smartphone measurement. (ii) Photographs of the smartphone attached with the portable adapter. Reprinted with permission from reference [91]. Copyright 2017, MDPI.

To date, numerous colorimetric-based μPADs for detecting biomarkers in plasma, serum, or whole blood have been developed. Like other detection methods, target biomarkers include protein [91–95], enzyme [92], antigen [96, 97], antibody [98], nucleic acid [99] and organic molecule [38, 39, 100–102]. For glucose detection via colorimetry, several groups have demonstrated the model assay to clarify the validity of the developed plasma separation approach [38, 39, 100]. The glucose concentration determined by Yang et al. [39] and Kar et al. [100] showed a correlation with that determined via conventional methods; however, they did not describe the linear range or the LOD by their developed μPAD. Nilghaz et al. reported [38] a linear range from 3 to 5 mM using the μPAD; this result agrees very well with centrifugally-separated plasma.

1.2.5 Comparison of characteristics of glucose detection using different detection methods

Table 1.1 presents a summary of the measurement performance of glucose in blood (or plasma, serum) using the different detection methods. Regarding the measurement performance, the use of colorimetric detection showed the small linear range in 10^{-3} molarity concentration and high LOD, compared to that obtained by other detection methods. Nevertheless, colorimetric detection has a higher potential for providing point-of-care testing owing to its non-requirement of large-external instruments and well-maintained environment for optical measurements. Conversely, electrochemical, fluorescent, and chemiluminescent detection also present a potential for application to point-of-care testing. However, to achieve point of care testing through these detection methods, a dedicated portable measurement instrument for integration with smartphones must be developed. Therefore, the detection method should be carefully selected while considering the required measurement performance for the target analyte in human blood.

Table 1.1 Summary of measurement performance of glucose by four detection methods.

Detection method	Linear range	LOD	Time	External instrument (without PC and Phone)	Ref
Electrochemistry	0 – 100 mM	0.21 mM	100 s	Potentiostat	52
	~0 – 27.8 mM	1.44 mM	60 min	Commercial glucometer	53
	0 – 33.1 mM	ND†	~7 min	Electrochemical analyzer	54
	0.2 – 11.2 mM	0.1 mM		Electrochemical workstation	55
	0.3 – 3 mM	0.1 mM	2 min	Wireless potentiostat	56
	0.01 – 1.3 mM, 1.3 – 5.0 mM	0.67 μM	1 min	Potentiostat	57
Fluorescent	0.01 – 5 mM	10 μM	~60 min	Naked eye (Under UV light)	82
Chemiluminescent	0.01 – 1.0 mM	8 μM	~10 s	Luminescence analyze	88
Colorimetry	2.8 – 11 mM	ND†	5 min	NR††	38
	3 – 5 mM	ND†	20 min	ND†	39
	ND† (~0.5 – 26 mM)	ND†	ND†	NR††	100
	0 – 5 mM	0.5 mM		NR††	17*

†: Not described

††: Not required

*: Glucose in artificial urine

1.3 Research objective of this thesis (Summary of the research motivation)

As reviewed in the previous sections, a demand for academic research on microfluidic paper-based analytical devices (μPAD) has grown rapidly after the first report by Whitesides' group in 2007. Figure 1.5 shows the relationship between the publication year and the number of (a) publications or (b) citations since 2007 (search word, "paper-based analytical device"). These results indicate that research related to PADs received increased attention and research and development is still being energetically conducted.

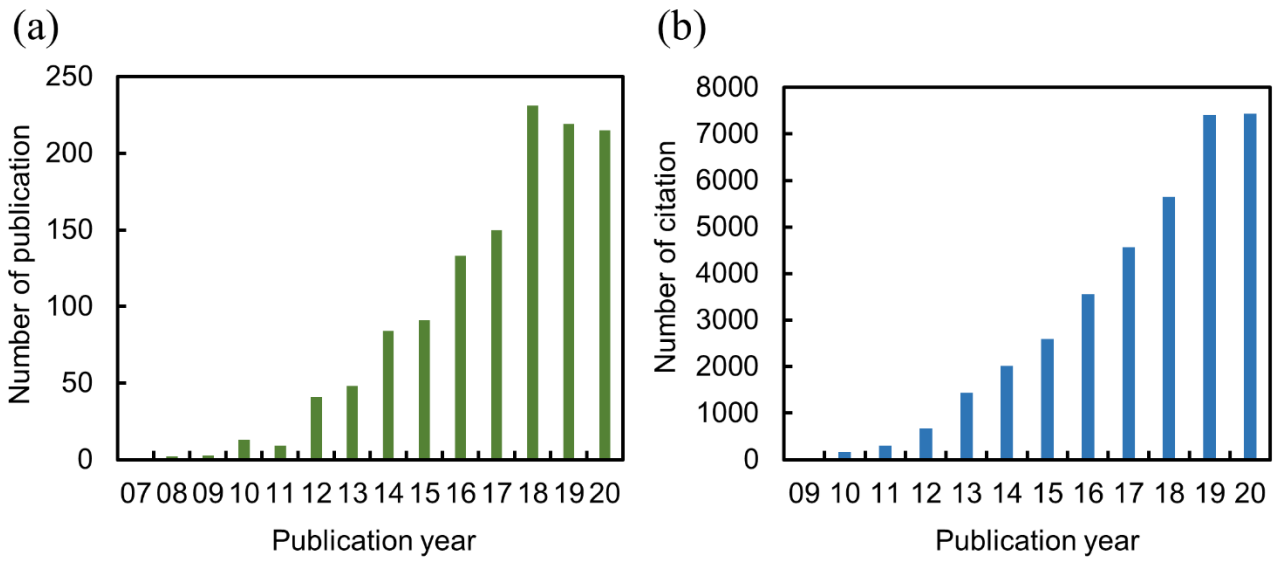

Figure 1.15 Number of (a) publications and (b) citations after the μPAD concept was first reported by Whitesides' group in 2007 (searched on the Web of ScienceTM on December 2nd, 2020).

The motivation of this thesis is to contribute to the improvement of the quality of diagnostics in the world from the standpoint of low-cost, rapid, and straightforward medical diagnostic technology. The PADs have been applied to numerous fields, such as clinical diagnostics, environmental analysis, and food safety analysis. In this thesis, I focused on blood tests that are demanded in many situations —not only in hospitals — such as home tests and emergency tests in the event of a disaster: there is a great need for the on-site analysis of blood tests. The problems with conventional blood tests include the requirement of a large amount of blood,

a complicated process (such as plasma separation), trained manipulations and techniques, large and expensive external instruments, high cost, and a long period for obtaining the results. Therefore, it is difficult to conduct on-site analysis for conventional blood tests owing to the above problems. In contrast, the reported PAD towards blood tests can provide an on-site analysis system integrating all of the analytical processes, from blood loading to detection, as shown in Fig. 1.16. In addition, the reported PAD can be simply disposed of by incineration, which solves the problems of medical wastage, as well as cumbersome operation and high-cost.

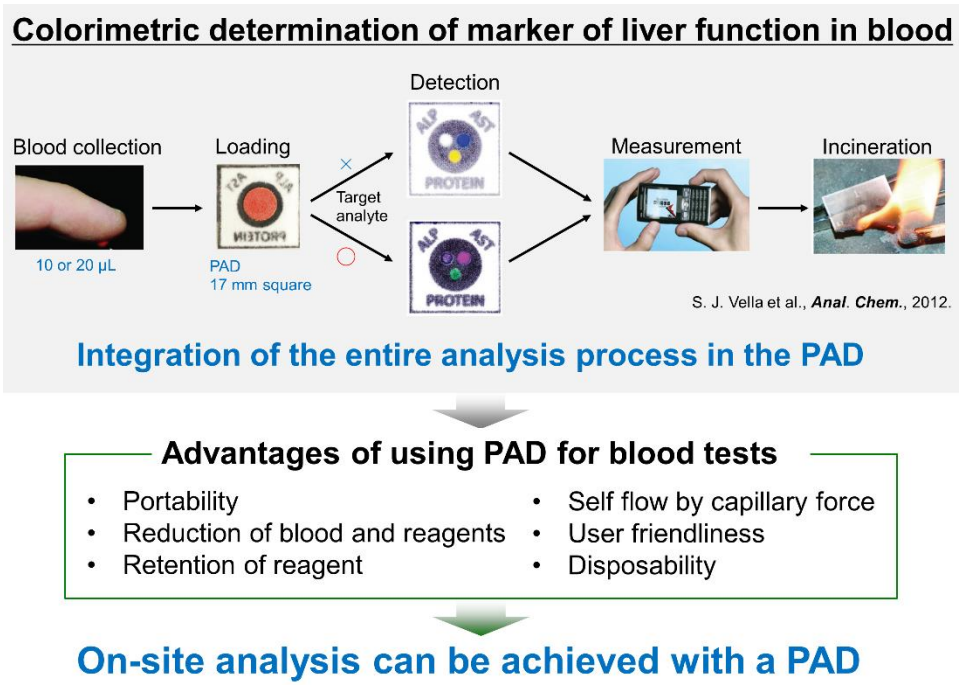

Fig. 1.16 The reported PAD for measuring liver function markers in blood via colorimetry and a summary of the advantages of using PADs for blood tests. Reprinted with permission from reference [92]. Copyright 2012, American Chemical Society.

Thus, I considered that the use of PADs in blood tests not only addresses the problems of conventional blood tests but also provides an on-site, user-friendly analytical method. The drawbacks of using PADs in blood tests are two-fold: requirement of (i) plasma separation and (ii) an accurate volume manipulation of the

separated plasma. Several approaches of (i) plasma separation and (ii) accurate volume manipulation of the separated plasma is introduced and described in Section **1.2.1**. The approach of plasma separation is to use plasma separation paper or the aggregation of red blood cells; both approaches can separate plasma by capturing red blood cells via pores. However, due to the dead volume of plasma inside the paper, it is necessary to use up to several hundred microliters of blood. Several approaches for accurate volume manipulation of liquid samples have been described in Section **1.2.1**. However, to date, an innovative technology that enables constant volume operation has not been established. Thus, the development of PADs that enable constant volume operation after separating plasma from a low blood volume is important to overcome the present drawbacks of PADs concerning blood tests. Subsequently, colorimetry, electrochemistry, fluorescence, and chemi/bio-chemiluminescence are used as PAD detection methods in blood tests. Among them, the colorimetric method is the simplest for easily obtaining results due to the rapid reaction and visual color change. Furthermore, quantitative analysis can be performed in combination with digital technology. In this thesis, the main objective is the development of PADs for low-cost, rapid, and straightforward measurement of components in human whole blood via colorimetry. The outline of this thesis is summarized in Fig. 1.17.

In Chapter 1, after a brief introduction of PADs, the current state and issues for the application of blood tests have been discussed by reviewing the recent literature on device development.

Chapter 2 described an evaluation of four different fabrication methods for PADs. To develop a PAD for use in blood tests by colorimetry, a selection of PAD fabrication methods is required. In this chapter, common fabrication methods, including craft cutting, wax printing, screen printing, and photolithography were used for PAD fabrication. Using PADs fabricated via four methods, various parameters — such as cost, fabrication accuracy, wicking rate, and analytical precision — were investigated and summarized. Through comparison with the investigated parameters, it was concluded that cutting and screen printing are the optimal methods of producing colorimetric PADs.

Chapter 3 evaluated the method of image analysis for multi-color detection in μPADs, using CIE *L*a*b** color space. For multi-analyte detection, color signals are specific to the selected reaction and are

diverse. In the future, to detect multi-analytes in whole blood by colorimetry, the technique of image analysis that enables a display on a single graph of multicolor signals generated from multi targets in a single graph will be desired. The pH detection is used as the model of multi-color change and to demonstrate the multi-color development (pH 2 – 9) on the μPAD. Then, calibration curves (pH versus each color intensity) are obtained using the RGB scale and CIE *L*a*b** color space via image analysis. For the RGB scale, the change in color intensity depending on pH was not observed. In contrast, the color difference (ΔE) obtained from CIE *L*a*b** color space showed that the ΔE value increased monotonously with increasing pH value, with small standard deviations. Therefore, the combination of the PAD and image analysis based on CIE *L*a*b** color space will enable quantitative analysis of the detection of multi-analytes in whole blood via colorimetry.

Chapter 4 described the development of the PAD for determining the lithium ion concentration in human blood. The development of PADs that enable plasma separation from a low blood volume and volume control of the separated plasma is important to overcome the present drawbacks of using PADs in blood tests. To address these drawbacks, a PAD was designed that consisted of a blood cell separation unit and a detection unit for detecting the lithium ion concentration. The developed PAD exhibited good measurement performance, comparable with that of conventional methods. Finally, the PAD was used to determine the lithium ion concentration in whole blood and exhibited a high recovery rate with high reproducibility. Thus, I succeeded in developing a PAD for determining lithium ion concentration in human blood.

Chapter 5 described the development of automatic PAD for determining the lithium ion concentration in human blood. The developed PAD in Chapter 4 still requires improvements, e.g.: (i) further reduction of required blood volume and (ii) no pipetting when loading a certain volume of whole blood. To achieve (i) and (ii), I invented a fusion device that comprises a digital microfluidics (DMF) unit and PAD unit, comprised of five circle-shaped PADs: DMF can provide the plasma separation, division, transportation, introduction of a precise volume of the plasma; the PADs concentrated the detection reagent can detect lithium ions by absorbing the transported plasma droplet. Dielectrophoresis was used for the plasma separation and was able to separate highly pure plasma within 5 min: the plasma volume depended upon the device dimension; the successful

separation volume was in the range of 20 to 400 nL. Subsequently, the fusion device was able to detect lithium ion concentration and its measurement performance was comparable to conventional methods. Finally, the fusion device was used to determine the lithium ion concentration in whole blood and the whole detection process was successfully completed within 20 minutes. The results obtained by this method agreed very well with the conventional methods. Thus, I succeeded in developing the fusion device for determining lithium ion concentration in human whole blood.

Chapter 6 summarized the results of this thesis and the prospects of this research.

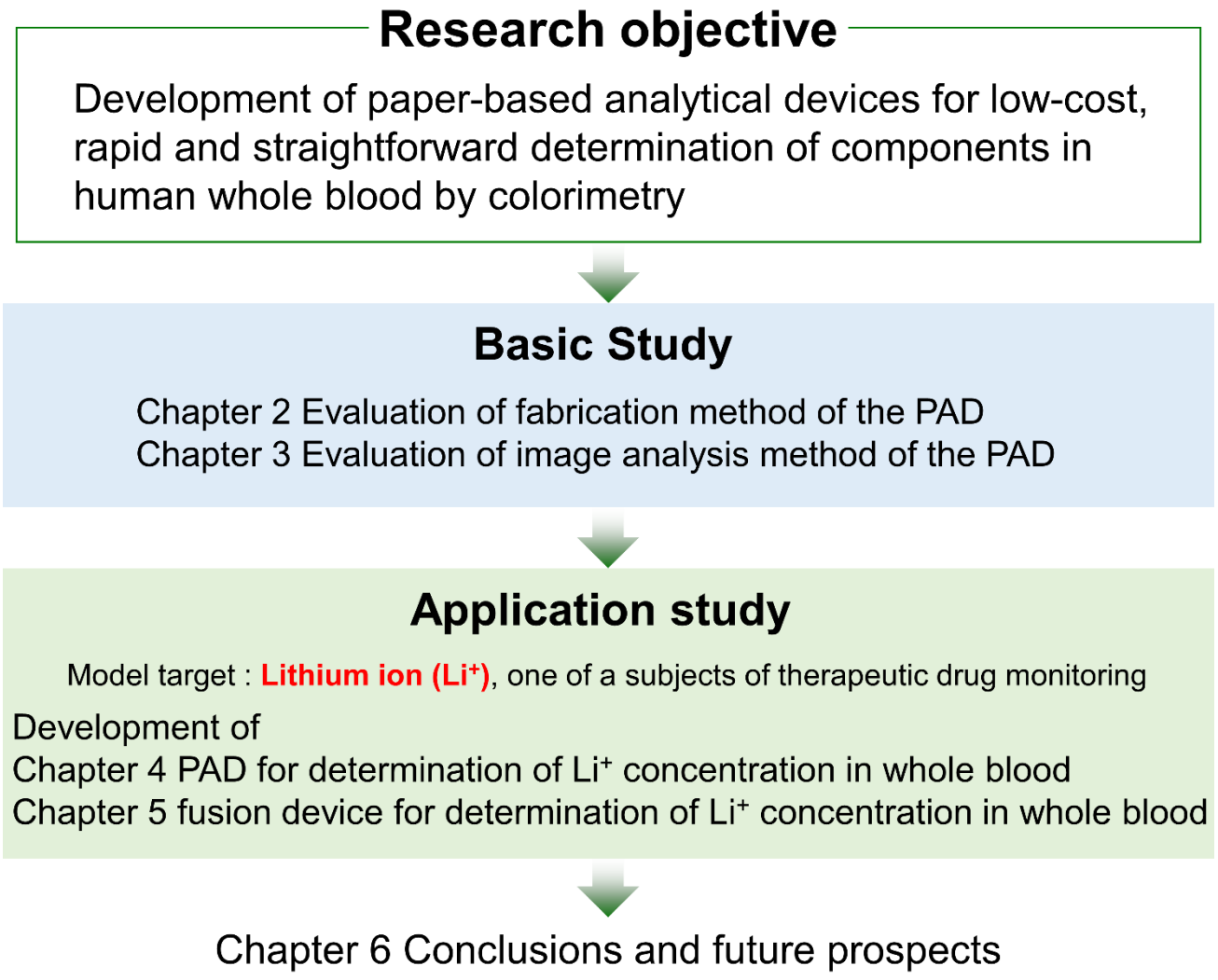

Figure 1.17 Outline of this thesis.

References

[1] H. Yagoda, *Ind. Eng. Chem. Res.*, **9**, 79-82 (1937).

[2] R. H. Muller, and D. L. Clegg, *Anal. Chem.*, **21**, 1123-1125 (1949).

[3] D. Z. Silver, and R. Bookman, *Anal.l Chem.*, **28**, 558-558 (1956).

[4] D. M. Abelson, and J. G. C. Fox, *J. Clin. Pathol.*, **12**, 375-376 (1959).

[5] B. M. Johnstone, and G. P. Briner, *J. Chromatogr.*, **2**, 513-518 (1959).

[6] J. W. Porteous, *J. Chromatogr.*, **2**, 58-64 (1959).

[7] G. Smiljanic, and T. Rabuzin, *Rev. Sci. Instrum.*, **36**, 160-163 (1959).

[8] B. L. Vanduuren, *Anal. Chem.*, **32**, 732-733 (1960).

[9] D. Dearnaley, and R. M. Acheson, *J. Chromatogr.*, **5**, 452 (1961).

[10] J. S. Matthews, *Analyst*, **87**, 911-& (1962).

[11] C. H. Coleman, Journal of the Association of Official Agricultural Chemists, **46**, 770-+ (1963).

[12] G. W. Perold, Vanstade.Jm, and H. J. Jacobs, *Analyst*, **89**, 297-& (1964).

[13] J. W. Boag, P. S. Bond, Tramerza.Z, E. M. Fielden, and H. Hodt, *J. Chromatogr.*, **73**, 265-& (1972).

[14] G. Kasang, and H. Rembold, *J. Chromatogr.*, **71**, 101-& (1972).

[15] A. W. Martinez, S. T. Phillips, M. J. Butte, and G. M. Whitesides, *Angew. Chem. Int. Ed.*, **46**, 1318-1320 (2007).

[16] D. A. Bruzewicz, M. Reches, and G. M. Whitesides, *Anal. Chem.*, **80**, 3387-3392 (2008).

[17] A. W. Martinez, S. T. Phillips, E. Carrilho, S. W. Thomas, H. Sindi, and G. M. Whitesides, *Anal. Chem.*, **80**, 3699-3707 (2008).

[18] A. W. Martinez, S. T. Phillips, and G. M. Whitesides, *Proc. Natl. Acad. Sci. U.S.A.*, **105**, 19606-19611 (2008).

[19] A. W. Martinez, S. T. Phillips, B. J. Wiley, M. Gupta, and G. M. Whitesides, *Lab. Chip*, **8**, 2146-2150 (2008).

[20] A. Manz, N. Graber, and H. M. Widmer, *Sens. Actuators B Chem.*, **1**, 244-248 (1990).

[21] D. J. Harrison, K. Fluri, K. Seiler, Z. H. Fan, C. S. Effenhauser, and A. Manz, *Science*, **261**, 895-897 (1993).

[22] P. C. Simpson, D. Roach, A. T. Woolley, T. Thorsen, R. Johnston, G. F. Sensabaugh, and R. A. Mathies, *Proc. Natl. Acad. Sci. U.S.A.*, **95**, 2256-2261 (1998).

[23] Y. N. Xia, and G. M. Whitesides, *Annu. Rev. Mater. Sci.*, **28**, 153-184 (1998).

[24] E. O. a. A. v. d. B. R. E. Oosterbroek, Lab-on-a-chip. Miniaturized Systems for (Bio)Chemical Analysis and Synthesis (Elsevier, 2003).

[25] D. J. Laser, and J. G. Santiago, *J Micromech Microeng*, **14**, R35-R64 (2004).

[26] J. Clayton, *Nat. Methods*, **2**, 621-627 (2005).

[27] N. T. Nguyen, and Z. G. Wu, *J Micromech Microeng*, **15**, R1-R16 (2005).

[28] K. Mahato, A. Srivastava, and P. Chandra, *Biosens. Bioelectron.*, **96**, 246-259 (2017).

[29] A. K. Yetisen, M. S. Akram, and C. R. Lowe, *Lab. Chip*, **13**, 2210-2251 (2013).

[30] K. Yamada, H. Shibata, K. Suzuki, and D. Citterio, *Lab. Chip*, **17**, 1206-1249 (2017).

[31] Y. Y. Xia, J. Si, and Z. Y. Li, *Biosens. Bioelectron.*, **77**, 774-789 (2016).

[32] D. M. Cate, J. A. Adkins, J. Mettakoonpitak, and C. S. Henry, *Anal. Chem.*, **87**, 19-41 (2015).

[33] J. Hu, S. Q. Wang, L. Wang, F. Li, B. Pingguan-Murphy, T. J. Lu, and F. Xu, *Biosen. Bioelectron.*, **54**, 585-597 (2014).

[34] M. M. Gong, and D. Sinton, *Chem. Rev.*, **117**, 8447-8480 (2017).

[35] C. H. Liu, C. A. Chen, S. J. Chen, T. T. Tsai, C. C. Chu, C. C. Chang, and C. F. Chen, *Anal. Chem*., **91**, 1247-1253 (2019).

[36] S. Vemulapati, and D. Erickson, *Anal. Chem.*, **91**, 14824-14828 (2019).

[37] C. Dixon, J. Lamanna, and A. R. Wheeler, *Lab. Chip*, **20**, 1845-1855 (2020).

[38] X. X. Yang, O. Forouzan, T. P. Brown, and S. S. Shevkoplyas, *Lab. Chip*, **12**, 274-280 (2012).

[39] A. Nilghaz, and W. Shen, *Rsc Adv.*, **5**, 53172-53179 (2015).

[40] W. J. Guo, J. Hansson, and W. van der Wijngaart, *Anal. Chem.*, **92**, 6194-6199 (2020).

[41] X. Li, J. F. Tian, T. Nguyen, and W. Shen, *Anal. Chem.*, **80**, 9131-9134 (2008).

[42] H. Fu, P. F. Song, Q. Y. Wu, C. Zhao, P. Pan, X. Li, N. Y. K. Li-Jessen, and X. Y. Liu, *Microsys. Nanoeng.*, **5**, 50 (2019).

[43] J. L. Han, A. J. Qi, J. R. Zhou, G. Wang, B. W. Li, and L. X. Chen, *ACS Sens*., **3**, 1789-1794 (2018).

[44] B. W. Li, L. J. Yu, J. Qi, L. W. Fu, P. Q. Zhang, and L. X. Chen, *Anal. Chem.*, **89**, 5708-5713 (2017).

[45] A. W. Martinez, S. T. Phillips, Z. H. Nie, C. M. Cheng, E. Carrilho, B. J. Wiley, and G. M. Whitesides, *Lab. Chip*, **10**, 2499-2504 (2010).

[46] B. R. Lutz, P. Trinh, C. Ball, E. Fu, and P. Yager, *Lab. Chip*, **11**, 4274-4278 (2011).

[47] E. Fu, T. Liang, P. Spicar-Mihalic, J. Houghtaling, S. Ramachandran, and P. Yager, *Anal. Chem.*, **84**, 4574-4579 (2012).

[48] G. E. Fridley, H. Le, and P. Yager, *Anal. Chem.*, **86**, 6447-6453 (2014).

[49] H. Liu, X. Li, and R. M. Crooks, *Anal. Chem.*, **85**, 4263-4267 (2013).

[50] B. Lutz, T. Liang, E. Fu, S. Ramachandran, P. Kauffman, and P. Yager, *Lab. Chip*, **13**, 2840-2847 (2013).

[51] J. Houghtaling, T. Liang, G. Thiessen, and E. Fu, *Anal. Chem.*, **85**, 11201-11204 (2013).

[52] W. Dungchai, O. Chailapakul, and C. S. Henry, *Anal. Chem.*, **81**, 5821-5826 (2009).

[53] Z. H. Nie, F. Deiss, X. Y. Liu, O. Akbulut, and G. M. Whitesides, *Lab. Chip*, **10**, 3163-3169 (2010).

[54] J. Noiphung, T. Songjaroen, W. Dungchai, C. S. Henry, O. Chailapakul, and W. Laiwattanapaisal, *Analy. Chim. Acta*, **788**, 39-45 (2013).

[55] F. Y. Kong, S. X. Gu, W. W. Li, T. T. Chen, Q. Xu, and W. Wang, *Biosens. Bioelectron.*, **56**, 77-82 (2014).

[56] R. Canovas, M. Parrilla, P. Blondeau, and F. J. Andrade, *Lab. Chip*, **17**, 2500-2507 (2017).

[57] S. Chaiyo, E. Mehmeti, W. Siangproh, T. L. Hoang, H. P. Nguyen, O. Chailapakul, and K. Kalcher, *Biosens. Bioelectron.*, **102**, 113-120 (2018).

[58] C. C. Wang, J. W. Hennek, A. Ainla, A. A. Kumar, W. J. Lan, J. Im, B. S. Smith, M. X. Zhao, and G. M. Whitesides, *Anal. Chem.*, **88**, 6326-6333 (2016).

[59] P. Wang, Z. Y. Cheng, Q. Chen, L. L. Qu, X. M. Miao, and Q. M. Feng, *Sens. Actuators B Chem.*, **256**,

931-937 (2018).

[60] Y. Wang, J. P. Luo, J. T. Liu, X. R. Li, Z. Kong, H. Y. Jin, and X. X. Cai, *Biosens. Bioelectron.*, **107**, 47-53 (2018).

[61] Y. F. Wu, P. Xue, Y. J. Kang, and K. M. Hui, *Anal. Chem.*, **85**, 8661-8668 (2013).

[62] G. Scordo, D. Moscone, G. Palleschi, and F. Arduini, *Sens. Actuators B Chem.*, **258**, 1015-1021 (2018).

[63] B. Wei, K. Mao, N. Liu, M. Zhang, and Z. G. Yang, *Biosens. Bioelectron.*, **121**, 41-46 (2018).

[64] S. Boonkaew, S. Chaiyo, S. Jampasa, S. Rengpipat, W. Siangproh, and O. Chailapakul, *Microchimica Acta* **186**, 153 (2019).

[65] Y. Boonyasit, O. Chailapakul, and W. Laiwattanapaisal, *Biosens. Bioelectron.*, **130**, 389-396 (2019).

[66] N. Ruecha, K. Shin, O. Chailapakul, and N. Rodthongkum, *Sens. Actuators B Chem.*, **279**, 298-304 (2019).

[67] S. Cinti, E. Proietti, F. Casotto, D. Moscone, and F. Arduini, *Anal. Chem.*, **90**, 13680-13686 (2018).

[68] X. L. Sun, H. Wang, Y. N. Jian, F. F. Lan, L. N. Zhang, H. Y. Liu, S. G. Ge, and J. H. Yu, *Biosens. Bioelectron.*, **105**, 218-225 (2018).

[69] M. N. Tsaloglou, A. Nemiroski, G. Camci-Unal, D. C. Christodouleas, L. P. Murray, J. T. Connelly, and G. M. Whitesides, *Anal.l Biochem.*, **543**, 116-121 (2018).

[70] H. Wang, Y. N. Jian, Q. K. Kong, H. Y. Liu, F. F. Lan, L. L. Liang, S. G. Ge, and J. H. Yu, *Sens. Actuators B Chem.*, **257**, 561-569 (2018).

[71] S. Cinti, G. Cinotti, C. Parolo, E. P. Nguyen, V. Caratelli, D. Moscone, F. Arduini, and A. Merkoci, *Anal. Chem.*, **92**, 1674-1679 (2020).

[72] M. Novell, T. Guinovart, P. Blondeau, F. X. Rius, and F. J. Andrade, *Lab. Chip*, **14**, 1308-1314 (2014).

[73] H. Wang, C. X. Zhou, X. L. Sun, Y. N. Jian, Q. K. Kong, K. Cui, S. G. Ge, and J. H. Yu, *Biosens. Bioelectron.*, **117**, 651-658 (2018).

[74] S. G. Ge, L. Ge, M. Yan, X. R. Song, J. H. Yu, and S. S. Liu, *Biosens. Bioelectron.*, **43**, 425-431 (2013).

[75] Z. L. Qiu, J. Shu, and D. P. Tang, *Anal. Chem.*, **89**, 5152-5160 (2017).

[76] M. Y. He, and Z. H. Liu, *Anal. Chem.*, **85**, 11691-11694 (2013).

[77] E. Petryayeva, and W. R. Algar, *Analyst*, **140**, 4037-4045 (2015).

[78] J. T. Connelly, J. P. Rolland, and G. M. Whitesides, *Anal. Chem.*, **87**, 7595-7601 (2015).

[79] G. L. Xu, D. Nolder, J. Reboud, M. C. Oguike, D. A. van Schalkwyk, C. J. Sutherland, and J. M. Cooper, *Angew. Chem. Int. Ed.*, **55**, 15250-15253 (2016).

[80] S. W. Hu, S. Qiao, B. Y. Xu, X. Peng, J. J. Xu, and H. Y. Chen, *Anal. Chem.*, **89**, 2131-2137 (2017).

[81] J. X. Wang, J. D. Dai, Y. Q. Xu, X. H. Dai, Y. L. Zhang, W. D. Shi, B. Sellergren, and G. Q. Pan, *Small*, **15**, 1803913 (2019).

[82] J. F. Chang, H. Y. Li, T. Hou, W. N. Duan, and F. Li, *Biosens. Bioelectron.*, **104**, 152-157 (2018).

[83] W. R. Chu, Y. Chen, W. Liu, M. Zhao, and H. F. Li, *Sens. Actuators B Chem.*, **250**, 324-332 (2017).

[84] L. Ge, S. M. Wang, X. R. Song, S. G. Ge, and J. H. Yu, *Lab. Chip*, **12**, 3150-3158 (2012).

[85] S. M. Wang, L. Ge, X. R. Song, M. Yan, S. G. Ge, J. H. Yu, and F. Zeng, *Analyst*, **137**, 3821-3827 (2012).

[86] M. Zhao, H. F. Li, W. Liu, Y. M. Guo, and W. R. Chu, *Biosens. Bioelectron.*, **79**, 581-588 (2016).

[87] W. Liu, C. L. Cassano, X. Xu, and Z. H. Fan, *Anal. Chem.*, **85**, 10270-10276 (2013).

[88] F. Li, J. C. Liu, L. Guo, J. H. Wang, K. Q. Zhang, J. B. He, and H. Cui, *Biosens. Bioelectron.*, **141**, 111472 (2019).

[89] K. Tenda, B. van Gerven, R. Arts, Y. Hiruta, M. Merkx, and D. Citterio, *Angew. Chem. Int. Ed.*, **57**, 15369-15373 (2018).

[90] Y. Li, L. L. Zhou, W. Ni, Q. Y. Luo, C. N. Zhu, and Y. H. Wu, *Anal. Chem.*, **91**, 14838-14841 (2019).

[91] M. L. Dong, J. D. Wu, Z. M. Ma, H. Peretz-Soroka, M. Zhang, P. Komenda, N. Tangri, Y. Liu, C. Rigatto, and F. Lin, *Sensors*, **17**, (2017).

[92] S. J. Vella, P. Beattie, R. Cademartiri, A. Laromaine, A. W. Martinez, S. T. Phillips, K. A. Mirica, G. M. Whitesides, *Anal. Chem.*, **84**, 2883-2891 (2012).

[93] H. Ki, J. Oh, G. R. Han, and M. G. Kim, *Lab. Chip*, **20**, 844-851 (2020).

[94] J. Kanter, M. J. Telen, C. Hoppe, C. L. Roberts, J. S. Kim, and X. X. Yang, *BMC Med.*, **13**, 225-232 (2015).

[95] M. Bond, B. Hunt, B. Flynn, P. Huhtinen, R. Ware, and R. Richards-Kortum, *Plos One*, **12**, (2017).

[96] R. N. Deraney, C. R. Mace, J. P. Rolland, and J. E. Schonhorn, *Anal. Chem.*, **88**, 6161-6165 (2016).

[97] S. Lathwal, and H. D. Sikes, *Lab. Chip*, **16**, 1374-1382 (2016).

[98] G. Svedberg, Y. Jeong, H. Na, J. Jang, P. Nilsson, S. Kwon, J. Gantelius, and H. A. Svahn, *Lab. Chip*, **17**, 549-556 (2017).

[99] J. Reboud, G. L. Xu, A. Garrett, M. Adriko, Z. G. Yang, E. M. Tukahebwa, C. Rowell, and J. M. Cooper, *Proc. Natl. Acad. Sci. U.S.A.*, **116**, 4834-4842 (2019).

[100] S. Kar, T. K. Maiti, and S. Chakraborty, *Analyst*, **140**, 6473-6476 (2015).

[101] R. Robinson, L. Wong, R. J. Monnat, and E. Fu, *Micromachines*, **7**, 28-38 (2016).

[102] W. R. Tan, L. Y. Zhang, J. C. G. Doery, and W. Shen, *Lab. Chip*, **20**, 394-404 (2020).

CHAPTER 2 Evaluation of Fabrication Method of Paper-Based Analytical Devices

2.1 Introduction

Paper-based analytical devices (PADs) have great advantages, such as low cost, being easy to mass produce, use, carry around, and disposal after use.[1] For these reasons, PADs are to be popular alternative devices to conventional ones for food safety analysis [2,3], environmental monitoring [4,5], and point-of-care diagnosis [6-9]. The PADs have been fabricated by a variety of methods, including (1) photolithography [10-12], (2) wax printing [12-14], (3) inkjet printing [15-18], (4) screen printing [19-22], and (5) craft cutting [23-25]. The main advantages and disadvantages of each fabrication method may be summarized as follows.

Method (1): The apparatus for photolithography is expensive, procedures are complicated, and a long fabrication time is required in comparison with the other fabrication methods. However, photolithography can fabricate channel patterns with high resolution.[10-12]

Methods (2), (3) and (4): These printing methods enable low cost and easy fabrication. Method (5): Craft cutting machines are inexpensive. However, it is difficult for them to create microchannels on a paper precisely.

The various parameters of fabricated PADs, such as cost, wicking rate, and edge clarity, have also been reported, and the fabrication methods affect these parameters.[1,11,26,27] In addition, I previously demonstrated the effect of a paper substrate on the sensitivity of PADs.[12,28] The suitable fabrication method should be selected according to the target analytes and types of paper substrate. Some articles [1,11,26,27] have compared the precision, cost, and ease of the fabrication methods of PADs as summaries of experimental results from several research groups. However, the effect of fabrication method on the analytical properties of colorimetric PADs has not been well investigated.

Here I considered the evaluation of the PAD fabrication method for selecting the suitable fabrication method to develop the colorimetric PAD towards blood tests. The investigated properties are cost, fabrication accuracy, wicking rate and analytical precision for developing colorimetric PADs of blood tests. I selected the fabrication methods of photolithography, wax printing, screen printing, and craft cutting, because these

methods are widely used for PAD fabrication and the characteristics, as well as the advantages and disadvantages, of the methods are significantly different. The evaluations of fabrication methods and the PADs themselves provide valuable information for developing novel colorimetric PADs of blood tests and the promise of PADs with better performance features.

2.2 Experimental

2.2.1 Reagents and chemicals

Whatman chromatography paper #1 was purchased from GE Healthcare Japan Co., Ltd. (200 × 200 mm, thickness = 0.18 mm, Tokyo, Japan) and used as a substrate for μPAD devices. SU-8 2010 photoresist and SU-8 developer were obtained from Microchem (Westborough, MA, USA). Isopropanol, used to remove unreacted SU-8 developer, was purchased from Wako Pure Chemical Industries, Ltd. (Osaka, Japan). Polydimethylsiloxane (PDMS, SILPOT 184 CAT), used as hydrophobic ink for screen printing, was purchased from Dow Corning Toray Co., Ltd. (Tokyo, Japan). For edge observations, a 1 mM phenolphthalein solution was prepared by dissolving phenolphthalein (special grade, Kanto Chemical Co., Inc., Tokyo, Japan) in ultrapure water (Millipore water purification system, 18 MΩ cm, Milli-Q, Millipore, Bedford, MA, USA) and added 0.1 mM NaOH. To measure the wicking rate, 9 mM bromothymol blue (Wako special grade, Wako Pure Chemical Industries) was prepared by dissolving in 95% ethanol. Albumin, from bovine serum (Wako 1st grade) was obtained from Wako Pure Chemical Industries and used with ultrapure water to prepare BSA standard solutions (0, 20, 40 and 60 μM). A citrate buffer solution (250 mM, pH 1.8) was prepared by mixing (41 : 8 v/v) of a 250 mM trisodium citrate dihydrate solution (special grade, Wako Pure Chemical Industries, Ltd.) and a 250 mM citric acid solution (special grade, Kishida Chemical Co., Ltd., Osaka, Japan). To measure the BSA concentration, 9 mM tetrabromophenol blue (TBPB, Sigma-Aldrich Co., Inc.) was prepared by dissolving in 95% ethanol.

2.2.2 Pattern designs and fabrication procedures of PADs by four methods

The patterns of the photomasks for photolithography were designed using AutoCAD 2015 (Autodesk, Inc., CA, USA), and then obtained from Unno Giken Co., Ltd. (Tokyo, Japan). The pattern of the hydrophobic barrier for the PAD was designed using Inkscape and Adobe Illustrator (Adobe Systems Inc., Tokyo, Japan), for wax- and screen-printing methods, respectively. The pattern for the craft cut PAD was designed using Silhouette Studio software (GRAPHTEC Corp., Kanagawa, Japan). As shown in Fig. 2.1, the channel design of the PAD had eight channels connected to eight separate detection zones (φ = 4 mm) located around the buffer introduction zone (φ = 12 mm).

The PAD was fabricated by standard photolithography procedures reported previously [12, 28]. A piece of chromatography paper #1 (the substrate) was cut to the same size as a photomask (Unno Giken Co., Ltd., Tokyo, Japan) and the paper substrate was immersed into the photoresist. A spin coater (MS-A100, Mikasa Co., Ltd., Toyo, Japan) was used to remove the excess photoresist. After spin coating, the paper substrate was baked on a hotplate at 95 ˚C for 5 minutes, and then removed from the hotplate and cooled to room temperature. The paper substrate was aligned with the photomask and exposed to UV radiation using a mask aligner M-1S-type (Mikasa Co., Ltd.). The UV-irradiated paper was placed on the hotplate at 95 ˚C for 5 minutes. After cooling to room temperature, the paper substrate was immersed into the SU-8 developer for 6 minutes. Finally, the channel-patterned paper was rinsed with isopropanol and dried with an air-gun to get the PAD.

Fabrication protocol for screen printing of the PAD was reported previously [19, 29]. In brief, a screen stencil was designed to arrange the 36 paper device patterns in the printing area. The paper substrate was fixed to the screen printing apparatus using a vacuum pump unit. Degassed PDMS ink was poured onto the screen stencil on the paper substrate. The PDMS ink was rubbed into the stencil using a squeegee for the optimized number of times for the PAD. The PDMS screen printed PAD was heated in the oven at 120 ˚C for

30 minutes. Then, it was removed from the oven and cooled at room temperature. Finally, the PAD was cut into a suitable size for the experiments.

The pattern of the hydrophobic barrier for the PAD was designed using Inkscape software. A Xerox Tektronix PHASER 850 wax printer was used to create channel patterns on a paper substrate for the PAD. The wax printed PAD was put into an oven at 120 ˚C for 2 minutes. Then, it was removed from the oven and cooled to room temperature. Finally, the PAD was cut into a suitable size for the experiments.

The standard craft cutting method [4] was employed with a minor modification. The PAD pattern was designed using the Silhouette Studio software. The paper substrate was set in a craft cutting machine and the cutting condition was set at 3 cm/s. This gave the craft cut PAD in a ready to use form.

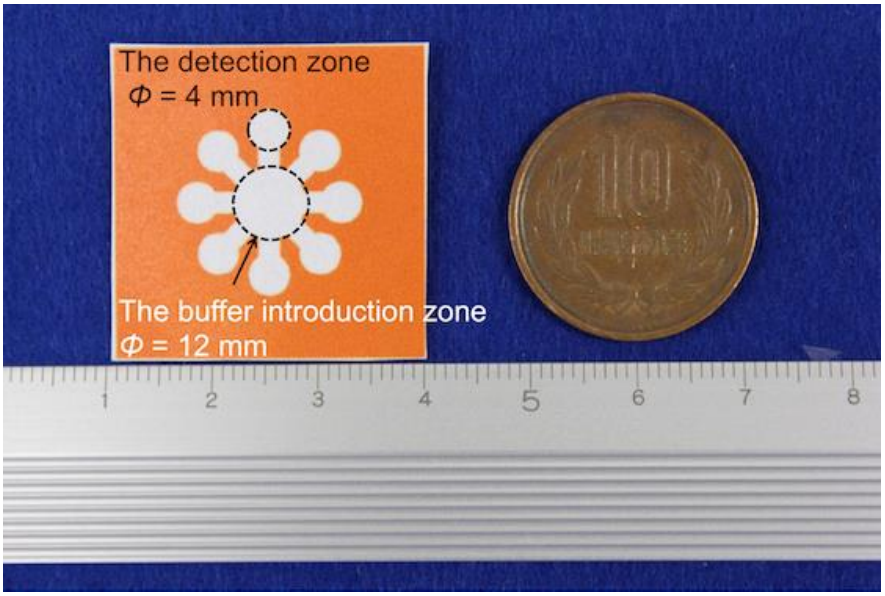

Figure 2.1 Photograph of the PAD used in this study. Its channel design consists of eight channels connecting to eight separate detection zones (φ=4 mm) which are located around the central detection and buffer introduction zone (φ=12 mm).

2.2.3 Protein assay procedure

First, 15 μL of a 250 mM citrate buffer solution (pH 1.8) was introduced into the buffer zone and was evaporated using a dryer for 2 min. Then, 15 μL of a 9 mM TBPB solution in 95% ethanol was introduced into the buffer zone and was evaporated using a dryer for 5 min. Finally, 3.5 μL of BSA solutions of different concentrations was separately spotted onto the eight detection zones. Colorimetry was used as the detection method. The distance between the PAD and a digital camera (EOS Kiss X6i, Canon, Tokyo, Japan) was *ca.* 20 cm, and images of the PADs were taken using a digital camera under fluorescent lighting conditions. The color information was measured with an image analysis software program (ImageJ Ver. 1.48).

2.3 Results and discussion

2.3.1 Evaluation of fabrication efficiency

In Table 2.1, I summarize my comparison of the PADs fabricated by the four types of methods. First, I evaluated the ease of implementing each PAD fabrication method. I fabricated the PADs as shown in Fig. 2.2. Wax printing, screen printing, and craft cutting methods were very simple; especially, screen printing only required rubbing PDMS ink on the stencil several times using a squeegee to get ink penetration into the paper substrate. Wax printing and craft cutting could automatically fabricate PADs using the respective apparatuses. However, photolithography included many fabrication steps and took a long time.

Table 2.1 Investigation of the effects of fabrication methods on the properties:

cost, fabrication accuracy, wicking rate and analytical precision, of μPADs using four types of fabrication methods

	Photolithography	Wax printing	Screen printing	Craft cutting
Ease of fabrication	×	◎	◎	◎
Fabrication time	×	◎	○	○
Raw materials costs*	~$ (US) 7.11/device	~$ (US) 1.55/device	~$ (US) 0.0376/device	~$ (US) 1.82/device
Fabrication efficiency	4 devices/h	10 devices/h	54 devices/h	12devices/h
Pattering precision	◎	×	○	◎
SEM observation	○	×	◎	◎
Wicking rate (TB)	0.724 mm/s	0.574 mm/s	0.853 mm/s	0.960 mm/s
Wicking rate (SPW)	0.831 mm/s	0.810 mm/s	1.37 mm/s	1.97 mm/s
Instrument costs	~$ (US) 100,000	~$ (US) 3,000	~$ (US) 3,000	~$ (US) 300
Characteristics	Sharp designs can be created. Plasma treatment is required.	Simple and fast fabrication. The leakage of solution should be prevented to improve the cross-contamination.	Easy fabrication. The μPAD indicates good properties.	Automated fabrication of many devices at one time. The μPAD is the fastest wicking rate and evaporation.

◎ Great result.

○ Good result.

× Bad result.

* Raw material costs are not included a cost of the fabricating instrument.

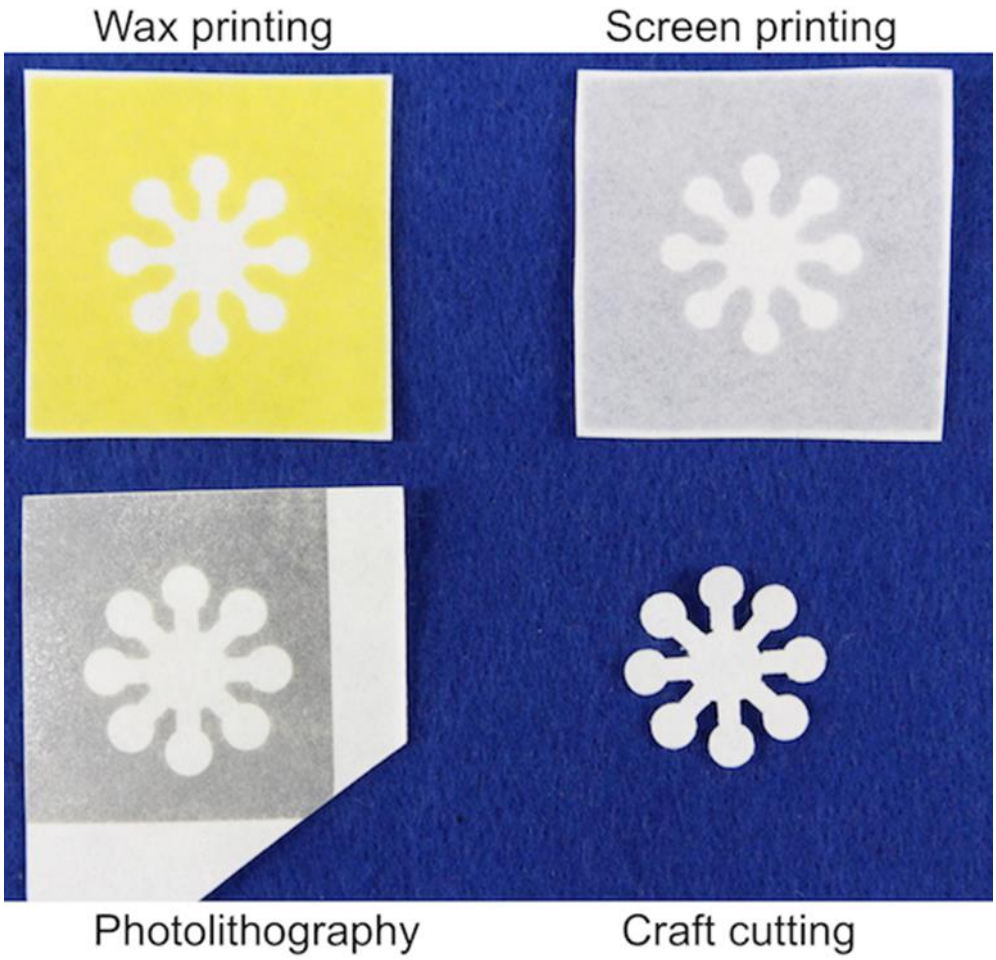

Figure 2.2 The PAD fabricated by photolithography, wax printing, screen printing and craft cutting.

Then, I evaluated the fabrication throughput for the PADs using each method. The fabrication efficiencies (as devices/fabrication at once) were 4, 12, 36, and 10, for photolithography, wax printing, screen printing, and craft cutting, respectively. Although the fabrication efficiency depends on the channel pattern, screen printing had the highest fabricating efficiency among the four fabrication methods. I used a stencil with a 20-cm square printing area, and the PAD size was 3-cm square. I was able to fabricate 36 PADs at one time. The UV irradiation area of a typical mask aligner was 6-8 cm square. According to literature, I can assume the throughput of the number of fabricating PADs (~2 cm square) to be 9-16 devices at one time.[10] Photolithography, in comparison, could fabricate only four PADs at once due to the limited UV irradiation area

(about an 8-cm square) and the size of the PAD (about a 3-cm square). Wax printing and craft cutting had similar fabrication throughputs.

I also focused on the fabrication costs, calculated from the raw material costs, including the paper (Whatman chromatography paper #1: $40/100 papers) and reagents. The raw material costs were calculated as follows:

Five mL of SU-8 2010 ($2290/L) and 200 mL of SU-8 developer ($85/L) were used for photolithography. Seven g of PDMS ($0.136/g) was used for screen printing. The costs of the wax ink and cutting sheet were $36/color-ink and $12/sheet. From the material costs including the paper cost, I estimated the fabrication costs of PADs. For photolithography, wax printing, screen printing, and craft cutting, the respective fabrication costs were estimated to be ~$7.11, ~$1.82, ~$0.0376, and ~$1.55, and the respective apparatus costs were ~$100,000, ~$3,000, ~$3,000, and ~$300.

2.3.2 Evaluation of the patterning ability

I evaluated the patterning ability of each fabrication method. To prevent leakage of the solutions and contaminations, the hydrophobic and hydrophilic areas should be clearly patterned on the paper substrate. In this paper, I define the microchannel clearly patterned by hydrophobic ink as good channel patterning. Therefore, I observed the boundary between the hydrophobic area and hydrophilic area constituting the microchannel of the PADs (topside and backside) using a benchtop SEM (proX PREMIUM, Phenom World Co., Ltd.). Figures 2.3a, b show SEM images of the PAD fabricated by photolithography. The boundary between the hydrophobic and hydrophilic areas was clearly formed on the topside. However, it was not clearly formed on the backside of the PAD. I assume that the photoresist could not completely crosslink due to poorer UV exposure on the paper backside. I can improve patterning of the channel design by using a thinner paper substrate or having an additional UV irradiation from the substrate backside. Figures 2.3c, d show SEM images of the PAD fabricated by screen printing. For screen printing, the boundary between the hydrophobic

and hydrophilic areas was clearly formed on both paper sides and the method showed the best channel patterning capability. The amount of PDMS ink can be adjusted depending on the paper substrate and channel design [19]. The optimal amount of PDMS ink and the rubbing frequency make it possible to fabricate PADs with good channel patterning.

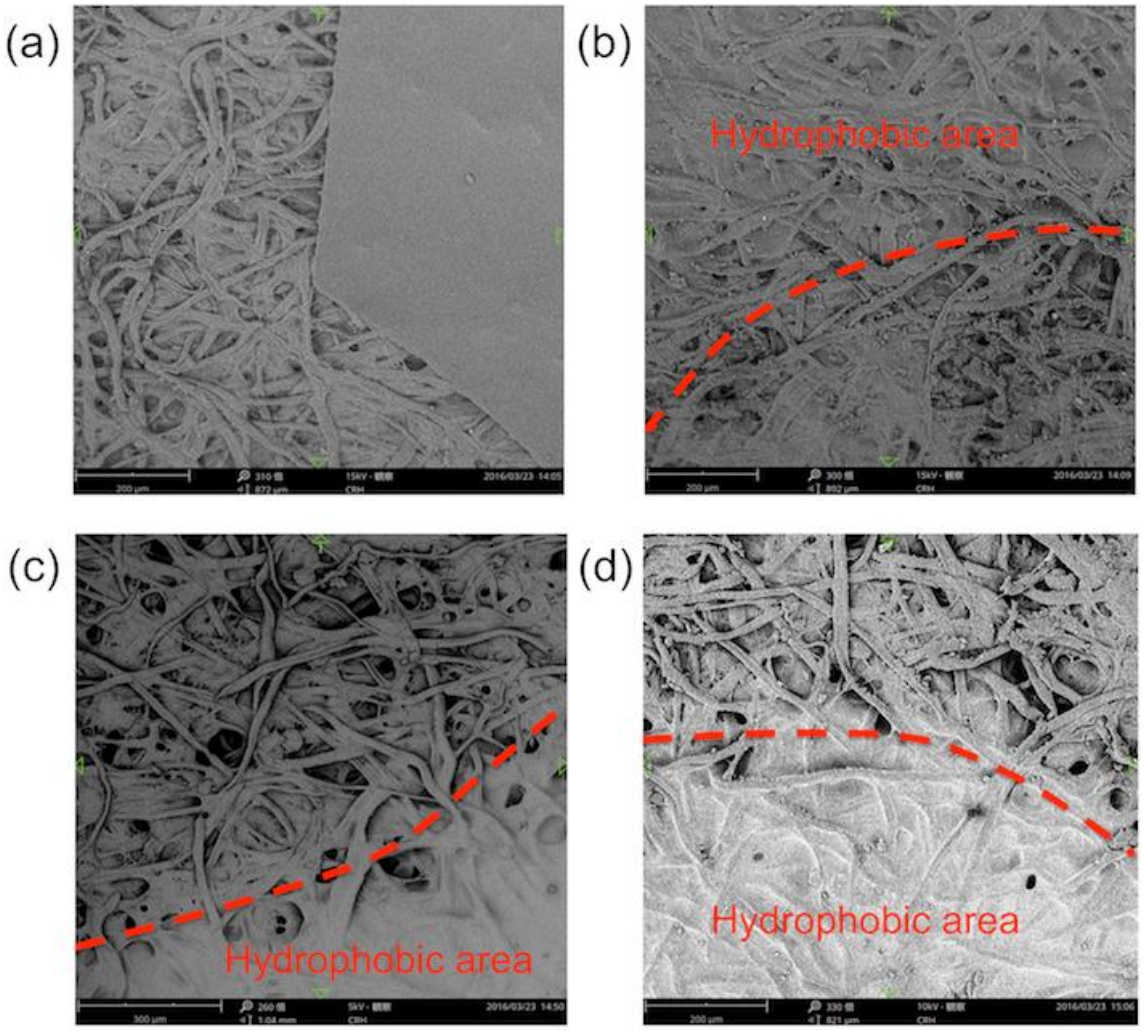

Fig. 2.3 Boundary between the hydrophobic area and the hydrophilic area of the PAD (topside and backside) observed using a benchtop SEM. The left images (a, c) are the top side and the right images (b, d) are the back side of the PAD. (a, b) show SEM images of the PAD fabricated by photolithography and (c, d) show SEM images of the PAD fabricated by screen printing.

On the other hand, I did not confirm any significant difference between both sides of the PADs fabricated by wax printing and craft cutting, as shown in Fig. 2.4a,b. The channel design of the PAD fabricated by wax printing was clearly patterned as shown in Fig. 2.2. However, the amount of printed wax ink was not enough to make the boundary between the hydrophobic and hydrophilic areas of the PAD. For this reason, I consider that the wax ink could not penetrate uniformly into the cellulose fibers, and this might affect the performance of the PAD. Wax printing can fabricate a completely patterned PAD by controlling the melting point and heating time of the wax ink to prevent cross-contamination. In the case of craft cutting, all bare cellulose fibers were observed because it did not use chemicals (Fig. 2.4c, d).

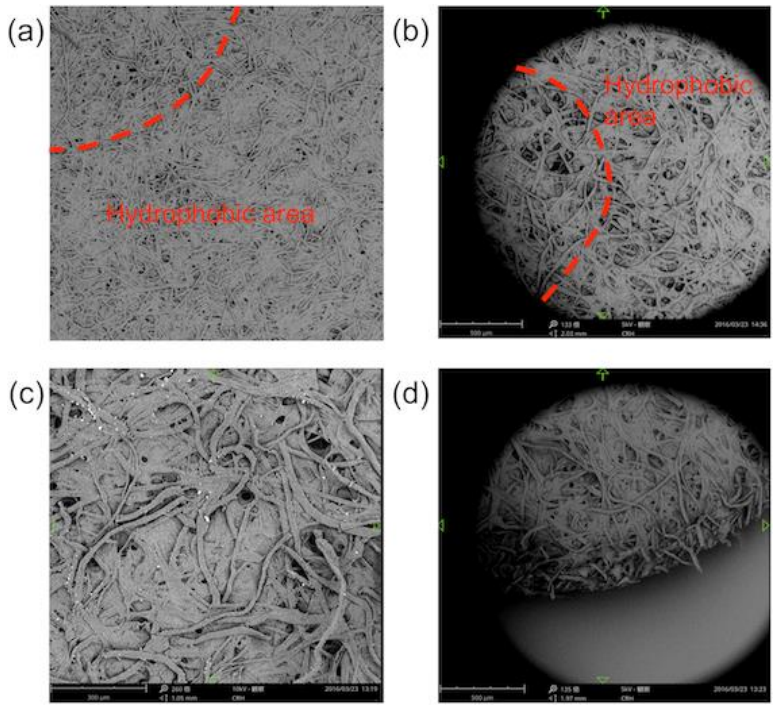

Fig. 2.4 Boundary between the hydrophobic area and the hydrophilic area of the PAD (topside and backside) observed using a benchtop SEM. The left images are the topside and the right images are the backside of the PAD. Figures 2.4a,b show the SEM images of the PAD fabricated by wax printing and Figs. 2.4c, d show the SEM images of the PAD fabricated by craft cutting.

Then, a 1 mM phenolphthalein solution was pipetted onto each PAD to observe the formed channel pattern. The PAD fabricated by photolithography underwent an oxygen plasma treatment to increase the hydrophilicity. Figure 2.5 shows photographs of PADs when the phenolphthalein solution was introduced. In the case of wax printing, the phenolphthalein solution flowed out from the buffer introduction zone. I think that the wax printed PAD did not form a complete hydrophobic barrier (Fig. 2.4 a,b) due to insufficient wax ink on the paper substrate. In the case of photolithography, phenolphthalein solution did not fill every part of the PAD and there was slight leakage out to the hydrophobic area. This result indicates the hydrophilicity of the whole PAD (the extent of the hydrophobic and hydrophilic areas) was increased by the oxygen plasma treatment and it led to a penetration of the phenolphthalein solution into the hydrophobic area. In the case of craft cutting, I did not observe any leakage of the phenolphthalein solution from the buffer introduction zone of the PAD put on pinholders, because the craft cut PAD had only the hydrophilic area based on the presence of bare cellulose fibers. From these results, I conclude that the photolithography method can produce the sharpest channel among the four methods, although the fabrication methods would affect the performance of the PADs, including their wicking rate, sensitivity, and precision of analysis. In the next section, I therefore evaluate the wicking rate of the PADs.

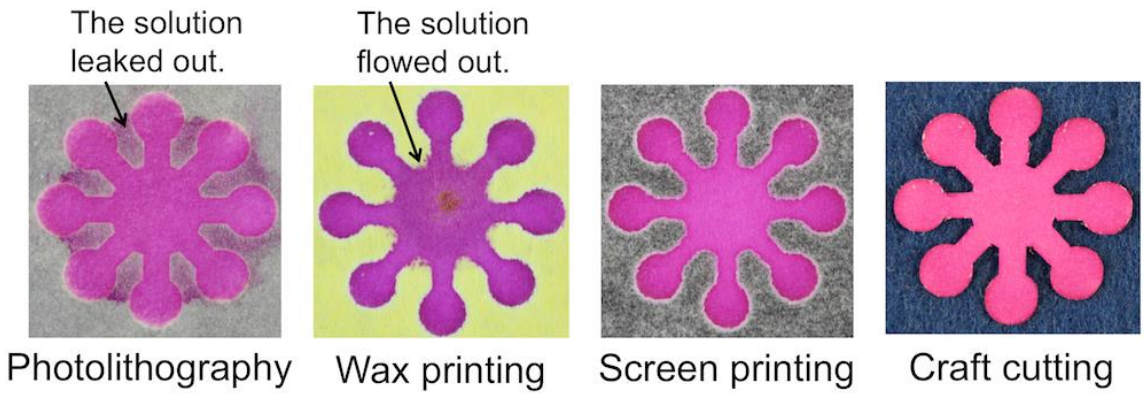

Fig. 2.5 Patterning precision evaluation using a 1 mM phenolphthalein solution for PADs fabricated by the four methods.

2.3.3 Evaluation of the wicking rate

To evaluate the wicking rate changing of four fabrication methods, I measured the wicking rate of the PADs using 9 mM bromothymol blue (dissolved in 95 % ethanol). First, 15 μL of 9 mM bromothymol blue or ultrapure water was dropped onto the center part of the buffer introduction zone. Then, I measured the time for the solution to reach the detection zone. The wicking rates of bromothymol blue were 0.724 (RSD = 3.41 %), 0.574 (6.23 %), 0.853 (1.92 %), and 0.960 (2.72 %) mm/s, for photolithography, wax printing, screen printing, and craft cutting, respectively (See Table 2.1). The wicking rates of the PADs fabricated by craft cutting and screen printing were faster than the other fabrication methods, because the channel areas were completely formed without any chemical processing. Contrary to my expectation, the PAD fabricated by photolithography had a moderate wicking rate. For this experiment, because the PAD had not undergone the oxygen plasma treatment, I consider that the organic solvent remained in the cellulose fibers, which promoted wicking of the ethanol-based solution. The PAD fabricated by wax printing had the slowest wicking rate due to unclear patterning of the channel design.

I also measured the wicking rate under the same experimental procedures using ultrapure water. Water dropped onto the PAD fabricated by photolithography without oxygen plasma treatment did not flow into the PAD (Fig. 2.6). I then used the PAD that had undergone the oxygen plasma treatment and measured the wicking rate of ultrapure water (Table 2.1). The wicking rates were 0.831 (RSD = 9.65 %), 0.810 (12.8 %), 1.37 (12.9 %), and 1.97 (5.04 %) mm/s, for photolithography, wax printing, screen printing, and craft cutting, respectively. Product information of Whatman chromatography paper #1 (thickness: 0.18 mm, weight: 87 g/m^2) is reported to be 130 mm/30 min (0.0722 mm/s). However, the provided wicking rate was measured by a different evaluation method from my case. I assume that the wicking rate of the PAD fabricated by craft cutting shows a similar value with typical chromatography paper, because the PAD is composed by bare cellulose fiber. Therefore, I compared the wicking rate of the craft cutting device and other devices. The wicking rates of the PADs fabricated by craft cutting and screen printing were also faster than the other fabrication methods, because the channel area were completely formed without any chemical processing. The

hydrophilicity of the PAD fabricated by photolithography was enhanced by the oxygen plasma treatment, and thus performance became the same as for the wax-printed PAD. These results indicate the fabrication methods affected the wicking property of PADs and their performance could be improved by selecting suitable fabrication methods, post treatment, and experimental conditions.

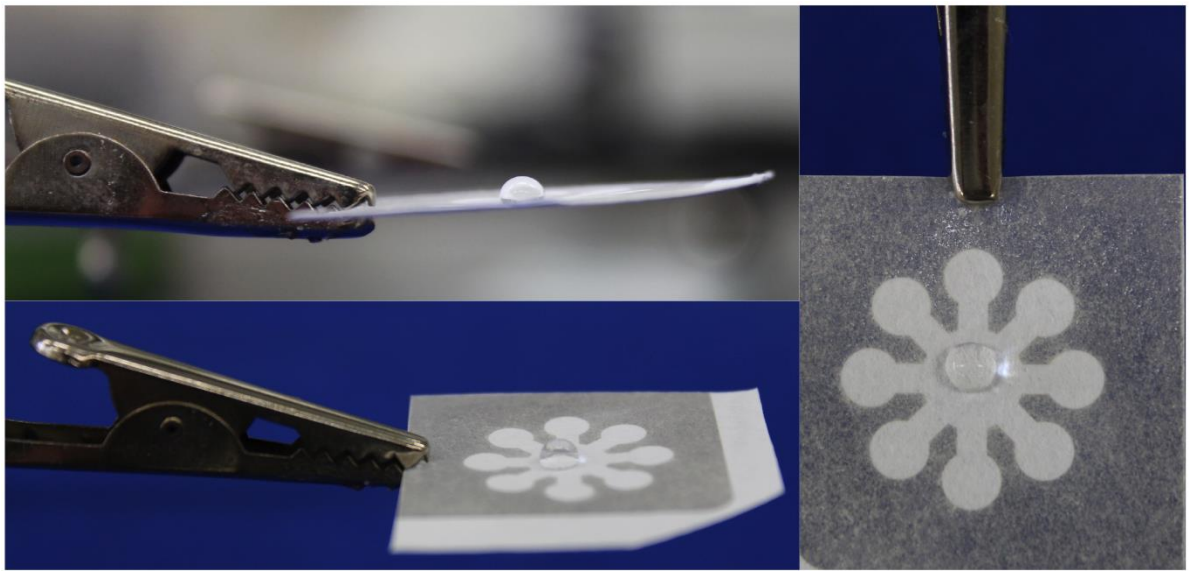

Figure 2.6 Photolithography (left) of the PAD fabricated by photolithography without oxygen plasma treatment. Ultrapure water was pipetted onto the PAD (right).

2.3.4 Comparison of performance for protein assay using the PADs

Finally, I compared the performance for the protein assay using the PADs. I carried out the colorimetric protein assay in triplicate, and compared the PADs using the K-scale (color scale) [29] and standard deviation (STD) of color scale. Figure 2.7a shows photographs of PADs used for the colorimetry. The protein reacted with TBPB to give detection zones with a blue color. Figure 2.7b presents the calibration plot of the protein assay using the PADs. The K -scale of the PAD fabricated by craft cutting was lower than the values of the other PADs. I consider that the evaporation rate of the craft cut PAD was higher than those of the other PADs, because the solution could evaporate not only from the top and back sides of the device, but

also from the edges. BSA molecules (66 kDa) cannot diffuse into all of the detection zones due to the rapid evaporation of the solvent. The diffusion or transfer rate of protein molecules depends on the drying condition of the paper substrate, and might be limited, even with the semi-dried condition due to rapid evaporation. In other words, all the BSA molecules introduced into the detection zones could not react with TBPB. For this reason, the color intensity obtained from the craft cut PAD was low. The K-scale of the PAD fabricated by photolithography also showed lower intensity compared with the two types of printing-based PADs. The introduced solution could not flow homogeneously into the PAD fabricated by photolithography, because of the leakage of solution from the introduction zone and the shortage of hydrophilic cellulose fibers inside the paper substrate by a plasma treatment of all the total topside area of the PAD. Therefore, BSA diffused non-uniformly and did not react with TBPB in the detection zones. On the other hand, the K-scale values of the PADs fabricated by wax printing and screen printing were of higher intensity than those of the other PADs. The hydrophilic area of printing-based PADs is composed of bare cellulose fibers, and the solution can only evaporate at the top and back sides of the paper substrates. I consider that the bare cellulose fibers and desirable diffusion rate of proteins were responsible for the high detection intensity. However, I did not confirm any large difference in the STD among the PADs, because of the similar color reproducibility in detection zones among the PADs. I fabricated three PADs for each fabrication method, and carried out the protein assay three times. This result indicates that the assay reproducibility of the PADs fabrication and of the protein assay was confirmed, regardless of the fabrication methods.

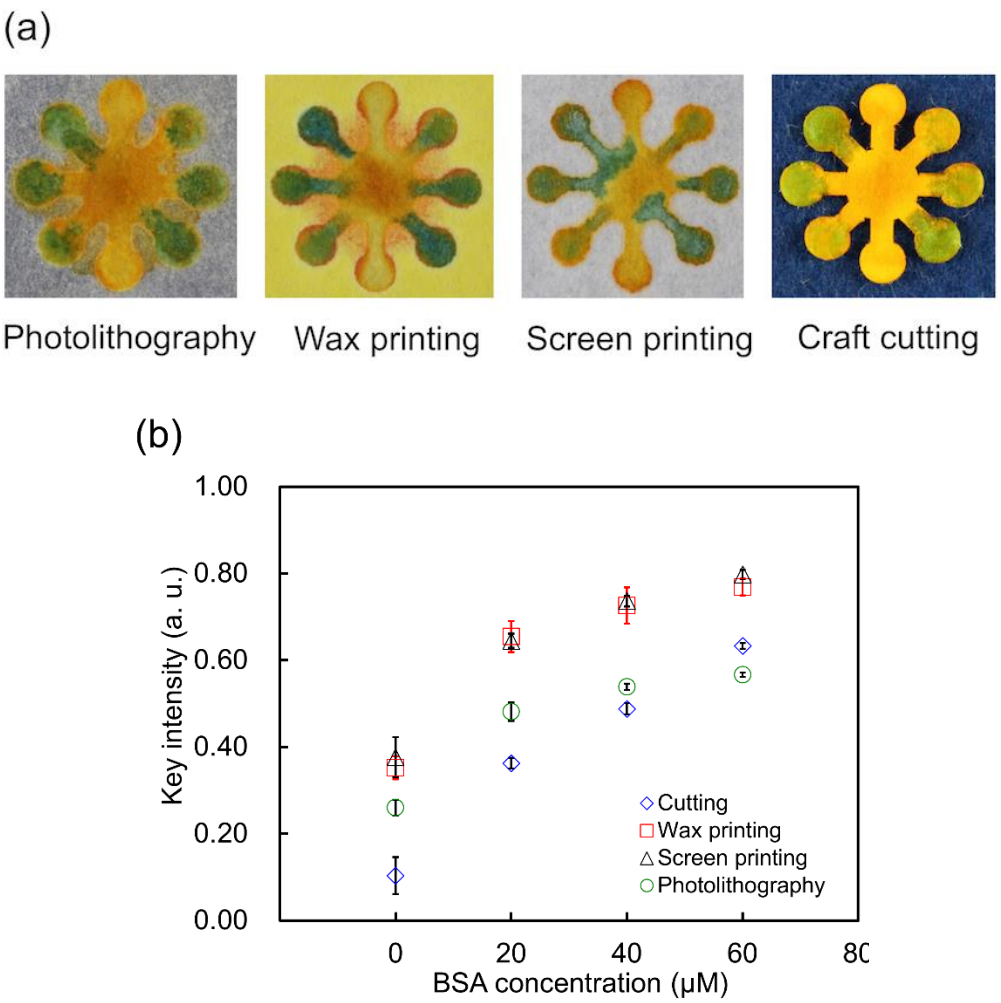

Fig. 2.7 Protein assay using the PADs fabricated by four methods: (a) Photographs of the PADs for colorimetric analysis. (b) The calibration plot of the protein assay using the four PADs.

2.4 Conclusions

I investigated the characteristics of PADs fabricated by four different methods: photolithography, wax printing, screen printing, and craft cutting. Photolithography has complicated fabrication procedures, and an oxygen plasma treatment is necessary to introduce an aqueous solution into the PAD. The boundary between the hydrophobic and hydrophilic areas was formed most sharply for the photolithography method among the four methods. However, the K-scale intensity of this device was lower than those of the other devices. Wax printing offers a simple and rapid fabrication, although the leakage of the solution should be prevented to

improve the wicking rate and to avoid cross-contamination. Screen printing is also an easy fabrication method. The screen-printed PAD had a good wicking property and showed high detection intensity. Craft cutting provides an automated fabrication for many PADs at once. The craft cut PAD had the fastest wicking rate among the four PADs due to the bare cellulose fibers. In conclusion, my reports established that different hydrophobic barrier conditions due to different four fabrication methods effected to the analytical properties, such as the wicking rate, the evaporation rate, and the measuring performance of colorimetry. I assume that the detection intensity can be raised by optimizing the evaporation rate. For these results, I concluded cutting and screen printing is suitable fabrication method for developing colorimetric PADs of blood test. Finally, I believe that these reported characteristics of the PADs will promote development of other new PADs and will lead to improved PAD performance.

2.5 Reference

[1] Y. Yang, E. Noviana, M. P. Nguyen, B. J. Geiss, D. S. Dandy, and C. S. Henry, *Anal. Chem.*, **89**, 71-79 (2017).

[2] L. S. A. Busa, S. Mohammadi, M. Maeki, A. Ishida, H. Tani, and M. Tokeshi, *Micromachines*, **7**, 86 (2016).

[3] D. Cheng, X. Zhang, X. Li, L. Hou, and C. Wang, *Anal. Sci.*, **33**, 185-189 (2017).

[4] N. A. Meredith, C. Quinn, D. M. Cate, T. H. Reilly, J. Volckens, and C. S. Henry, *Analyst*, **141**, 1847-1887 (2016).

[5] L. H. Mujawar, A. A. Felemban, and M. S. El-Shahawa, *Anal. Sci.*, **32**, 491-497 (2016).

[6] L. Syedmoradi, M. Daneshpour, M. Alvandipour, F. A. Gomez, H. Hajghassem, and K. Omidfar, *Biosens. Bioelectron.*, **86**, 353-368 (2016).

[7] F. Hori, Y. Harada, T. Kuretake, and S. Uno, *Anal. Sci.*, **32**, 355-359 (2016).

[8] J. Sittiwong, and F. Unob, *Anal. Sci.*, **32**, 639-643 (2016).

[9] K. Tominaga, S. Arimoto, K. Shimono, T. Yoshioka, F. Mizutani, and T. Yasukawa, *Anal. Sci.*, **33**, 531-

536 (2017).

[10] A. W. Martinez, S. T. Philips, M. J. Butte, and G. M. Whitesides, *Angew. Chem. Int. Ed.*, **46**, 1318-1320 (2007).

[11] A. W. Martinez, S. T. Phillips, G. M. Whitesides, and E. Carrilho, *Anal. Chem.*, **82**, 3-10 (2010).

[12] L. S. A. Busa, T. Komatsu, S. Mohammadi, M. Maeki, A. Ishida, H. Tani, and M. Tokeshi, *Anal. Sci.*, **32**, 815-818 (2016).

[13] E. Carrilho, A. W. Martinez, and G. M. Whitesides, *Anal. Chem.*, **81**, 7091-7095 (2009).

[14] K. Ogawa, and T. Kaneta, *Anal. Sci.*, **32**, 31-34 (2016).

[15] K. Abe, K. Suzuki, and D. Citterio, *Anal. Chem.*, **80**, 6928-6934 (2008).

[16] X. Li, J. Tian, and W. Shen, *Cellulose*, **17**, 649-659 (2010).

[17] J. L. Delaney, C. F. Hogan, J. Tain, and W. Shen, *Anal. Chem.*, **83**, 1300-1306 (2011).

[18] X. Yan, Y. Zheng, J. Gao, and J. Lee, *Anal. Sci.*, **33**, 1-3 (2017).

[19] S. Mohammadi, M. Maeki, R. M. Mohamadi, A. Ishida, H. Tani, and M. Tokeshi, *Analyst*, **140**, 6493-6499 (2015).

[20] W. Dungchai, O. Chailapakul, and C. S. Henry, *Anal. Chem.*, **81**, 5821-5826 (2009).

[21] Y. Sameenoi, P. N. Nongkai, S. Nouanthavong, C. S. Henry, and D. Nacapricha, *Analyst*, **139**, 6580-6588 (2014).

[22] J.-Y. Sun, C.-M. Cheng, and Y.-C. Liao, *Anal. Sci.*, **31**, 145-151 (2015).

[23] W. Liu, Y. Guo, M. Zhao, H. Li, and Z. Zhang, *Anal. Chem.*, **87**, 7951-7957 (2015).

[24] J. Yu, S. Wang, L. Ge, and S. Ge, *Biosens. Bioelectron.*, **26**, 3284-3289 (2011).

[25] P. K. Yuen, and V. N. Goral, *Lab. Chip*, **10**, 384-387 (2010).

[26] X. Li, D. R. Ballerini, and W. Shen, *Biomicrofluidics*, **6**, 011301 (2012).

[27] A. K. Yetisen, M. S. Akram, and C. R. Lowe, *Lab. Chip*, **13**, 2210-2251 (2013).

[28] L. S. A. Busa, M. Maeki, A. Ishida, H. Tani, and M. Tokeshi, *Sens. Actuators, B*, **236**, 433-441 (2016).

[29] T. Komatsu, S. Mohammadi, L. S. A. Busa, M. Maeki, A. Ishida, H. Tani, and M. Tokeshi, *Analyst*, **141**, 6507-6509 (2016).

CHAPTER 3 Consideration of Image Analysis Method for Multicolor Detection on Paper-Based Analytical Devices

3.1 Introduction

Since the first report of a PAD in 2007 by Whitesides's group as inexpensive analytical and diagnostic devices [1], PADs have steadily gained attention and interest among researchers [2–4]. The PADs have a great potential as analytical devices in resource-limited settings because they are inexpensive, easy-to-use and require no special measuring instruments. Several types of fabrication methods have been developed including photolithography [5, 6], screen printing [7], wax printing [8, 9], inkjet printing [10, 11] and cutting [12]. Several detection methods for the PADs also have been proposed such as colorimetric [1, 6], fluorescence [13], electrochemical [7], and electrochemiluminescence [14] methods. In these detection methods, colorimetric methods based on an image analysis of digital images of the device are used most widely because they offer easiness and simplicity of use. These methods require no special apparatus, only a digital camera or smartphone, and allow quantitative analysis by reading out the color information (RGB value or CMYK value) of the detection area of a PAD in the digital image. The color information is mainly obtained as separate RGB channel values or grayscale, which give the amount of analyte on the basis of the relationship between the color information and the analyte concentration. Several software applications for smartphones have been developed to perform image analysis of the PAD images [15, 16]. Therefore, a combination of μPADs and image analysis is a suitable technique for point of care testing and applications in resource-limited settings. The grayscale (the average of RGB values) is one of the most common measure in image-analysis based colorimetry [6, 17–19]. However, the grayscale possibly does not allow quantitative analysis based on multiple changes of color such as a universal pH test strip because the grayscale cannot follow multiple color changes.

Herein, I report a simple colorimetric pH measurement method using a PAD based on the CIE $L^*a^*b^*$ color system. The CIE $L^*a^*b^*$ color system has three coordinates L^*, a^*, and b^*. The L^* value indicates lightness, and $(a^* + b^*)^{1/2}$ and $\tan^{-1}(b^*/a^*)$ indicate chroma (C_{ab}) and hue angle (h_{ab}), respectively. The color difference (ΔE) between an objective color and a reference one is given by following equation [20–22]:

$$\Delta E = \sqrt{(a_x - a_0)^2 + (b_x - b_0)^2 + (L_x - L_0)^2} \quad (3.1)$$

where subscripts *x* and 0 denote objective and reference, respectively. Abe *et al.* [11] previously demonstrated the pH measurement using a universal pH indicator and the *a** coordinate. However, the reported method did not cover a wide pH range because of lack of color information. The *a** coordinate indicates redness and greenness for the positive (+*a**) and negative (-*a**) direction, respectively. The *a** value is given by $a^* = C_{ab} \times \cos(h_{ab})$. The colors (red and orange) appeared at low pH values corresponds to small hue angels. This resulted in the small change in the *a** coordinate. Thus, only the use of the *a** value is not suitable for pH measurement based on formation of multiple colors. Commonly, multiple-color changes have gained great attention in various assays, such as heavy metal assay [23] and enzymatic assay [24, 25], which could be applicable to PAD formats. Therefore, I examined if the quantitative measurement of pH can be performed by using Δ*E* for multiple color changes because Δ*E* contains much color information.

3.2 Experimental

3.2.1 Materials and Reagent

A universal pH indicator was prepared by mixing 0.11 mM thymol blue (pKa_1 = 1.7, pKa_2 = 8.9, pH range 1.2–9.6, Wako Pure Chemical Industries, Ltd., Osaka, Japan), 0.45 mM methyl red (p*K*a = 5.1, pH 4.2–6.2, Wako Pure Chemical Industries, Ltd.,), 0.96 mM bromothymol blue (p*K*a = 7.1, pH 6.0–7.6, Kanto Chemical Co., Inc., Tokyo, Japan), and 3.1 mM phenolphthalein (p*K*a = 9.3, pH 7.8–10.0, Kanto Chemical Co., Inc.) in 95% ethanol [1]. A 0.1 M phosphate buffer (Wako Pure Chemical Industries, Ltd.), 0.1 M acetic acid buffer (Kanto Chemical Co., Inc.), and 0.1M Tris-HCl buffer (Wako Pure Chemical Industries, Ltd.) were used for adjusting pH value in test solutions in a range of 2 to 9.

3.2.2 Fabrication of Paper-based Devices

A screen-printing table (WHT No. 3 and equipped with a vacuum pump that was manufactured by Mino Group Co., Ltd., Tokyo, Japan), a screen stencil (T-200 nylon mesh on an aluminum frame), and a squeegee were purchased from Unno Giken Co., Ltd. (Tokyo, Japan). The screen stencil was designed with 36 paper device patterns in it. The detailed fabrication procedures were described in the literature [2]. Polydimethylsiloxane (PDMS, SILPOT 184 Kit, Dow Corning Toray Co., Ltd., Tokyo, Japan) was used as a polymer ink for hydrophobic patterning. Paper substrate selected for the device was Whatman chromatography paper #1 purchased from GE Healthcare (200 × 200 mm, thickness: 0.18 mm, GE Healthcare Japan Co., Ltd., Tokyo).

I fabricated PADs by the previously reported screen-printing method [26]. The PAD had eight detection zones (diameter, 4 mm) and an introduction zone (diameter, 12 mm) as shown in Fig. 3.1. The detection zones were connected to the introduction zone via microchannels (width = 2 mm). In brief, a piece of chromatography paper was fixed onto a printing table. A patterned screen stencil was placed onto the chromatography paper and the paper was kept in place on the printing table via a vacuum pump. Then, PDMS was poured onto the screen stencil, and a squeegee was used to rub the PDMS into the pattern openings. The PDMS-printed paper was cured in an oven at 120 °C for 30 min. The patterned paper was removed from the oven and cut into separate paper devices (30 × 30 mm).

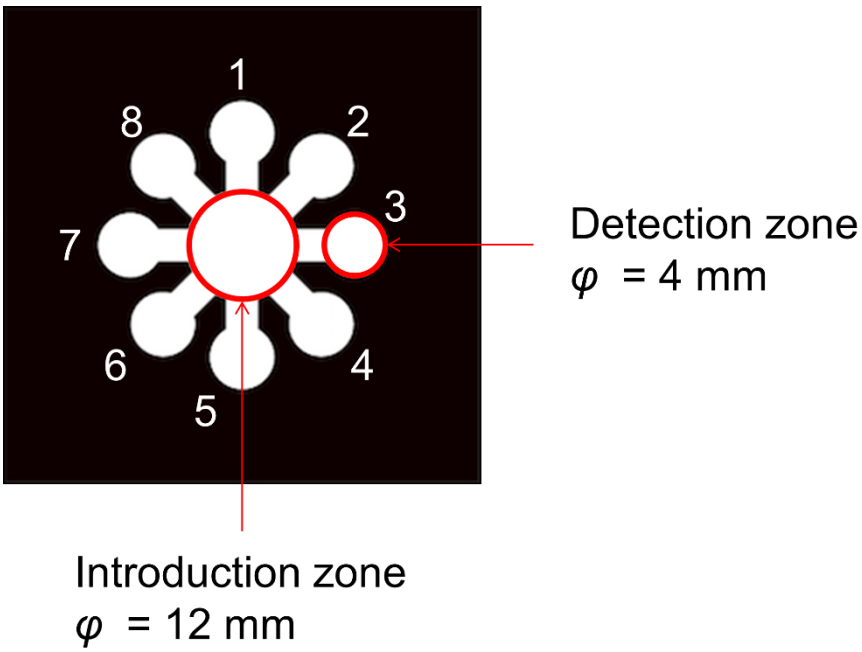

Figure 3.1 Illustration of the design of the PAD. The PAD had eight detection zones (φ = 4 mm) and an introduction zone (center part, φ = 12 mm).

3.2.3 Experimental procedure and image analysis

In the pH measurement with the PAD, 0.5-μL portions of aqueous solutions prepared at various pH values were introduced into the respective detection zones. After a 5-min incubation at room temperature, 15 μL of a universal pH indicator (the composition and the concentration are shown below and in the Supporting Information) was introduced into the introduction zone. After a 1-min incubation, a digital image of the PAD was taken with a digital camera (EOS Kiss X6i, Canon, Tokyo, Japan) under fluorescent lighting conditions. The distance between the PAD and the camera was fixed to ca. 20 cm. I used the ImageJ (ver. 1,48) software to obtain digital color information from digital images. A circular region of interest (ROI, 27000 pixels) was drawn around the detection zone in the digital image and was analyzed using the software, as shown in Fig. 3.2 (red broken line). For RGB values and grayscale, the "Measure RGB" plugin was used. The paper-based device had 8 detection zones with 4-mm diameter. I analyzed the 8 detection zones for a single paper-based device. For the image analysis in the CIE $L^*a^*b^*$ color space, the image was converted from RGB color space

to CIE *L*a*b** color space with the "Color Space Converter" plugin in the image analysis software and then separated into respective channels of *L**, *a**, and *b**. A circular region of interest (ROI, 27000 pixels) was selected around each detection zone and was analyzed using the software, as shown in Fig. 3.2 (a red dotted circle). In this study, I used the mean value on each measuring scale as the measuring value. I performed the assay in triplicate. Figure 3.3 shows a plot of grayscale at various pH values.

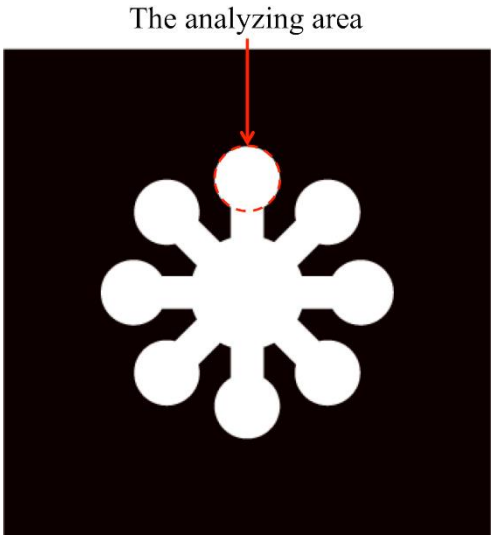

Figure 3.2 The analyzing area of paper-based device.

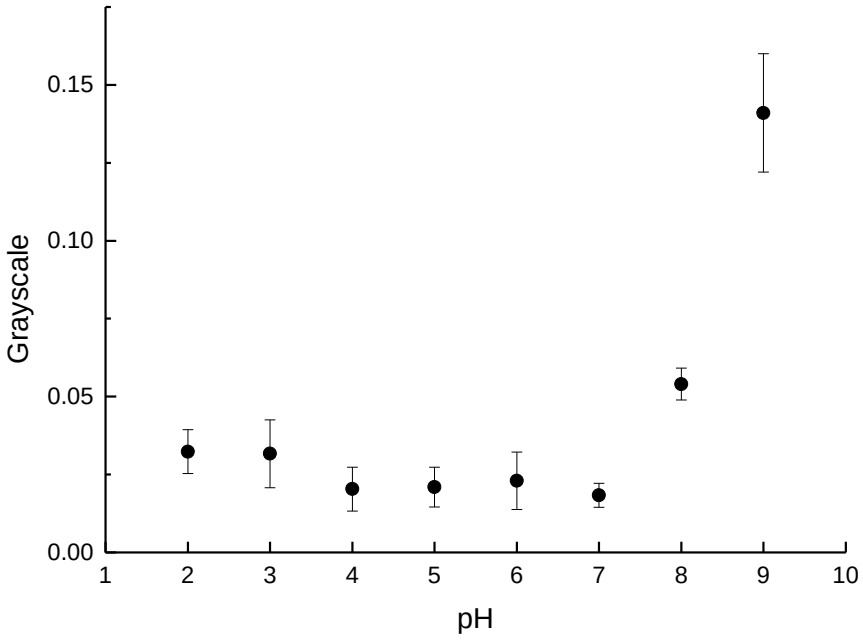

Figure 3.3 Plot of grayscale against pH value.

3.3 Results and discussion

3.3.1 Measurement of pH using RGB scale and CIE *L*a*b** color space

To perform the pH measurement in a wide range of pH values, I used the universal pH indicator consisting of thymol blue, methyl red, bromothymol blue, and phenolphthalein [9]. Figure 3.3 shows a photograph of the PAD, showing that the pH indicator exhibited various colors, such as red, orange, yellow and green in response to the pH values of test solutions (pH 2–9) at the detection zones.

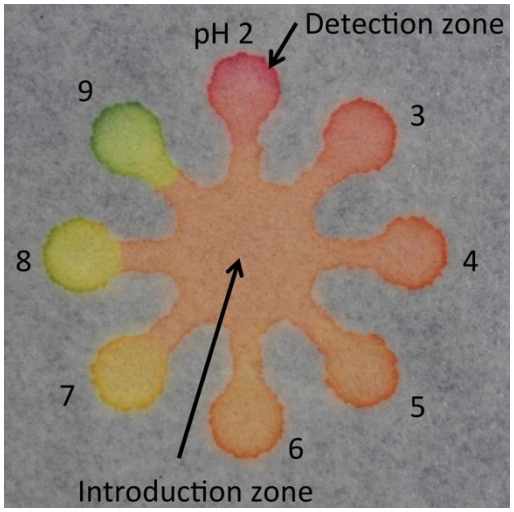

Figure 3.3 Photograph of the PAD producing multiple colors for various pH values (2–9). Aqueous solutions (0.5 μL) with different pH were introduced into separate detection zones and the universal pH indicator (15 μL) was added to the introduction zone.

First, I analyzed the color of the detection zones in the digital images in typical RGB color space and the CIE *L*a*b** color space. The obtained each value was given as a mean in the region. Thus, the nonuniformity in the colors in each zone was flattened. Consequently, the nonuniformity had little effect on the assay results. Figure 3.4a,b show a plot of obtained mean values by the grayscale and the RGB scale against various pH values, respectively.

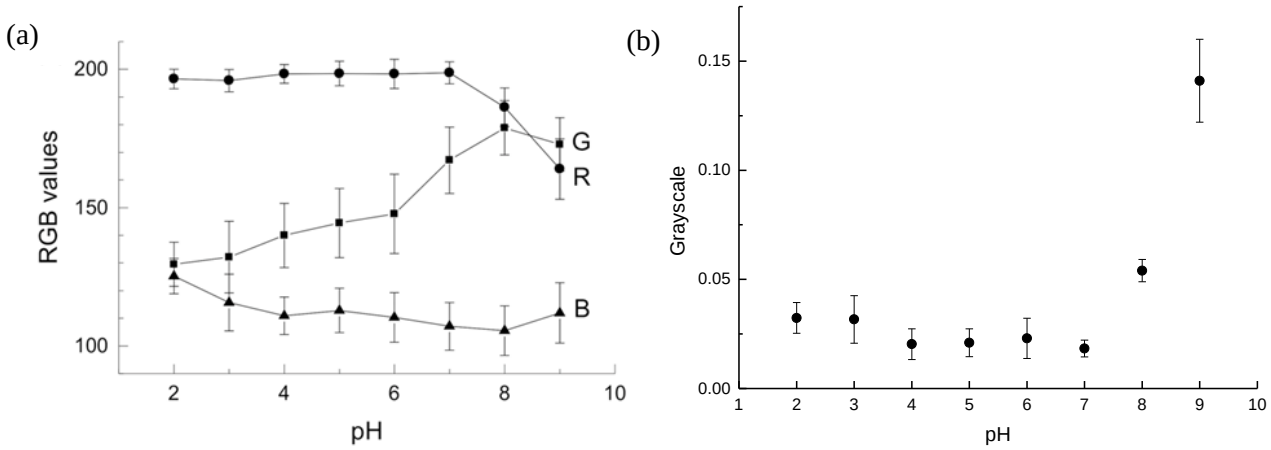

Figure 3.4 Plots of (a) grayscale and (b) plot of R, G, and B against pH value difference against pH value. Data points represent the mean of 3 measurements and error bars represent one standard deviation from the mean.

The RGB values and grayscale showed no monotonic change in response to the pH value of 2–9 and narrow detectable pH range with RGB values. This is due to lack of the color information because the respective RGB values show only the information of redness, greenness or blueness of the resulting colors. I also considered that large standard deviations were caused by the reproducibility of colors of photograph. Therefore, the RGB value is not suitable for pH measurement in the PAD giving multiple colors.

Next, I analyzed the color of the detection zones in the digital images in the CIE $L^*a^*b^*$ color space. The obtained each value was given as a mean in the region. Thus, the nonuniformity in the colors in each zone was flattened. The images were converted from the RGB color space to the CIE $L^*a^*b^*$ color space and split to L^*, a^*, and b^* channel with the Color Space Converter plugin prior to the image analysis. The detection zones in the split images were selected with circle and measured to obtain L^*, a^*, b^* values. Figure 3.5 shows 3D and 2D plots in CIE $L^*a^*b^*$ color space. Figure 3.5b shows a plot of a^* and b^* coordinates. Figures 3.5 a,b indicate that the data points formed a trace in an arc in response to an increase in pH value.

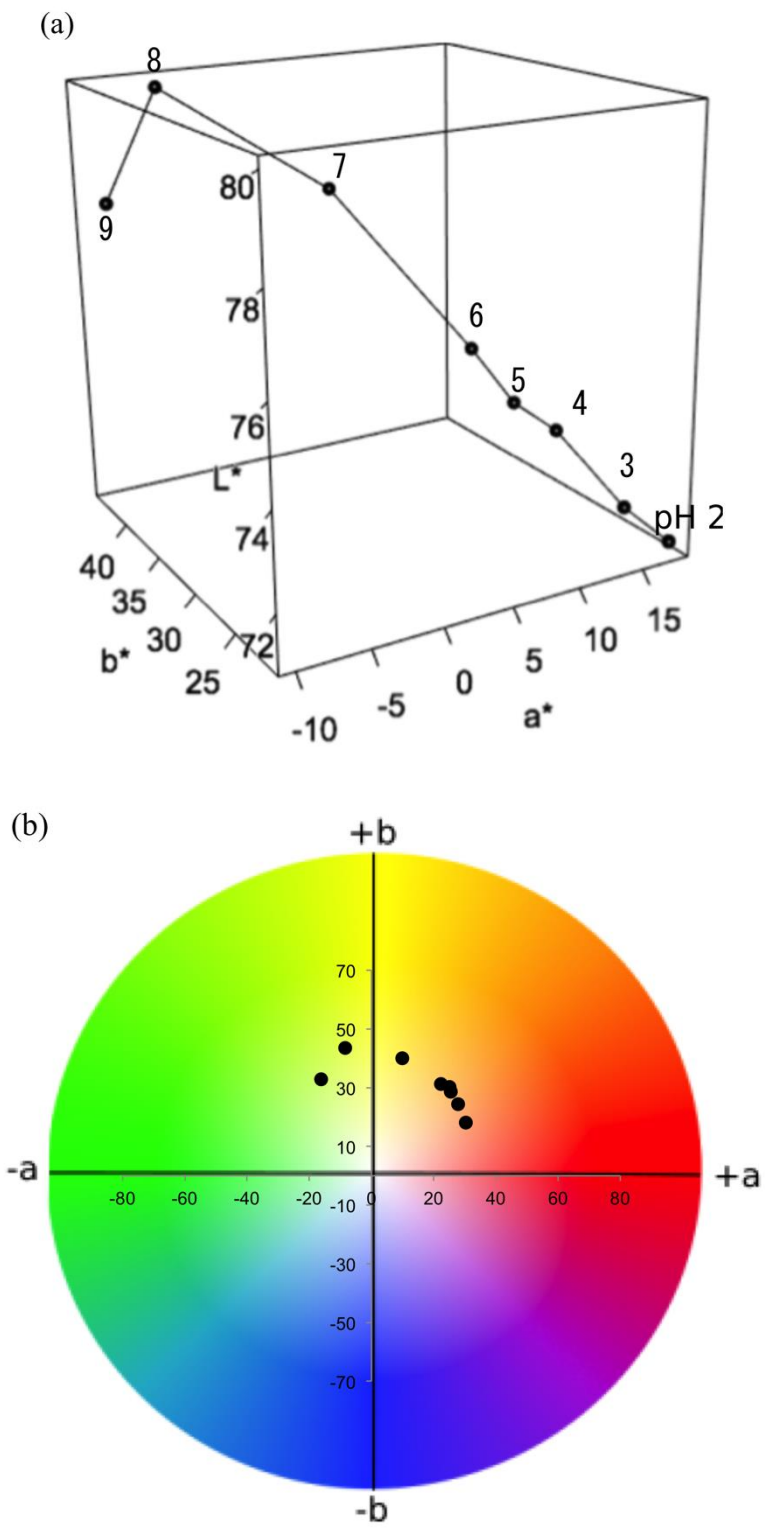

Figure 3.5 (a) 3D and (b) 2D plot of various pH values in CIE *L*a*b** color system.

Figure 3.6 also shows dependencies of pH value on each coordinate (L^*, a^*, and b^*). The a^* value was decreased with increasing pH value as shown in Fig. 3.6. However, the a^* value shows no significant change at low pHs because of large standard deviation as shown in Fig. 3.6, which suggests that the pH cannot be measured with the a* value. The b^* value and the L^* value did not show monotonic changes in response to the pH value of 2–9 (Fig. 3.6)

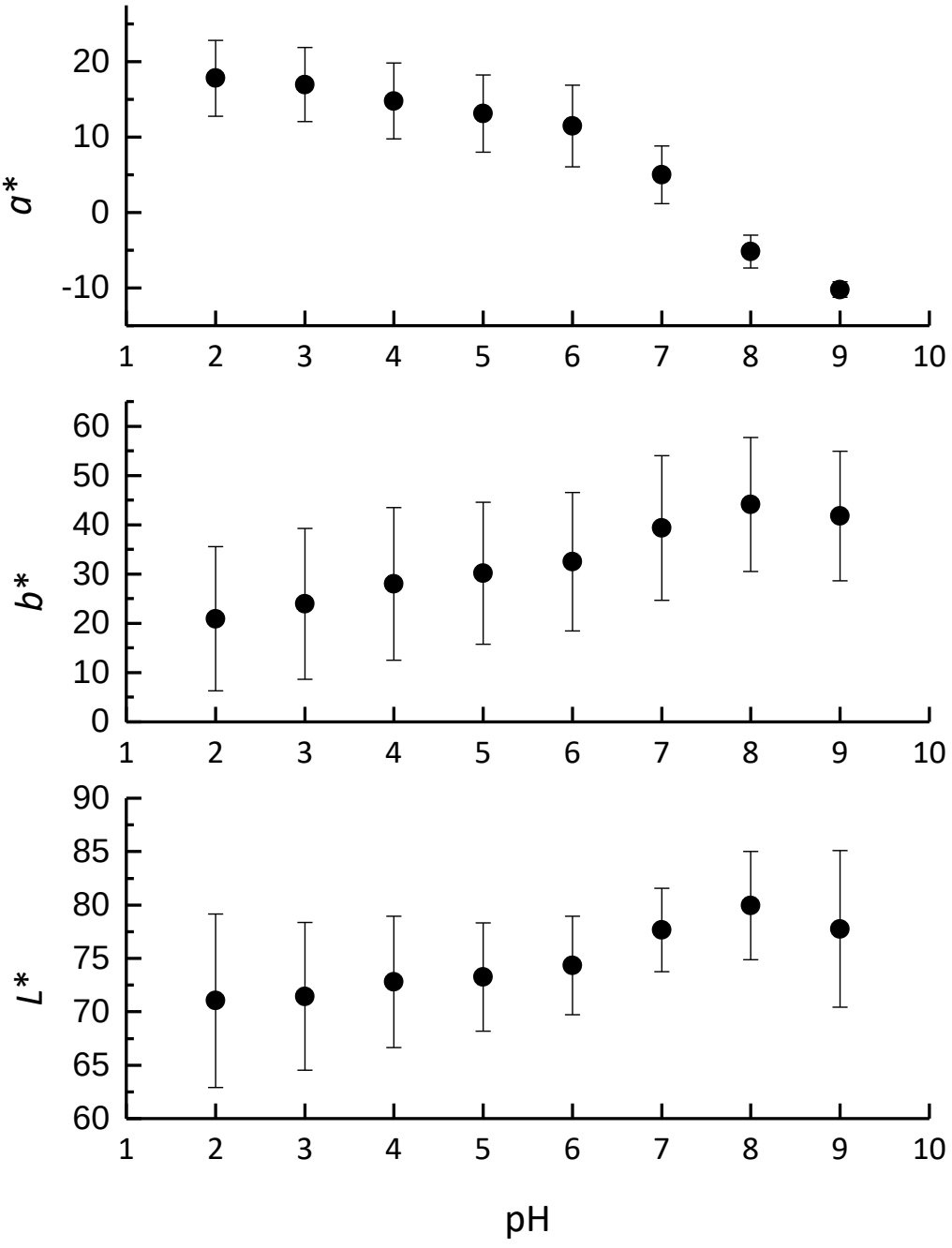

Figure 3.6 Plots of $L^*a^*b^*$ against pH value.

Subsequently, the color difference (ΔE) was calculated using Eq. (3.1) with the values of L_0*, a_0*, and b_0* for the color produced at pH 2. Figure 3.7a shows that the ΔE value increased monotonously with increasing pH value with small standard deviations. This confirmed high assay reproducibility. The detectable pH range was wider than those obtained with the RGB-based image analysis and single channel value of L*, a*, and b*. For comparison, $\tan^{-1}(b^*/a^*)$[15] vs. pH value plot was constructed (Fig. 3.7b) because $\tan^{-1}(b^*/a^*)$ contains the hue information as well as ΔE. The $\tan^{-1}(b^*/a^*)$ showed linear relationship with the pH value in the range of 2–9 ($r^2 = 0.972$). However, the $\tan^{-1}(b^*/a^*)$ values showed larger standard deviation than ΔE at low pHs.

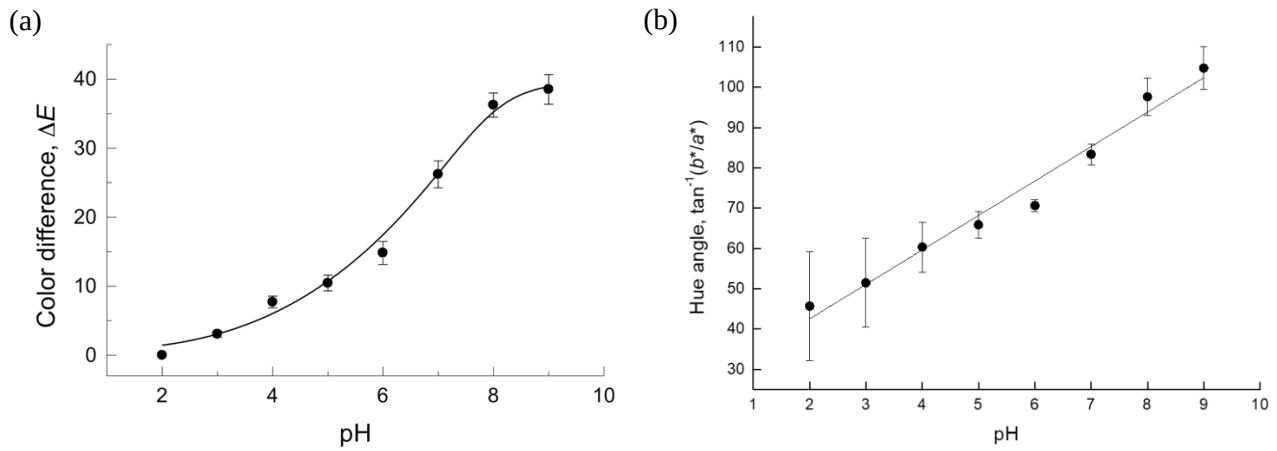

Figure 3.7 Plots of (a) CIE $L^*a^*b^*$ color difference against pH value and (b) plot of $\tan^{-1}(b^*/a^*)$ at pH values in CIE $L^*a^*b^*$ color system. Data points represent the mean of 3 measurements and error bars represent one standard deviation from the mean. In panel (a), data were fitted to a sigmoidal curve.

3.4. Conclusions

In conclusion, I demonstrated a simple pH measurement in the PAD by the colorimetric method based on the CIE $L^*a^*b^*$ color difference (ΔE). The use of ΔE was suitable for a colorimetric pH measurement based on the multiple color changes due to the universal pH indicator. For these results, I concluded the CIE $L^*a^*b^*$ color system can provide the multi-color detection. In the future, I expect that the combination of the PAD and image analysis based on CIE $L^*a^*b^*$ color system will enable quantitative analysis of multi-components in not only whole blood but also other liquid samples such as urea, milk [24] and river/sea water for multiple color changes.

3.5 Reference

[1] A. W. Martinez, S. T. Philips, M. J. Butte and G. M. Whitesides, *Angew. Chem., Int. Ed.*, **46**, 1318 -1320 (2007).

[2] D. M. Cate, J. A. Adkins, J. Mettakoonpitak and C. S. Henry, *Anal. Chem.*, **87**, 19-41 (2015).

[3] Y. Xia, J. Si and Z. Li, *Biosens. Bioelectron.*, **77**, 774-789 (2016).

[4] L. S. A. Busa, S. Mohammadi, M. Maeki, A. Ishida, H. Tani and M. Tokeshi, *Micromachines*, **7**, 86. (2016).

[5] A. W. Martinez, S. T. Phillips, G. M. Whitesides and E. Carrilho, *Anal. Chem.*, **82**, 3-10 (2010).

[6] A. W. Martinez, S. T. Phillips, E. Carrilho, S. W. Thomas III, H. Sindi and G. M. Whitesides, *Anal. Chem.*, **80**, 3699-3707 (2008).

[7] W. Dungchai, O. Chailapakul and C. S. Henry, *Anal. Chem.*, **81**, 5821-5826 (2009).

[8] E. Carrilho, A. W. Martinez and G. M. Whitesides, *Anal. Chem.*, **81**. 7091-7095 (2009).

[9] S. Karita and T. Kaneta, *Anal. Chem.*, **86**, 12108-12114 (2014).

[10] K. Yamada, T. G. Henares, K. Suzuki and D. Citterio, *Angew. Chem. Int. Ed.*, **54**, 5294-5310 (2015).

[11] K. Abe, K. Suzuki and D. Citterio, *Anal. Chem.*, **80**. 6928-6934 (2008).

[12] W. Liu, Y. Guo, M. Zhao, H. Li and Z. Zhang, *Anal. Chem.*, **87**, 7951-7957 (2015).

[13] N. K. Thom, G. G. Lewis, K. Yeung and C. T. Phillips, *RSC Adv.*, **4**, 1334-1340 (2014).

[14] N. Hao, M. Xiong, J. D. Zhang, J. J. Xu and H. Y. Chen, *Anal. Chem.*, **85**, 11715-11719 (2013).

[15] N. Lopez-Ruiz, V. F. Curto, M. M. Erenas, F. Benito-Lopez, D. Diamond, A. J. Palma and F. Capitan-Vallvey, *Anal. Chem.*, **86**, 9554-9562 (2014).

[16] C. Sicard, C. Glen, B. Aubie, D. Wallace, S. Jahanshahi-Anbuhi, K. Pennings, G. T. Daigger, R. Pelton, J. D. Brennan and C. D. M. Filipe, *Water Res.*, **70**, 360-369 (2015).

[17] S. J. Vella, P. Beattie, R. Cademartiri, A. Laromaine, A. W. Martinez, S. T. Phillips, K. A. Mirica and G. M. Whitesides, *Anal. Chem.*, **84**, 2883-2891 (2012).

[18] X. Mu, L. Zhang, S. Chang, W. Cui and Z. Zheng, *Anal. Chem.*, **86**, 5338-5344 (2014).

[19] L. Cai, Y. Wang, Y. Wu, C. Xu, M. Zhong, H. Lai and J. Huang, *Analyst*, **139**, 4593-4598 (2014).

[20] E. Hirayama, T. Sugiyama, H. Hisamoto and K. Suzuki, *Anal. Chem.*, **72**, 465-474 (2000).

[21] M. Maskan *J. Food Eng.*, **48**, 169-175 (2001).

[22] R. S. Berns, *Billmeyer and Saltzman's Principles of Color Technology*, John Wiley & Sons (2000).

[23] D. Li, X. Sun, M. Wang, H. Yu, H. Zhou, J. Wu and Y. Tian, *Sens. Actuators, B*, **220**, 1006-1016 (2015).

[24] A. Ishida, Y. Yamada and T. Kamidate, *Anal. Bioanal. Chem.*, **392**, 987-994 (2008).

[25] C. Li, Y. Yang, D. Wu, T. Li, Y. Yin and G. Li, *Chem. Sci.*, **7**, 3011-3016 (2016).

[26] S. Mohammadi, M. Maeki, R. M. Mohamadi, A. Ishida, H. Tani and M. Tokeshi, *Analyst*, **140**, 6493-6499 (2015).

CHAPTER 4 Development of Paper-Based Devices for Determining Blood Lithium Ion Concentrations

4.1 Introduction

Lithium carbonate is used for the treatment of bipolar disorder [1, 2]. The therapeutic concentration range of lithium ions is narrow (0.4 to 1.2 mM) in blood [3–8], and this is very close to the toxic range (>1.5 mM) [3–8]. Therefore, it is necessary to control the lithium concentration in blood to prevent severe side effects, such as tremors and vomiting. In addition, the suitable lithium concentration in blood is patient-dependent, and dosage must be determined based on psychological state, diet, and the presence of other ingested drugs [8, 9, 10]. In particular, health professionals must monitor the relationship between the lithium-ion concentration in the blood and the patient's condition to select the most appropriate dose [8, 11]. After treatment has started, the lithium-ion concentration in the blood must be measured in the early morning before the administration of lithium; this allows the evaluation of the trough value [8, 12]. After treatment stabilization, patients with bipolar disorder must undergo a regular assessment of their blood lithium-ion concentration at least once every 2–3 weeks or 3–6 months in the case of long-term treatment [8, 13].

In 1967, Bowman first reported [14] the measurement of the lithium-ion concentration in serum by atomic absorption spectrometry (AAS). However, this method requires the dilution of blood serum. To solve this challenge, flow injection, a non-diluting process, integrated with AAS was developed [15]. Moreover, a non-diluting measurement of the lithium ion concentration in serum by frame photometry was achieved by integration with the flow injection technique [16]. Electrochemical detection including ion selective electrodes [17–19] and capillary electrophoresis [20] was reported as another measurement technique in the 1980s. In the 2000s, since the first report of the colorimetric method for the determination of lithium-ion concentration in blood serum using chromoionophore 1 [21], several colorimetric [22, 23] and fluorometric [24–26] approaches have been developed. In particular, Glazer reported a colorimetric lithium assay with a duration of 2 min [23]. However, this method requires a large amount of blood (50 μL) and staff trained to handle low plasma volumes (0.2 μL). Additionally, other reported methods require not only the separation of interfering components including blood cells (BCs) and sodium and potassium ions but also pH adjustment. Therefore, these methods are restricted to the laboratory.

Recently, the research and development of “lab-on-a-chip” technologies have been carried out to develop point of care testing (POCT) devices for the determination of the lithium ion concentration in whole blood samples. In particular, capillary electrophoresis microchips [27–29] and paper based potentiometric cells [30], which integrate BC separation and serum dilution, have been developed. These approaches achieve direct measurement by integrating pretreatment procedures, but they have several disadvantages, for example, complicated channel design and fabrication procedures and high voltage manipulation using expensive instruments. Therefore, a simple and low-cost method integrated with blood cell separation for the POCT of the lithium-ion concentration is urgently required.

Microfluidic paper-based analytical devices (μPADs) have been used for POCT in a broad range of analytical field such as clinical diagnosis [31–34] and tests for toxins in food and water [35–38] because a paper substrate provides several advantages as an analytical tool.

(1) Cellulose-based paper is readily available and inexpensive.

(2) The fibric cellulose structure of paper has the ability to wick liquid fluids by capillary force without an external power source.

(3) Patterning to form hydrophilic zones using typical cutting methods or common printing methods is possible.

(4) Paper has good portability, disposability, and biological compatibility.

(5) Various detection methods can be selected according to their needs. In particular, the colorimetric method based on image analysis with a smartphone is a simple and user-friendly method.

This paper describes a paper-based device for blood cell separation and the colorimetric determination of the lithium ion concentration in whole blood with a small sample volume at low cost. The key feature of

this device is that the assay is completed in a single step. As described in General Introduction, the drawbacks of PADs toward blood tests are two points: needing (i) the plasma separation and (ii) an accurate volume manipulation of the separated plasma. To overcome these drawbacks, I designed the device configuration as shown in Figure 4.1. After whole blood is placed on the injection port, it is transferred into the separation unit under the action of capillary forces. Blood cells are filtered in the first half of the separation unit by small pores of glass fibers. In contrast, plasma reaches the detection unit to produce a colored product visible through the detection window. This device is simple and user friendly. Because the detection unit is placed at the end of the separation unit, the sample flows perpendicularly from the end of the separation unit to the detection unit. Compared to lateral flow, perpendicular flow provides uniform color formation in the detection window built into the detection unit and prevents the migration of the free reagent to the edge of the detection window. The detection window contains a concentrated detection reagent (F28 tetraphenylporphyrin, F28TPP), which yields a strong magenta color in the presence of lithium ions. The developed μPAD exhibits high sensitivity, precision, and reproducibility comparable with conventional measurement instruments with standard samples. In addition, although an increase in the coefficient of variation was necessitated for utilization in POCT, the test results of the spiked blood samples showed good linearity. The required sample volume was 10 μL, and the assay time was approximately 10 s. Thus, the lithium ion concentration of blood can be measured by non-specialists anywhere using only the device and a smartphone. Consequently, the present device will provide an alternative method for the monitoring of the blood lithium ion concentration in the treatment of bipolar disorder.

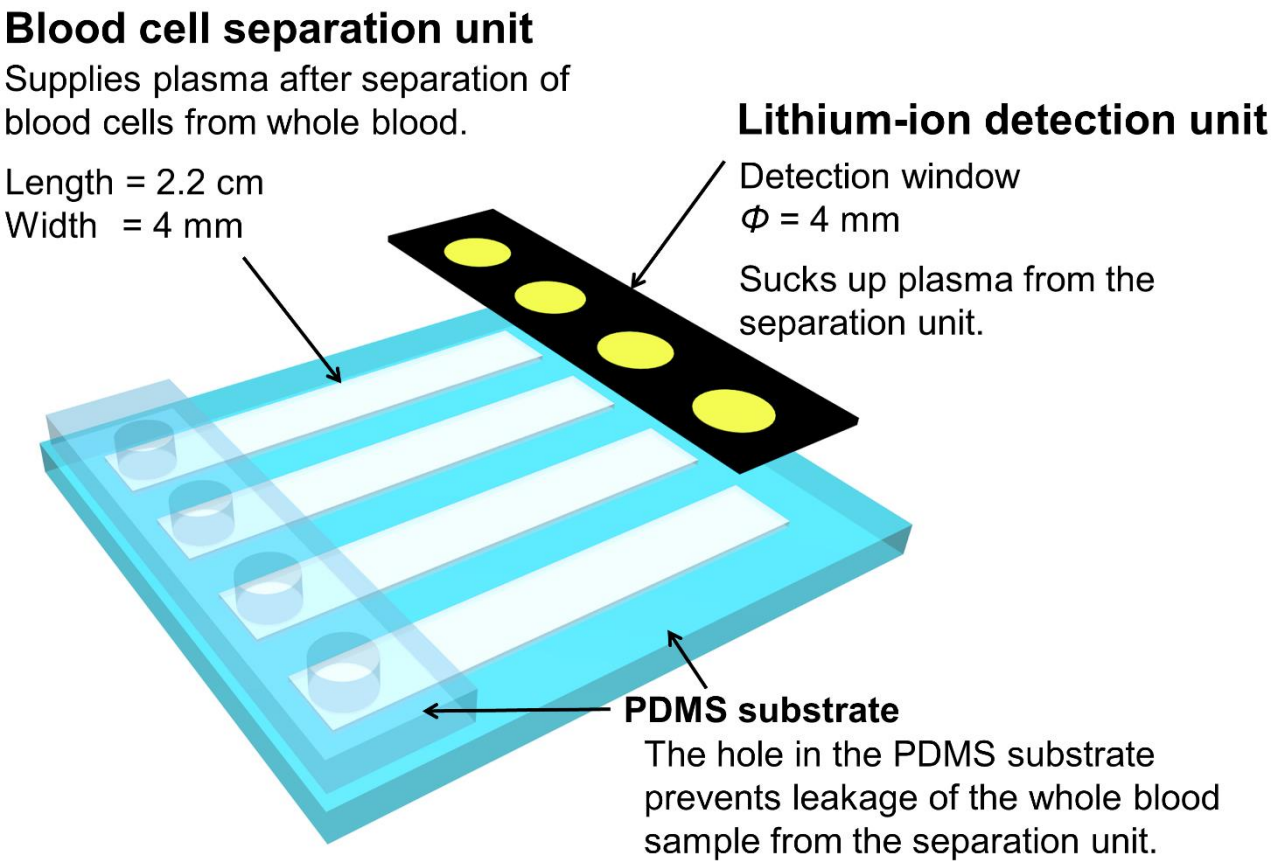

Figure 4.1 Device design for the determination of the lithium ion concentration in blood. The paper-based device consists of a blood cell separation unit, a lithium-ion detection unit, and a polymer substrate.

4.2 Experimental

4.2.1 Reagents and chemicals

High-purity cotton blotting paper #319 was purchased from Ahlstrom-Munksjö Co., Ltd. (20 × 20 cm, thickness: 0.48 mm, Helsinki, Finland) and used as a substrate for the lithium ion detection unit. An MF1, blood cell separation membrane, was purchased from GE Healthcare Japan Co., Ltd. (22 mm × 50 m, thickness: 0.367 mm, Tokyo, Japan) for the blood separation unit. These surface images of paper materials treated with gold vapor deposition for 1 min were observed by a benchtop scanning electron microscope (SEM; JCM-6000Plus Versatile Benchtop SEM, JEOL Ltd., Tokyo, Japan.) as shown in Fig. 4.2. For use as a hydrophobic screen-printing ink and polymer substrate, polydimethylsiloxane (PDMS, SILPOT 184 CAT) was purchased

from Dow Corning Toray Co., Ltd., (Tokyo, Japan). Multi walled carbon nanotubes (Sigma–Aldrich Co., Inc., St. Louis, MO, USA) were mixed with the hydrophobic ink to prevent the reflection of fluorescent light. For the measurement of the lithium ion concentration, I used a lithium ion standard solution (2 mM) and F28 tetraphenylporphyrin (F28TPP) as the detection reagent. These were contained in a commercially available colorimetric assay kit, (ESPA Li II, NIPRO Co., Inc., Osaka, Japan) and the details of the detection principle as shown in Fig. 4.3. To prepare a spiked blood sample, I obtained a 10 mM lithium ion standard solution from NIPRO Co., Inc. (Osaka, Japan). Spiked blood samples ($[Li^+]$ = 0–2 mM) were prepared using human whole blood with added sodium citrate (Tennessee Blood Services Co., Ltd., Memphis, TN, USA). All the samples were prepared using a phosphate buffered saline (PBS, pH 7.5, Thermo Fisher Scientific Inc., Tokyo, Japan).

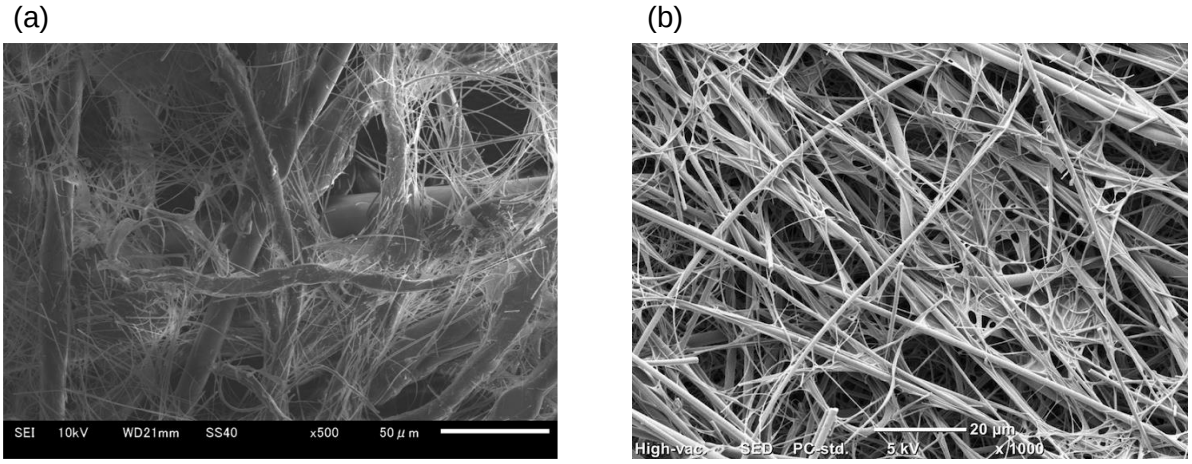

Figure 4.2 The surface of a raw substrate for a paper-based device, observed using a benchtop SEM. (a) SEM image of chromatography blotting paper used as a detection unit for lithium ions. (b) SEM image of a blood cell separator used as a separation unit for blood cells.

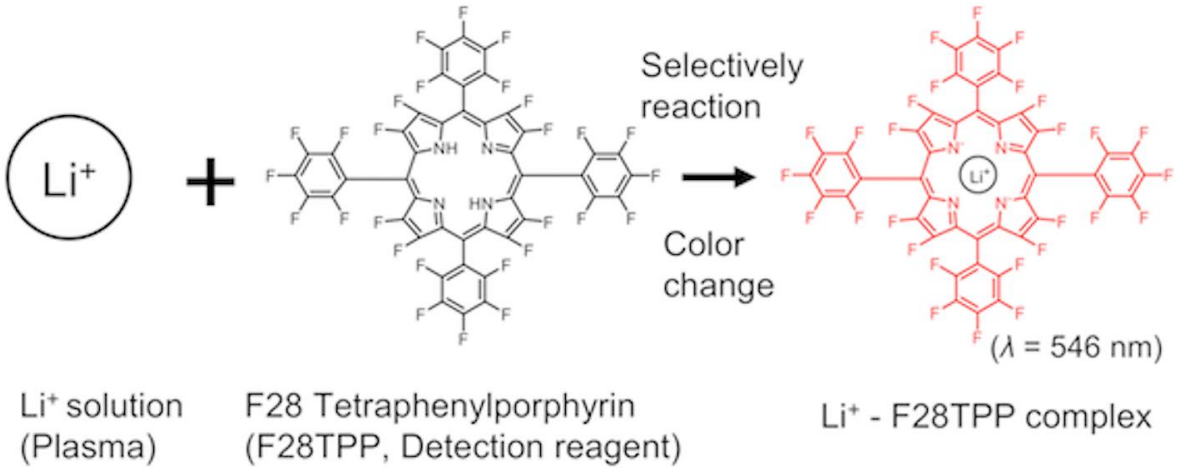

Figure 4.3 Principle of lithium ion detection using a commercial colorimetric assay kit. F28 tetraphenylporphyrin (F28TPP), a detection reagent, selectively reacts with Li^+ to produce a red Li^+-F28TPP complex (λ = 546 nm).

4.2.2 Device fabrication

I used a paper-based device design as shown in Fig. 4.1 to prevent non-uniform coloring and sample leakage. The device is composed of the lithium ion detection unit, four BC separation units, and the PDMS substrate. A hole in the PDMS substrate allows the smooth wicking of blood to the separation unit. Without this substrate, some of the blood would flow on the surface of the separation unit without penetrating it. Additionally, the device designed that can detect four analytes by combining with my evaluated image analysis method in the future. However, this thesis demonstrated that the determination of single target analyte (Li^+) on the device. Crucially, using this setup, the device allows the immediate determination of the lithium ion concentration on sample injection.

The lithium-ion detection unit was designed using Inkscape (v. 0.92.1) and had four detection windows (ϕ = 3, 4, 5, and 6 mm) as shown in Fig. 4.4a. A patterned screen stencil (T 200 nylon mesh on an aluminum frame) fabricated by photolithography and a squeegee were purchased from Unno Giken Co., Ltd. (Tokyo, Japan). For the patterning, I used a desktop hand screen-printing table (WHT No. 3 equipped with a vacuum

pump) that was purchased from Mino Group Co., Ltd. (Tokyo, Japan). To fabricate the lithium ion detection unit the patterning on a paper substrate was carried out by rubbing PDMS on the screen mesh with a squeegee (Figure 4.4b). The detailed screen-printing fabrication procedures have been described in my previous papers [39-41].

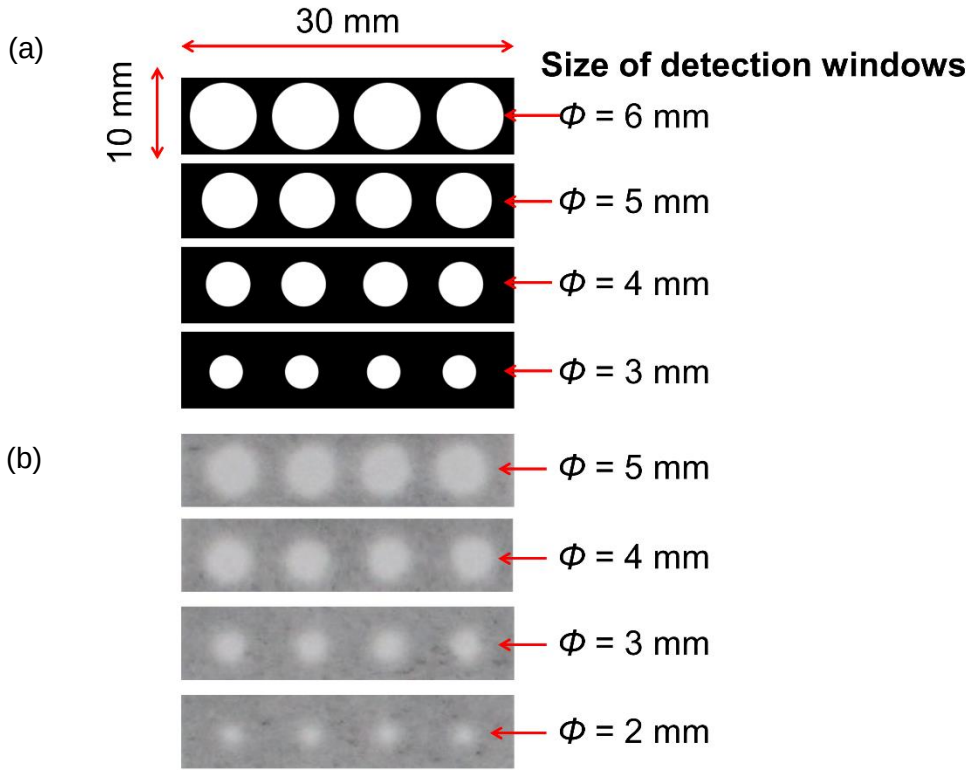

Figure 4.4 (a) Design of a detection unit for lithium ion with different windows of diameters 3, 4, 5, and 6 mm. (b) Photographs of the detection units fabricated by screen-printing. After fabrication, the window size was ~1 mm smaller than that of a screen stencil.

4.2.3 Device operation and measurement

The working principle and the experimental process using the device and micropipette are shown in Figures 4.5 (a) and (b). Aliquots (20 μL) of the detection reagent were loaded onto the respective detection windows and dried in the dark at room temperature for one day. The BC separation unit was cut to a predetermined size with scissors and placed on the PDMS substrate. After component positioning, four 20-μL

droplets of the sample solution were injected into the holes of the polymer substrate and were transferred into the separation unit by capillary force. After the sample solution reached the end of the separation unit, the detection unit was placed in contact with the end of separation units for 5 s. Finally, a photograph of the detection unit was taken with a digital camera (EOS Kiss X6i, Canon, Tokyo, Japan, distance: ca. 15 cm, ISO: 1600, shutter speed: 1/200, aperture value: 5.6) under a fluorescent light. The obtained image was converted to the CMYK color scheme as described elsewhere, and the intensity of the magenta color (denoted magenta intensity here) visible in each detection window (region of interest (ROI): 7860 pixel) was obtained by image analysis using ImageJ ver. 1.48 (Figure 4.5 c) [42]. I have used the maximum value obtained by image analyses of all the samples.

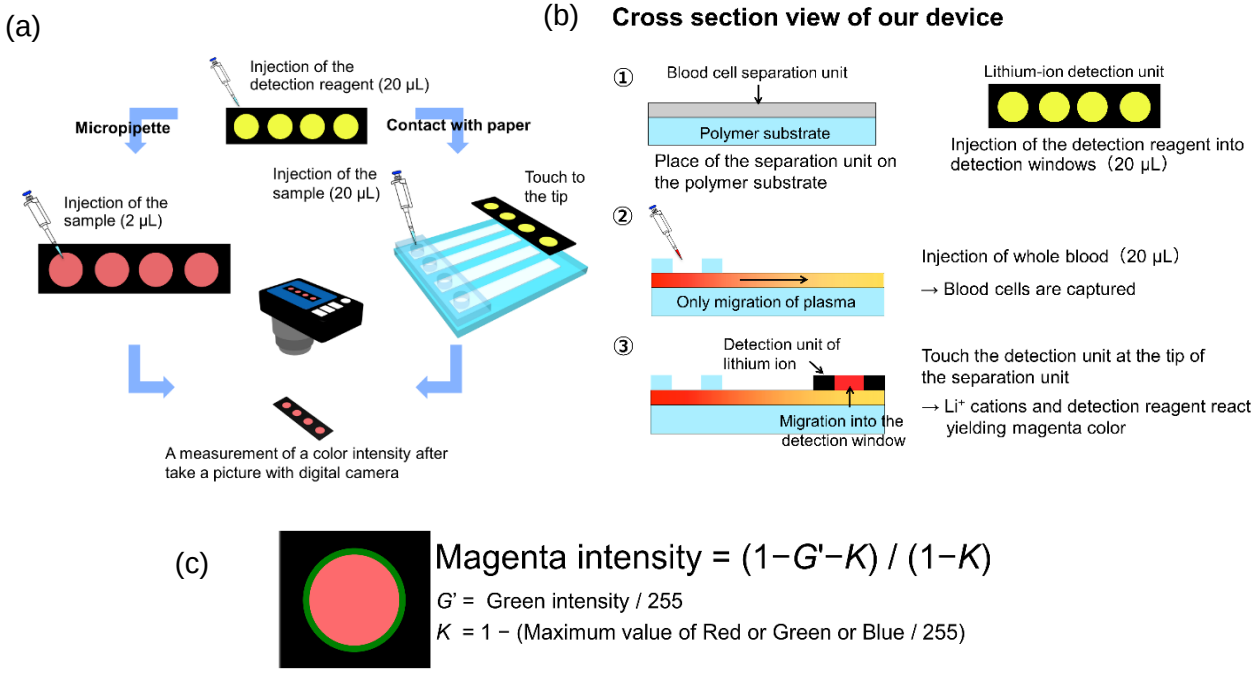

Figure 4.5 (a) Experimental procedure by micropipette/contact operation. (b) Principle for the determination of lithium ion concentration in blood using my device. The two processes (separation and detection/visualization) occur within approximately 10 s. (c) Region of interest (ROI, indicated by the green circle) for image analysis using the ImageJ ver. 1.48 software. The image was converted in the CMYK color space. The color intensity was obtained in magenta scale in each window area (red color) as a green circle.

4.3 Results and discussion

4.3.1 Optimization of device parameters

I fabricated lithium ion detection units using a stencil (detection window diameters of 3, 4, 5, and 6 mm) by screen printing (Figure 4.4a). The fabricated detection window was approximately 1 mm smaller than the screen stencil design because of the non-uniform penetration of uncured PDMS in the cellulose fibers (Figure 4.4b). The detection windows having diameters of 2 and 3 mm did not clearly form a circular shape because of the high viscosity of PDMS and the thick paper substrate provided by fine fibers. Therefore, the 2 mm detection window was not used in this study. For further study, I used detection windows with diameters of 3, 4, and 5 mm.

First, I optimized the strip size of the separation unit, that is, the width and length, using the separation membrane for red blood cells (RBCs). In these tests, I used 20-μL blood samples based on the typical volume used in existing commercial techniques. The width of the blood separation membrane was 4 mm in accordance with the diameter of the detection window. Different lengths of blood separation membrane were tested, from 1 to 3 cm. At 2 cm or less, a narrow region of plasma that was close to the non-separated region was formed. In contrast, the plasma did not reach the end of the separation membrane at 2.5 cm or greater. Figure 4.6 (left) shows the separation units (length: 2.2 cm and width: ca. 4 mm) wicking blood samples (20 μL). The separation of BCs was accomplished within a length of approximately 1 cm, and a plasma region sufficient for contact with the detection unit was obtained. Details of the optimization with a low volume of whole blood (10 and 15 μL) is shown in Fig. 4.6 (middle and right). The optimized size of each sample volume was used in all experiments.

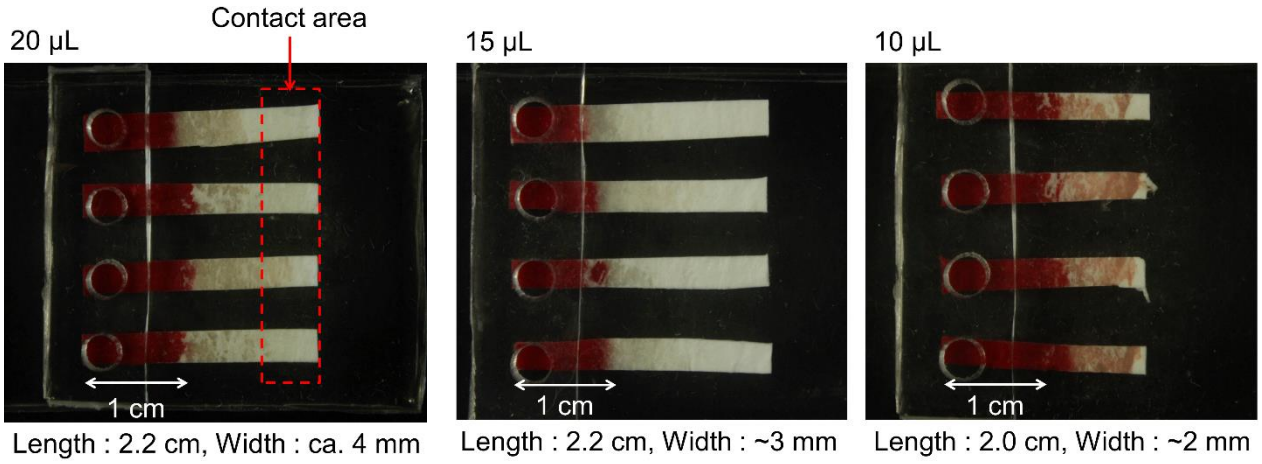

Figure 4.6 Optimization of the separation unit size with different loading volume of human whole blood. Separation ability of the RBC separation units. Photographs of separation units after an injection of spiked blood samples of volume 20 µL (left), 15 µL (middle) and 10 µL (right), respectively. The right-hand-side photograph shows little hemolysis of blood. The separation units were completely separated at a distance of ~1 cm, and there is a large plasma region.

To obtain sufficient sensitivity for clinical applications, I optimized the loading volume of the detection reagent (0.168 mg/mL) in the detection window with a diameter of 4 mm. Various loading volumes of the detection reagent from 5 to 30 µL were loaded in the 4-mm diameter detection window by pipetting and dried in the dark at room temperature. A 2-mM Li^+ solution of 2-µL volume was added to the detection unit and dried with different volumes of the detection reagent. As shown in Fig. 4.7, the magenta intensity was linear up to 20 µL, and the slope became gentler when the volume exceeded 20 µL. Thus, the excess load of the detection reagent caused a signal increase in the blank sample. Therefore, a loading volume of 20 µL of detection reagent was chosen.

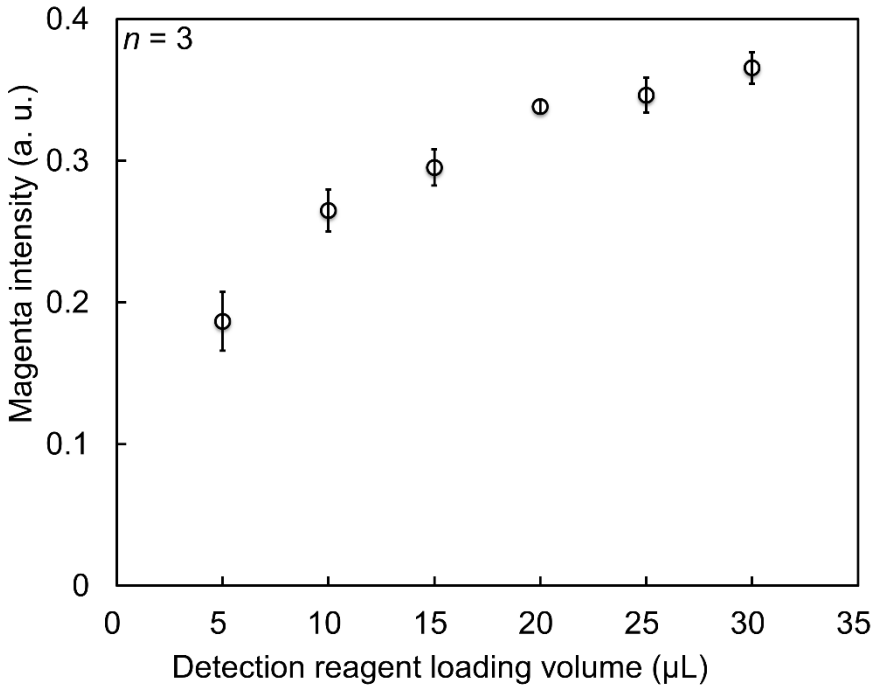

Figure 4.7 Optimization of the injection volume of the detection reagent in the detection window. The plots showed the relationship between the magenta intensity and the volume of the injected detection reagent. The magenta intensity was almost same for injection volumes of 20 μL or more. Moreover, use of a large amount of detection reagent induced increase in background signal.

Subsequently, I optimized the detection window size using the optimized loading volume of detection reagent. I expect that the use of different volumes influences the magenta intensity because of the difference in the amount of detection reagent per unit volume. Figure 4.8a shows the calibration plots obtained with different window sizes. As expected, the calibration plot with a 3 mm detection window was higher than the others, especially in the high concentration range. However, large error bars were obtained for two reasons: the 3 mm detection window was difficult to fabricate in the correct size and with a clear shape, and different drying conditions occurred because of the non-uniform window size. In the case of 4 and 5 mm detection windows, no significant differences in the color intensity were obtained. Thus, I chose the 4 mm detection window for further experiments. Finally, for a proof of concept demonstration, I compared the color uniformity obtained after device and pipette operation. Two microliters of a 2 mM Li^+ solution was loaded on each detection

window by pipette. Figure 4.8b shows the calibration plots obtained after pipetting the sample solution using same experimental conditions as my method. For all tested window sizes, the magenta intensity increased with increase in lithium ion concentration in the low concentration range (0 to 0.8 mM), but the intensity was almost constant in the high concentration range (see Figure 4.8a), possibly because the reagent was carried away from the center to the edge of the detection window by capillary force after pipetting. In contrast, contact loading resulted in uniform coloring because the sample was absorbed over the whole surface of the detection window.

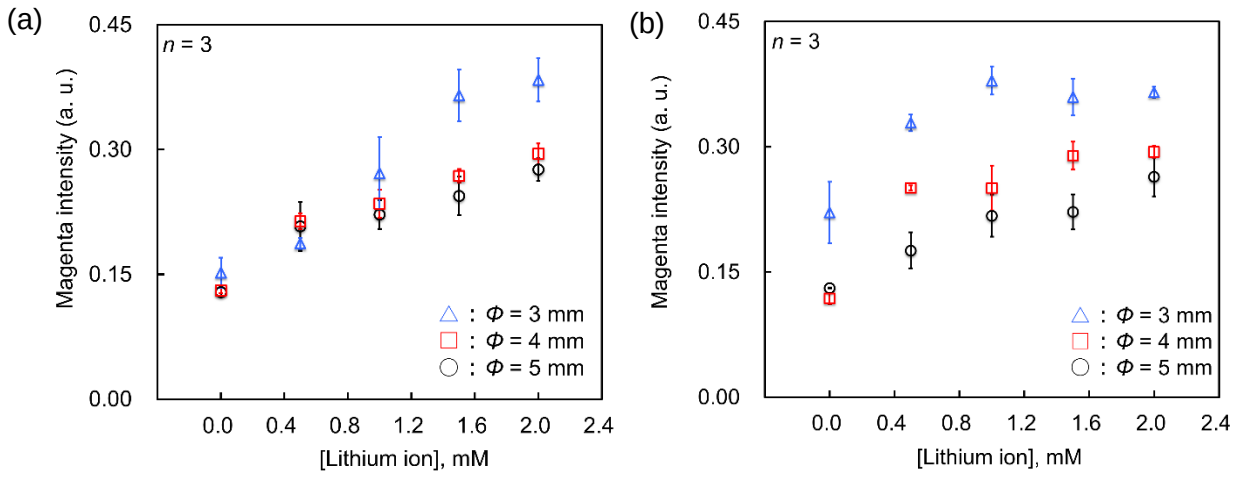

Figure 4.8 Optimization of the detection window size. The plots show the relationship between magenta intensity and the detection window size on (a) paper-to-paper contact loading and (b) micropipette loading. The magenta intensity increased with decrease in window size in both the cases. However, linearity over the entire measured range was only obtained for contact loading.

4.3.2 Investigation of parameters related to paper-to-paper contact: introduction volume, applied pressure, and contact time

To determine the absorption volume for quantitative analysis, I compared the magenta intensity obtained using a 2 mM Li^+ solution loaded by contact to that loaded with a pipette. The magenta intensity

obtained by contact loading was similar to that obtained by loading with 1.5 μL via pipette, as shown in Fig. 4.9.

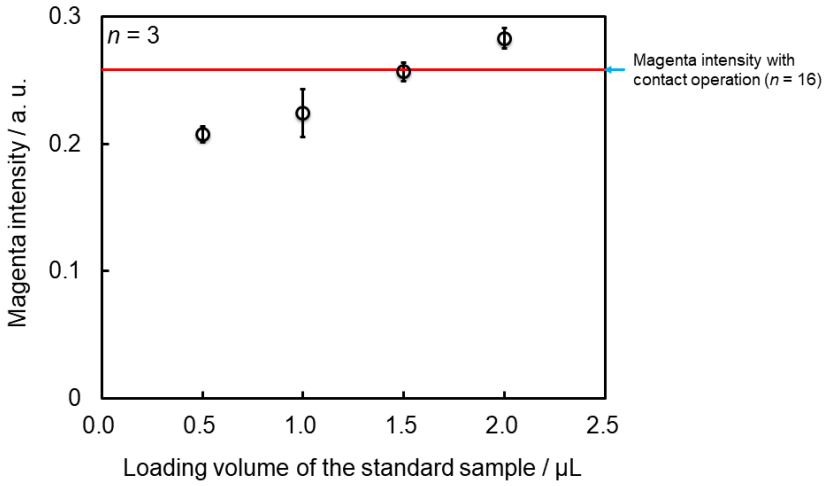

Figure 4.9 Effect of sample volume directly put on the detection unit with a pipette on color intensity. The red line indicates the magenta intensity obtained when the sample solution was introduced from the separation unit to the detection unit in the device studied herein. This indicates that the introduced volume is estimated to be 1.5 μL

Subsequently, I investigated the effects of the contact pressure and time because these should influence the sample penetration volume and the color intensity. To determine the contact pressure, I measured the weight required to completely fill the detection zone with plasma by pressing with a finger. The contact pressure calculated as $P = ((W) \times g)/A$, where P is the applied pressure, W is the measured weight, g is the acceleration by gravity (9.80665 m/s^2), and A is the area of the detection window ($4\pi \times 10^{-6}$ m^2).

The contact time required to completely fill the detection window with the sample was measured. The sample solution completely filled the whole detection window immediately (see Figure 4.10a) when the applied pressure was approximately 46.8 kPa. Next, I investigated the effect of the time that the separation and detection units were in contact with at 0.5, 1.0, and 2 mM Li^+ in spiked blood samples. Contact times

from 1 to 10 s were measured. The experimental procedure was the same as that described above. Figure 4.10a shows photographs of the detection unit after contact with the 2 mM Li^+ spiked blood samples. An increase in the magenta intensity of the detection windows depending on the lithium-ion concentration could be seen by the naked eye. Figure 4.10b-d show the relationship between the contact time and the magenta intensity using the 0.5, 1.0, and 2 mM Li^+ in spiked blood samples. In all results, the magenta intensity remained constant throughout because the wettability area of the detection unit was completely filled with rapid absorption after contact with BC units. After optimization of the whole blood injection volume and device design, my method was found to allow the rapid determination of the lithium-ion concentration in blood.

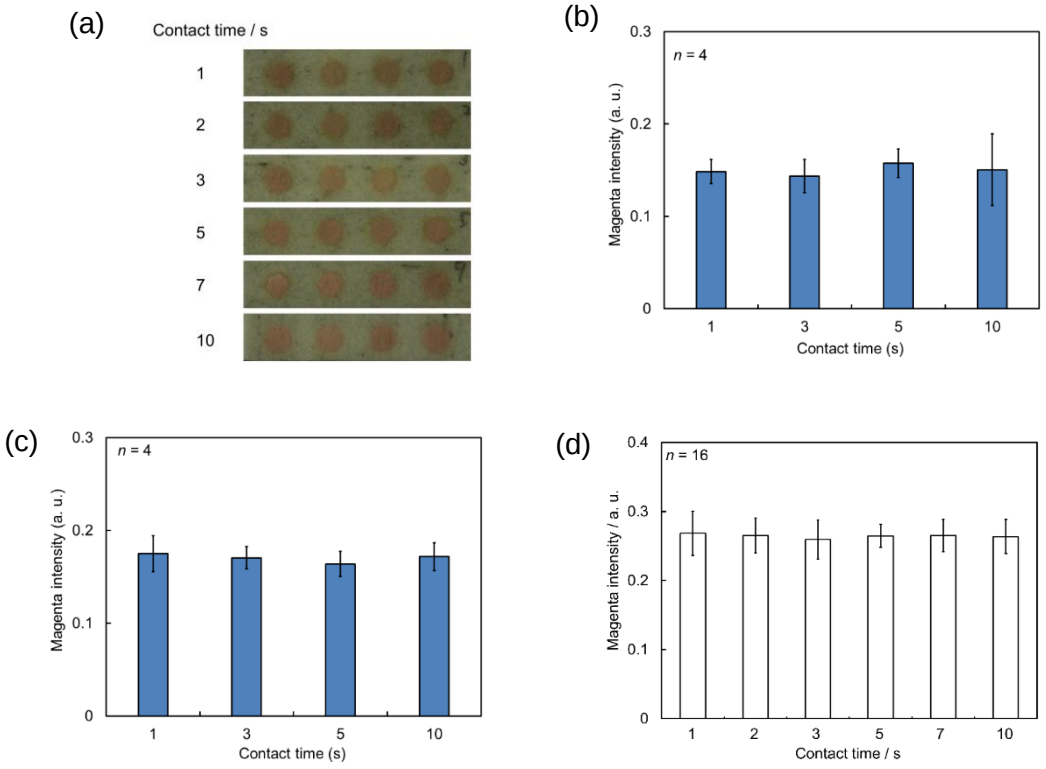

Figure 4.10 Estimation of the effect of different contact times on magenta intensity. (a) Relationship between the magenta intensity and contact time of the detection unit. Photographs of detection units after color formation with blood samples spiked with 2 mM Li^+ at different contact times. Estimation of the effect of contact time on magenta intensity for a 0.5 mM (b), 1.0 mM (c) and 2.0 mM (d) Li^+ standard sample. The magenta intensity was independent of contact time.

4.3.3 Comparison of the measurement performance with conventional methods

Under the optimized conditions, I compared the sensitivity, accuracy, and reproducibility of my paper-based method and those of conventional colorimetric methods (microplate well and cuvette). The experimental procedure was the same as that described above. In the conventional methods, a solution of lithium salt and the detection reagent were mixed in a volume ratio of 1:60, and the mixture was incubated at 37 °C for 10 min in accordance with the kit protocol. Figure 4.11a shows photographs of the detection unit after contact with the separation unit and Figure 4.11b shows the standard curves for lithium-ion detection with my device, a microplate well, and a cuvette. These results indicate that the calibration curve using the present device displays a good linearity with small error bars and R^2 = 0.991. The limits of detection (LOD, blank + $3SD_{Blank}$) and the maximum value of the coefficient of variation (CV) in the range examined in this study are listed in Table 4.1. Using my device, I achieved a low LOD (0.054 mM) and high accuracy and reproducibility values, comparable to those of conventional methods.

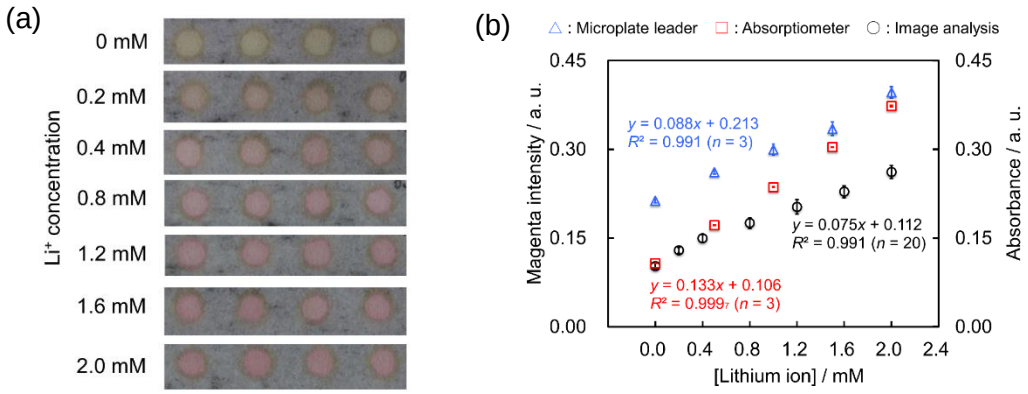

Figure 4.11 Measurement of standard samples using my device and conventional methods. (a) Photographs show the detection units after contact with the separation units. The magenta intensity increased with increasing lithium ion concentration in the standard samples. (b) The calibration curve obtained using my device (black plots) shows good linearity and coefficient of determination and small error bars in the measured range (comparable to that of conventional methods). The blue and red points indicate data for the microplate reader and the spectrophotometer, respectively.

Table 4.1. Comparison of measurement ability between my device and conventional methods

	Measurement method		
	Image analysis	Spectrophotometer	Microplate reader
LOD (mM)	0.054	0.021	0.123
CV (%)	6.05	0.44	3.46

4.3.4 Demonstration of the measurement of the Li^+ concentration using spiked blood samples

To evaluate the measurement performance, I determined the lithium ion concentration in Li^+ spiked whole blood samples; each sample concentration was prepared in the same volume ratio of 4 mL whole blood to 1 mL Li^+ solution. Figure 4.12a shows a photograph of the detection units after the development of color caused by the presence of Li^+ in the spiked samples. The magenta intensity increased with increase in the lithium ion concentration in the spiked blood samples. After the image analysis of the photograph, the magenta intensity was plotted against the lithium ion concentration in the blood as shown in Figure 4.12b. The data show good linearity and correlation in the measured range, comparable to that of the standard samples. The LOD and the maximum value of CV in the measured range were 0.281 mM and 12.4%, respectively. This result indicates that my device is able to determine the lithium ion concentration in blood. Although the LOD of my device (0.281 mM) was similar or inferior to previously reported values [23, 27–30], it was still sufficient to meet the requirements of clinical testing. However, the magenta intensity and the measurement sensitivity with the spiked blood samples were lower than those of the standard samples. This difference is possibly due to the poor lithium ion migration because of the high viscosity of the blood. Table 4.2 shows the recovery rates obtained by comparing the color intensity of the standard sample with the results of conventional methods. The present device provided high recovery of 90.0 ± 4.5% to 97.6 ± 3.4% with good CV of 3.4% to 9.8%. Subsequently, I measured the magenta intensity of 1-mM Li^+ whole blood samples with high concentrations of Na^+ and/or K^+ (>200 mM and >4 mM, respectively) to evaluate the influence of other metal ions on lithium

quantitation. Additionally, whole blood samples that comprise no Li^+ were observed to constitute high concentrations of Na^+, K^+, and/or Mg^{2+} (>200 mM, >4 mM, and >20 mM respectively). Each experiment was performed four times using the contact method. As shown in Figure 4.12c, the measurement outcome was unaffected by 200 mM Na^+, 4 mM K^+ and 20 mM Mg^{2+}. As the sodium, potassium and magnesium ion concentrations of blood used in this experiment were unknown, the sodium, potassium and magnesium levels of spiked samples exceeded the above values. Even under such conditions, these ions did not affect the measurement. These results indicate that the present device can be used as an alternative method for the determination of the lithium ion concentration in blood. In terms of accuracy and precision, my device showed comparable or worse performance than previously described devices, which presents one of the challenges of paper-based device development. To improve accuracy and precision, I need to develop a novel detection reagent for lithium ions or a novel paper substrate with controlled architecture of cellulose fibers. The difference between the spiked and found values is possibly due to the poor migration of lithium-ions because of the high viscosity of blood. I believe that the low values obtained at high lithium ion concentrations can be solved by optimizing the contact position of the detection unit with the separation unit.

Overall, my results indicate that the paper-based device enables the simple determination of the lithium ion concentration in blood. I believe that improvements in the sensitivity, accuracy, and reproducibility can be achieved by fabricating a uniform detection window size, optimizing the concentration of the detection reagent, and using a consistent drying atmosphere for the detection reagent.

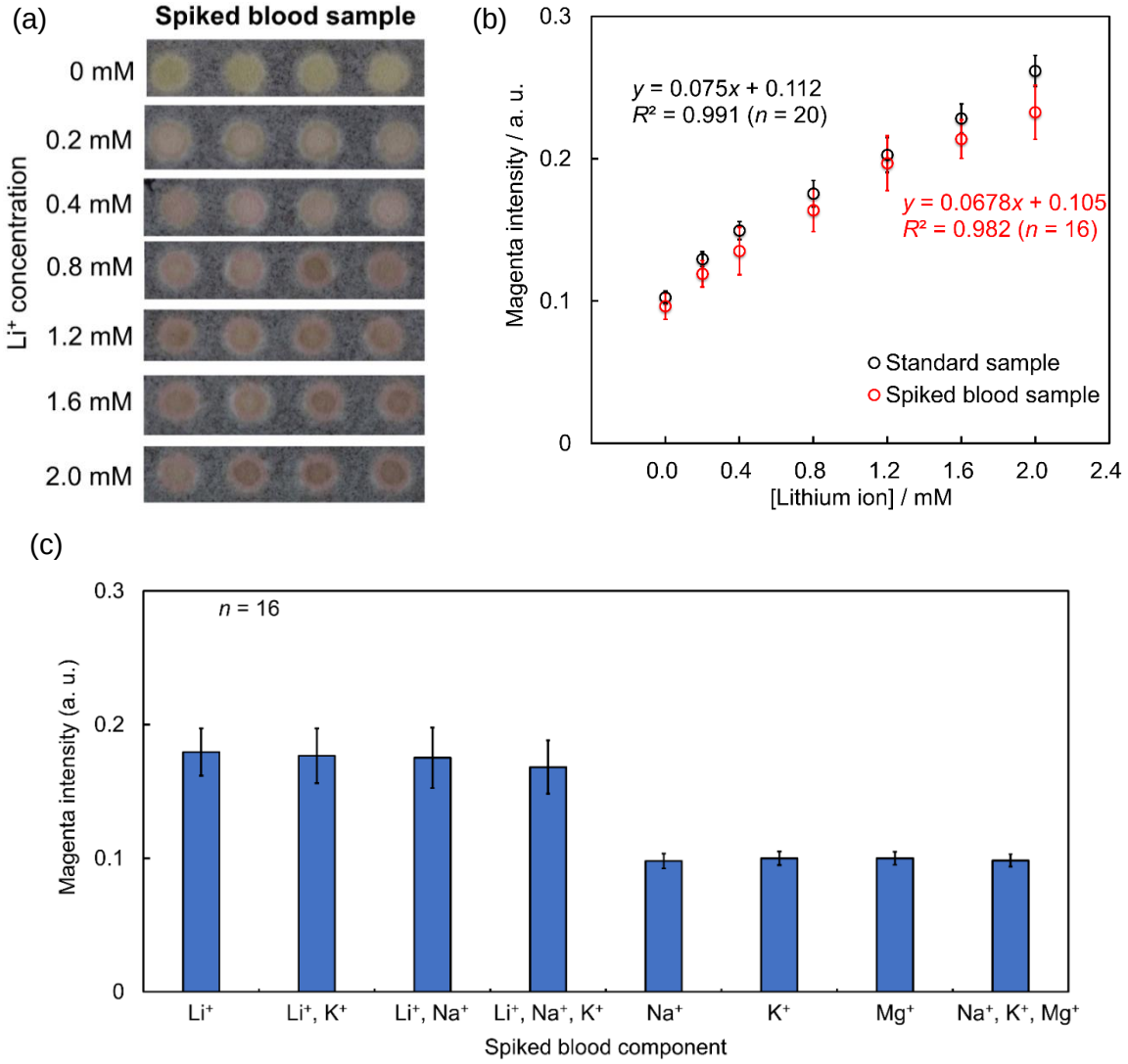

Figure 4.12 Demonstration of the measurement of lithium ion concentration in spiked blood samples using my device. (a) Photographs show the detection units after contact with the separation units. The magenta intensity increased with increasing [Li^+] in the spiked blood samples. (b) The plots show good linearity and coefficients of determination and small error bars, compared with the results obtained with the standard samples. The magenta intensity was a little lower than that of the standard sample because of the trapping of lithium ions in the separation process. (c) Influence of other metal ions on the quantitation of lithium ions in whole blood. Measurements were performed for spiked blood samples (1 mM Li^+) containing >200 mM Na^+ or/and >4 mM K^+, and negative blood samples (no-Li^+) containing >200 mM Na^+, >4 mM K^+ or/and >20 mM Mg^{2+}. In both conditions (positive and negative samples), the magenta intensity of each sample was constant, which confirmed that at the specified concentrations, the above-mentioned ions do not interfere with lithium detection

Table 4.2 Measurement of lithium ion concentration in spiked blood samples using my device (n = 16)

Spiked Li^+ ion concentration (mM)	Found concentration (mM)	Recovery (%)	RSD (%)
0	-0.07 ± 0.07	94.8 ± 5.4	5.7
0.2	0.22 ± 0.06	92.8 ± 3.7	4.0
0.4	0.43 ± 0.15	91.6 ± 9.0	9.8
0.8	0.79 ± 0.13	94.6 ± 4.9	5.2
1.2	1.21 ± 0.17	97.6 ± 3.4	3.4
1.6	1.43 ± 0.09	95.2 ± 3.6	3.8
2.0	1.67 ± 0.15	90.0 ± 4.5	5.0

Subsequently, I tested the measurement of the lithium ion concentration in small volumes of spiked blood. The injection volumes of the spiked samples were 10, 15, and 20 μL. The experimental procedure was identical to that described previously. Figure 4.13a show photographs after RBC separation and lithium ion detection using different injection volumes of spiked blood samples, respectively. An increasingly magenta color with increasing lithium ion concentration is visible in the detection window by the naked eye. The plots of the magenta intensities obtained with different injection volumes of spiked samples are shown in Fig. 4.13c. The magenta intensities were higher than those previously obtained in this study (Figure 4.12b) because of the slight hemolysis of the blood. However, as shown in Figure 4.13b, the plots have almost the same slope and small error bars (11.2%, 10.2%, and 12.4%,) for injection volumes of 10, 15, and 20 μL, respectively, and good coefficients of determination (R^2 > 0.982). Furthermore, the LODs were 0.357, 0.350, and 0.391 mM for the injection volumes of 10, 15, and 20 μL, respectively. These results indicate that the sensitivity and the

reproducibility of lithium ion measurement using my device was independent of the injection volume of the spiked blood samples. This study confirms that the proposed device is suitable for the POCT of lithium ion concentration in small volume whole blood samples.

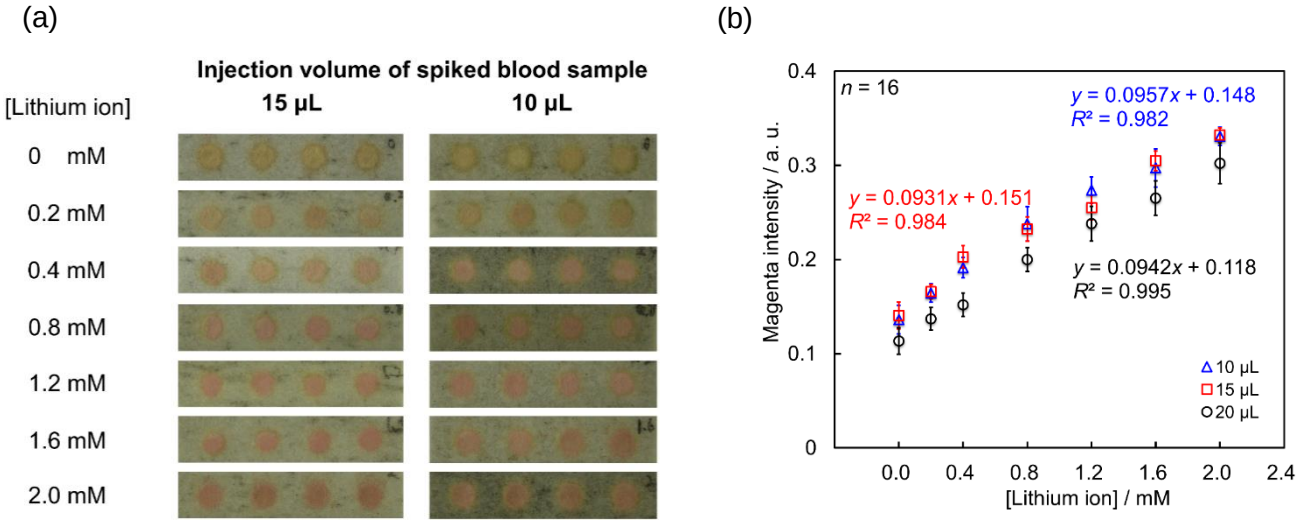

Fig. 4.13 Demonstration of the measurement of lithium ion concentration in spiked blood samples using my device. (a) Demonstration of the detection of lithium ion with spiked blood samples. Photographs of detection units after detection of lithium ion in spiked blood samples with different injection volumes of 15 μL (left) and 10 μL (right). (b) Lithium ion concentration in small-volume, spiked blood samples. Under all conditions, the same slope was obtained with a good coefficient of determination and small error bars. The plots for injection volumes of 20 μL are higher than that shown in Figure 4.12b because of hemolysis.

4.4 Conclusions

I succeeded in the development of the paper-based device (PAD) for determination of Li^+ concentration in human whole blood. My developed PAD overcomes the drawbacks of PAD towards blood tests, and realized a facile, user friendly, and quantitative colorimetric method. In this study, I used a digital camera to obtain the image for image analysis without any fixed light condition. My method has good compatibility with smartphone-based analysis because the detection is based on colorimetry. However,

smartphone cameras have lower resolution than a digital camera. In future, I want to adapt my method for smartphone-based analysis by developing a portable shooting box for acquiring images under fixed shooting conditions or by using machine-leaning image analysis. In previous reports, the determination of the lithium ion concentration in blood has used electrochemical approaches using a glass substrate to achieve high sensitivity and blood cell separation or direct measurement. Although an increased coefficient of variation is required for use in POCT, my developed paper-based device has a comparable measurement ability to those of conventional methods. Thus, this device provides an alternative method for the determination of the lithium ion concentration in human blood in the treatment of bipolar disorder. Finally, I expect my PAD has overcame the problems of PADs toward blood tests and will be able to apply various blood tests for detecting a single analyte or multi-analytes to achieve on-site analysis with PADs.

4.5 Reference

[1] F. K. Goodwin and K. R. Jamison, Manic-depressive illness: bipolar disorders and recurrent depression (Vol. 1), Oxford University Press (2007).

[2] M. Bauer, J. Unützer, H. A. Pincus, and B. L. William, *Ment Health Serv Res*, **4**, 225-229 (2002).

[3] E. X. Vrouwe, R. Luttge, I. Vermes and A. van den Berg, *Clin Chem.*, **53**, 117-123 (2007).

[4] A. J. Gelenberg, J. M. Kane, M. B. Keller, P. Lavori, J. F. Rosenbaum,; K. Cole and J. Lavelle, *N Engl J Med*, **321**, 1489-1493 (1989).

[5] R. H. Perlis, G. S. Sachs, B. Lafer, M. W. Otto, S. V. Faraone, J. M. Kane and J. F. Rosenbaum, *Am J Psychiatry*, **159**, 1155-1159 (2002).

[6] A. Coppen, M. Abou-Saleh, P. Milln, J. Bailey and K. Wood, *J Affect Disord*, **5**, 353-362 (1983).

[7] W. Greil, W. Ludwig-Mayerhofer, N. Erazo, C. Schöchlin, S. Schmidt, R. R. Engel, A. Czernik, H. Giedke, B. Müller-Oerlinghausen, M. Osterheider, G. A. E. Rudolf, H. Sauer, J. Tegeler and T. Wetterling, *J Affect Disord*, **43**, 151-161 (1997).

[8] J. Baird-Gunning, T. Lea-Henry, L. C. G. Hoegberg, S. Gosselin and D. M. Roberts, *J Intensive Care Med*, **32**, 249-263 (2017).

[9] H. S. Hopkins and A. J. Gelenberg, *Bipolar Disord.*, *2* (3 Pt 1), 174-179 (2000).

[10] F. Colom, E. Vieta, J. Sánchez Moreno, A. Martínez Arán, M. Reinares, J. M. Goikolea and J. Scott, *Bipolar Disord.*, **7**, 32-36, (2005).

[11] W. E. Q Severus, N. Kleindienst, F. Seemüller, S. Frangou, H. J. Möller and W. Greil, *Bipolar Disord.*, **10**, 231-237 (2008).

[12] D. S. Reddy and M. S. Reddy, *Indian J. Psychol. Med.*, **36**, 346-347, (2014).

[13] K. P. Chen, W. W. Shen and M. L. Lu, *Psychiatry Clin. Neurosci.*, **58**, 25-29, (2004).

[14] J. A. Bowman, *Anal. Chim. Acta*, **37**, 465-471, (1967).

[15] B. F. Rocks, R. A. Sherwood and C. Riley, *Clin. Chem.*, **28**, 440-443 (1982).

[16] G. N. Doku and V. P. Y. Gadzekpo, *Talanta*, **43**, 735-739 (1996).

[17] E. Metzger, D. Ammann, W. Simon and R. Asper, *Anal. Chem.*, **58**, 132-135 (1986).

[18] R. L. Bertholf, M. G. Savory, K. H. Winborne, J. C. Hundley, G. M. Plummer and J. Savory, *Clin. Chem.*, **34**, 1500-1502 (1988).

[19] S. Sawada, H. Torii, T. Osakai and T. Kimoto, *Anal. Chem.*, **70**, 4286-4290 (1998).

[20] E. X. Vrouwe, R. Luttge and A. van den Berg, *Electrophoresis*, **25**, 1660-1667 (2004).

[21] E. Chapoteau, B. P. Czech, W. Zazulak and A. Kumar, *Clin. Chem.*, **38**, 1654-1657 (1992).

[22] S. O. Obare, R. E. Hollowell and C. J. Murphy, *Langmuir*, **18**, 10407-10410 (2002).

[23] W. M. Glazer, J. G. Sonnenberg, M. J. Reinstein and R. F. Akers, *J. Clin. Psychiatry*, **65**, 652-655 (2004).

[24] S. O. Obare and C. J. Murphy, *Inorg. Chem.*, **40**, 6080-6082 (2001).

[25] T. Gunnlaugsson, B. Bichell and C. Nolan, *Tetrahedron Lett.*, **43**, 4989-4992 (2002).

[26] T. Gunnlaugsson, B. Bichell and C. Nolan, *Tetrahedron*, **60**, 5799-5806 (2004).

[27] E. X. Vrouwe, R. Luttge, W. Olthuis and A. van den Berg, *Electrophoresis*, **26**, 3032-3042 (2005).

[28] A. Floris, S. Staal, S. Lenk, E. Staijen, D. Kohlheyer, J. Eijkel and A. van den Berg, *Lab Chip*, **10**, 1799-1806 (2010).

[29] P. Kubáň and P. C. Hauser, *Lab Chip*, **8**, 1829-1836 (2008).

[30] M. Novell, T. Guinovart, P. Blondeau, F. X. Rius and F. J. Andrade, *Lab Chip*, **14**, 1308-1314 (2014).

[31] M. Wu, Q. Lai, Q. Ju, L. Li, H. D. Yu and W. Huang, *Biosens. Bioelectron.*, **102**, 256-266 (2018).

[32] P. Sandbhor Gaikwad and R. Banerjee, *Analyst*, **143**, 1326-1348 (2018).

[33] M. Sher, R. Zhuang, U. Demirci and W. Asghar, *Expert Rev. Mol. Diagn.*, **17**, 351-366 (2017).

[34] K. Mahato, A. Srivastava and P. Chandra, *Biosens. Bioelectron.*, **96**, 246-259 (2017).

[35] M. I. G. S. Almeida, B. M. Jayawardane, S. D. Kolev and I. D. McKelvie, *Talanta*, **177**, 176-190 (2018).

[36] Y. Lin, D. Gritsenko, S. Feng, Y. C. Teh, X. Lu and J. Xu, *Biosens. Bioelectron.*, **83**, 256-266 (2016).

[37] N. A. Meredith, C. Quinn, D. M. Cate, T. H. Reilly, J. Volckens and C. S. Henry, *Analyst*, **141**, 1874-1887 (2016).

[38] L. S. A. Busa, S. Mohammadi, M. Maeki, A. Ishida, H. Tani and M. Tokeshi, *Micromachines*, **7**, 86 (2016).

[39] S. Mohammadi, M. Maeki, A. Ishida, H. Tani and M. Tokeshi, *Analyst*, **140**, 6493-6499 (2015).

[40] T. Komatsu, S. Mohammadi, L. S. A. Busa, M. Maeki, A. Ishida, H. Tani and M. Tokeshi, *Analyst*, 141, 6507-6509 (2016).

[41] T. Komatsu, M. Maeki, A. Ishida, H. Tani and M. Tokeshi, *Anal. Sci.*, **34**, 39-44 (2018).

[42] A. W. Martinez, S. T. Phillips, E. Carrilho, S. W. Thomas, H. Sindi and G. M. Whitesides, *Anal. Chem.*, **80**, 3699-3707 (2008).

CHAPTER 5 Development of Fusion Device for Determining Blood Lithium Ion Concentrations

5.1 Introduction

Most blood tests require the separation of plasma to achieve precise results as blood cells affect the test result.[1, 2] Plasma separation involves the elimination of blood cells from whole blood and the segregation of the plasma into a fixed volume.[3] Blood tests are regulated based on the amount of substance per unit volume of the serum or plasma. Thus, controlling the volume of the serum or the plasma is an essential manipulation for determining the target concentration using blood tests. Further, the blood samples only have a tiny volume so that diagnoses can be minimally invasive. These points are the problem to be solved for developing paper-based device towards blood test as described in General Introduction. Many microfluidic techniques and lab-on-a-chip devices for blood separation have been developed because of the growing global demand for point-of-care testing.[4, 5] These techniques typically employ the centrifugal force [1, 6–8], filtration [8-10], capillary force [11-16], and dielectrophoresis (DEP) [16–20]. Centrifugal force generated by using a rotation disk or a stacking spiral microchannel can help separate plasma generated by a centrifugal field owing to the difference in the mass density of blood cells and plasma. Filtration provides plasma by capturing blood cells using microsized pores. Capillary force involves the use of combined additional force (modification of channel, special channel designs, dielectrophoresis) for attracting blood cells; however, paper-materials can separate the plasma using only capillary force when capturing blood cells via microsized pores. The negative DEP force, which is an electrokinetic force, repels blood cells on the voltage-applied electrode generated electric fields for separating the plasma. However, they usually require large-volume samples that need to be pre-diluted offline; they also suffer from unfavorable hemolysis and clogging along the channels and microstructures in the devices. Furthermore, the most significant challenge lies in obtaining plasma with a precisely controlled volume after separating the blood cells. Although there are several droplet-based microfluidic devices [21, 22] that can overcome these disadvantages, they only manipulate the blood by controlling the fluid with a complicated channel design at precise flow rates.

In contrast, digital microfluidics (DMF) is a droplet-based microfluidic technique that enables the simple manipulation of plasma droplets with a controlled volume via electrowetting on a dielectric

(EWOD).[23–28] The droplet manipulation is performed between two parallel plates that have thin-film electrodes. The electrode size and the distance between the two plates can determine the droplet volume. Furthermore, DEP and electrophoresis are potential separation techniques that can be executed on an integrated DMF platform.[29–34] Red blood cells are driven with a negative DEP force such that they can be separated from the blood.[18, 19] Traveling wave DEP has been used to separate red blood cells; it provides a large droplet without red blood cells that forms via a continuous flow.[18] Liao et al. performed [19] on-chip capillary electrophoresis to separate red blood cells. These studies only focused on separating red blood cells; thus, the resultant blood may contain other blood cells, such as leukocytes and platelets. Recently, Dixon et al. reported [3] a plasma separation system for blood tests; this system was based on a DMF device that was integrated with a blood cell separation filter. This passive approach requires a larger amount of whole blood (50 μL) and diluted plasma in the extraction procedure; further, it entails evaporation of liquids including blood, extracted plasma, and detection reagents in ambient air. Presently, separating and metering plasma droplets with a controlled volume directly from whole blood has not been achieved with DMF devices.

In the case of DMF platforms, the amount of analyzed sample is limited to small volumes of the order of nanoliters to microliters. Thus, they are compatible with fluorometric or chemiluminescence detection, which can achieve in-situ highly sensitive detection of the droplets.[35–39] However, this detection technique is not ideal for point-of-care testing since optical systems typically require bulky equipment. This includes controllers, light sources, and a variety of optical parts such as lenses, filters, mirrors, and a photosensor. In this regard, electrochemical detection can be an alternative technique for droplet detection using proper sensing electrodes on DMF devices. This technique has a higher sensitivity than fluorometric detection.[40–42] To extend the droplet manipulation advantages of DMF, a DMF platform with a replaceable cartridge for electrochemical detection was reported.[42] This allowed several types of sensors to be attached to the cartridge instead of permanent integration.[42] In addition, Ng et al. reported [43] the remote setting of the DMF system for POC serological immunoassay in a refugee camp in Kenya; however, too they required plasma separation using a centrifuge.

Recently, paper-based analytical devices (μPADs) have been developed for the point-of-care diagnosis of blood and urine, as well as for food/environmental safety tests. This is because paper materials have a low expense and high portability.[44–47] In particular, the development of μPADs for blood tests can reduce the required blood/reagent volume and integrate the analytical procedures. These reports achieved the rapid detection of target molecules in whole blood by introducing an accurate volume of blood sample into the μPAD with a micropipette. Therefore, the reported μPADs are not fully automated: micropipetting is essential for sample dispensing, and the precise volume of micropipette-transported plasma should be known for reliable diagnostic results.

In this study, I selected the lithium ion (Li^+) as a model target for the blood test. Li^+ has a therapeutic effect on bipolar disorder [48], which is a mood disorder, and its concentration in whole blood has to be regularly inspected for adequate treatments.[49] The therapeutic concentration range of Li^+ is 0.4 to 1.2 mM, and the toxic concentration is 1.5 mM or more.[50–54] To date, electrochemical methods/electrophoresis and colorimetry have been employed for the point-of-care testing of Li^+ concentration in whole blood; however, the reported methods have some limitations. These include the use of micropipettes, the requirement of a large amount of blood, the off-chip dilution of blood, and the necessity of a high temperature during the operation (70 °C).[55–59] To overcome these shortcomings, I previously reported a facile colorimetric method for determining the Li^+ concentration in whole blood with PAD.[60] However, my prior method still requires a large amount of blood (20 μL) that can be dispensed using a micropipette.

In this study, I developed a fusion device that integrates analytical manipulation based on plasma separation to detect the Li^+ concentration in whole blood. The developed PAD in Chapter 4 still requires the improvements: (i) more reduction of required blood volume and (ii) non-requirement of the blood introduction of certain volume. To achieve (i) and (ii), I invented the fusion device that is consisted of DMF unit and five circle paper sensors (PAD unit). For plasma separation with DMF unit, EWOD and DEP are simultaneously performed on the DMF platform. This has been demonstrated in my previous studies [29–34], in which the device manipulates the liquid samples and particles/cells via frequency modulation using a single DMF chip.

For Li^+ detection, paper sensors were fabricated by drying and concentrating the detection reagent (F28 tetraphenylporphyrin) on a filter paper, based on my previous study.[60] I achieved plasma separation with adjustable droplet volumes by using particle/liquid DEP and EWOD on a single DMF platform to separate a small amount of whole blood samples (a few microliters) with a separation efficiency greater than 90%. In a proof-of-concept study, as expected, the DMF–paper fusion device achieved the required measurement performance for the Li^+ test in ambient silicone oil. The limit of detection (LOD) was 0.267 mM, and the coefficients of variation (CVs) in the measuring range were less than 9.5%. In order to determine the Li^+ concentration in whole blood, the developed fusion device completed five serial replications within 20 min. The data plots obtained by my device are in good agreement with those obtained via a conventional method when the corresponding kit protocol is used. This indicates that the developed fusion device can be a potent therapeutic tool for the rapid detection of Li^+ in whole blood.

5.2 Experimental

5.2.1 Reagents and chemicals

Indium tin oxide (ITO)-coated glass plates (Ruilong, Taiwan) with square-surface resistivities of 7 and 450 Ω/sq were used respectively to fabricate the bottom and top plates with patterned electrodes. Acetone and isopropanol (E-Shine Advanced Chemical, Taiwan) were used for washing the glass substrates. A positive photoresist FH-6400L, a photoresist developer FHD-5, and a photoresist stripping solution MS-2001 (Fuji film Electric Materials, Japan) were used for the photolithography process. Parylene-C (Suzhou Parylene Materials, China) was coated with chemical vapor deposition equipment (Deree Technologies, Taiwan), which was the first dielectric layer. An SU-8 2002 photoresist (Microchem, USA) was employed as the second dielectric layer on the bottom plate. A Teflon 0.5% (w/v) solution was prepared with Teflon® AF1600 (Chemours, USA) and FC-770 (3M, USA) for the hydrophobic coatings. F28 tetraphenylporphyrin (0.168 mg/mL), which was included in a colorimetric assay kit (ESPA Li II, NIPRO, Japan), was used as a Li^+ detection reagent (see

Fig. 5.1). Quantitative filter paper #1 (21 cm × 29.7 cm, thickness 200 μm, Advantech MFS, USA) was used to prepare the paper sensors. Pluronic® F-127 (Sigma-Aldrich, USA) was added in the liquids to adjust the surface tension to achieve efficient DMF actuations. All of the spiked blood samples (0–2 mM) with 0.5% F-127 were prepared by mixing a Li^+ standard solution/1% HNO_3 (approximately 1436 mM, National Institute of Standards and Technology, USA) and human whole blood in ethylenediaminetetraacetic acid (EDTA) with a volume ratio of 1:18. For the preparation of the blood samples, I used 1 × phosphate buffered saline (PBS) by mixing 10 × PBS buffer (pH 7.4) and ultrapure water (18 MΩ-cm).

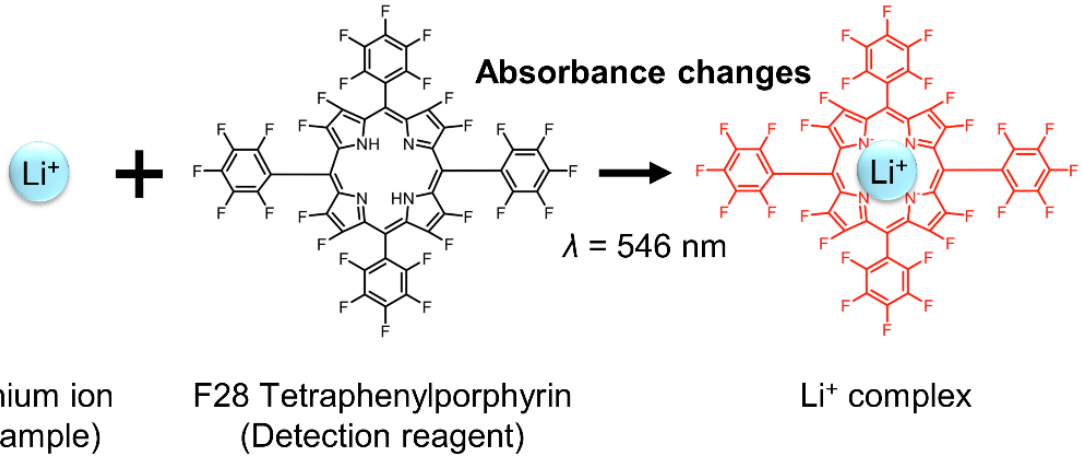

Figure 5.1 Scheme for the reaction of lithium-ion (Li^+) with F28 tetraphenylporphyrin included in a commercially available colorimetric assay kit. Li^+ in a sample reacted with the detection reagent to provide the color change from yellow to red (λ = 546 nm).

5.2.2 Principle of manipulation of liquid and particle with digital microfluidics

5.2.2.1 Electrowetting-on-dielectric

Electrowetting-on-dielectric (EWOD) is well-known as an actuation mechanism for a small droplet of liquids.[23] EWOD changes the apparent contact angle of a conductive liquid droplet on a solid electrode coated with dielectric and hydrophobic layers and applied with a voltage. According to the Lippmann–Young equation, the contact angle varies from θ_0 to θ (V) on an applied voltage V_{LF} across a dielectric layer as follows:

$$\cos\theta(V) = \cos\theta_0 + \frac{\varepsilon_0\varepsilon_D}{2\gamma_{LG}\cdot t}{V_{LF}}^2, \quad (1)$$

where ε_0 denotes the permittivity of vacuum (8.85×10^{-12} F/m), ε_D denotes the relative permittivity of the dielectric layer of thickness t, γ_{LG} represents the liquid–gas interfacial tension, and V_{LF} denotes the voltage drop across the dielectric layer (Fig. 5.2, left).

A pumping force F_{EWOD} of the droplet (Fig. 5.2, left) can be derived from the Laplace–Young equation based on the pressure difference between the two ends of the droplet (width W) as

$$F_{EWOD} = \frac{\varepsilon_0\varepsilon_D W}{2t}{V_{LF}}^2. \quad (2)$$

For the manipulation of all samples including whole blood with 0.1% F-127, a Li^+ standard solution with 0.5% F-127, Li^+ spiked plasma sample with 0.5% F-127, and Li^+ spiked blood sample with 0.5% F-127, I measured the contact angle variation of 1.5 μL droplets on the unpatterned ITO glass plates covered with dielectric and hydrophobic layers by applying 1-kHz square-wave AC signals at 0–100 V_{rms} (Table 5.1) between ITO and a tungsten wire (diameter 70 μm) inserted in to the droplets.

5.2.2.2 Dielectrophoresis on particles (PDEP)

The dielectrophoretic (DEP) force exerting on a spherical particle of radius r, F_{PDEP}, is described as

$$F_{PDEP} = 2\pi r^3 \varepsilon_L \mathrm{Re}\left(\frac{{\varepsilon_P}^* - {\varepsilon_L}^*}{{\varepsilon_P}^* + 2{\varepsilon_L}^*}\right)\nabla E^2, \quad (3)$$

where E denotes electric field, and ε_P* and ε_L* denote the complex permittivities of the manipulated particles and of the suspension liquid, respectively, which depend on frequency. This is expressed as

$${\varepsilon_{P,L}}^* = \varepsilon_0\varepsilon_{P,L} - j\frac{\sigma_{P,L}}{2\pi f}, \quad (4)$$

where $\varepsilon_{P,L}$ represents the relative permittivity and $\sigma_{P,L}$ denotes the conductivity of the particle or the suspension liquid; and f denotes the frequency of the electric field. From a previous report [18], blood cells were repelled from the regions of large field strength by negative DEP, as shown in Fig. 5.2 center, PDEP.

5.2.2.3 Dielectrophoresis on liquids (LDEP)

Further, DEP supplies surface forces to draw bulk liquids including dielectric liquids of greater relative permittivity into a region of a strong electric field of a smaller relative permittivity.[34] For example, I drove plasma in a silicone oil environment in this study. As shown in Fig. 5.2 right, LDEP, on applying voltage V_{HF} between parallel electrodes (spacing d) and neglecting the voltage in the dielectric layer, the plasma is attracted toward the region of strong electric field with a dielectrophoretic force F_{LDEP}

$$F_{LDEP} = \frac{\varepsilon_0(\varepsilon_{plasma}-\varepsilon_{oil})W}{2d} {V_{HF}}^2,$$

where ε_{plasma} and ε_{oil} are the relative permittivities of plasma and oil, respectively.

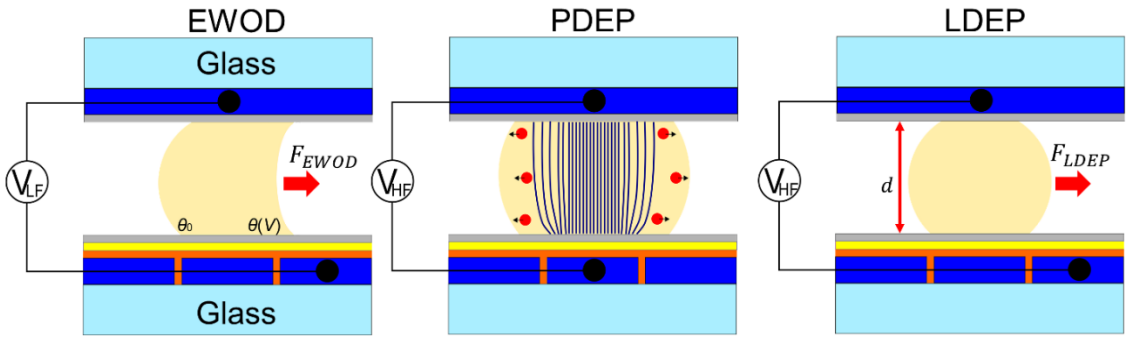

Figure 5.2 The manipulations of the whole blood on the DMF device. The illustration of the cross section of the DMF device showing the principle of EWOD, PDEP, and LDEP.

Table 5.1 Measurement of the contact angle on representative samples in my study (mean ± s.e.m., n = 3)

	Contact angle (deg)	
	Initial (0 Vrms)	100 Vrms
2 mM Li^+ spiked blood sample	87.5±2.0	45.1±2.5
2 mM Li^+ spiked plasma sample	93.4±1.0	48.3±1.9
2 mM Li^+ standard sample	83.1±0.1	53.6±1.1

5.2.2 Fabrication of the fusion device

The fusion device consisted of a DMF unit and PAD unit which has five preloaded paper sensors, as shown in Fig. 5.3. I embedded five paper sensors in DMF unit for detecting Li^+ in single whole blood sample at 5 times on the fusion device. Thus, my fusion device has a potential for determining multi-components in whole blood by embedding several paper sensors which are retained different detection reagents. Furthermore, my electrode design of DMF device can be easily parallelized and resized for achieving a high-throughput. By combining my image analysis method described in Chapter 3, I will be provided the automatic analytical system for determining multi-components in whole blood in the future. In this thesis, I could not demonstrate the detection of multi-analytes in whole blood.

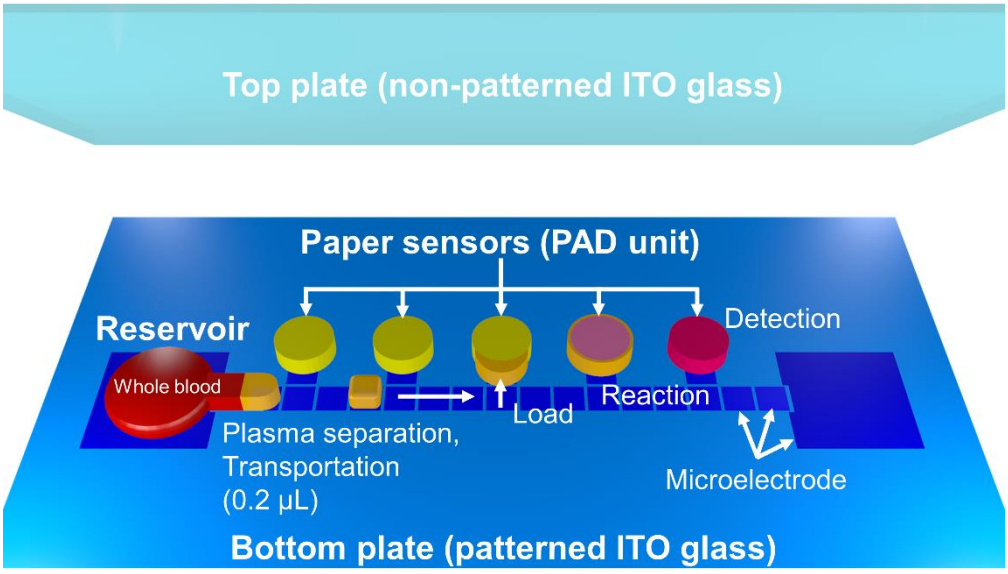

Fig. 5.3 Illustration of the fusion device to detect Li^+ in whole blood. The separated plasma droplets with DMF unit were transported to the paper sensors of PAD unit through the electrode array; the color of the paper sensors was changed to red due to the production of the Li^+-F28 tetraphenylporphyrin complex.

To prepare the paper sensors, a filter paper was cut into 1 cm × 4 cm pieces considering ease of fabrication and fabrication efficiency. In addition, a total of 350 μL (separately 70 μL for five times) of the detection reagent was loaded onto each paper piece that was cut and it was dried in the dark at room temperature (300 K).

Circular paper sensors (diameter 2 mm) were prepared by punching out the soaked and dried filter paper. As demonstrated in Fig. 5.3, the DMF device consisted of two parallel plates. Each plate was cut into 4 cm × 5 cm (thickness ~1 mm). The top glass plate contained an unpatterned ITO layer, which served as a transparent electrode. A hydrophobic layer (thickness 55 nm) was spin-coated with a 0.5% Teflon solution to facilitate the droplet movements. The bottom plate was fabricated by standard photolithography processes. The electrode design is shown in Fig. 5.4a. First, an ITO glass substrate was cleaned with acetone, isopropanol, and deionized water in an ultrasonic bath for 5 min each. These cleaning steps are important to wash away impurities on the surface of the glass substrate and to construct a precise electrode design. The positive photoresist was spin-coated on the bottom plate at 3000 rpm for 30 s (thickness 1.4 μm). After soft baking at 95 °C for 5 min, the bottom plate was aligned with the photomask and it was exposed to UV radiation with a mask aligner (USHIO, Japan) for 3.5 s. The UV exposed bottom plate was developed in FHD-5 for around 20 s and it was immersed in deionized water for 5 min. The bottom ITO plate was then etched in an aqua regia solution (HNO3:HCl:H2O = 1:3:6) at 49 °C for 200 s. After removing the photoresist with MS-2001, the bottom plate was washed with deionized water and dried on a hot plate at 150 °C. Subsequently, a parylene-C layer (thickness, 2 μm) and a SU-8 layer (thickness, 1.7 μm) were deposited. Finally, a Teflon layer (thickness, 55 nm) was spin-coated on the SU-8 coated substrate to obtain a hydrophobic surface.

To set the fusion device, five paper sensors were placed at the bottom plate and they were overlapped with the electrodes to transport the droplets. Before usage, five pieces of paper sensors were wetted with 0.2 μL detection reagent each to reduce the silicone oil absorption and to enhance their stiction on the bottom plate during the device preparation and assembly (see Figs. 5.4 b,c). Before placing the top plate, a sample solution (5 μL) was dispensed on the reservoir region of the bottom plate with preloaded paper sensors and spacers (thickness of 200 μm). The assembled top and bottom plates were fixed with binder clips.

(a)

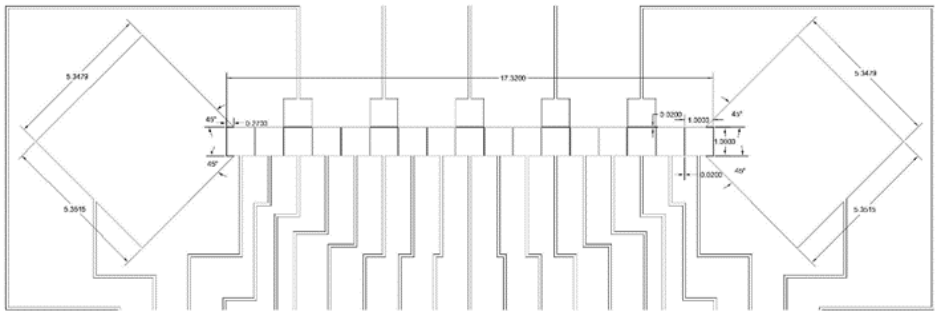

(b) (c)

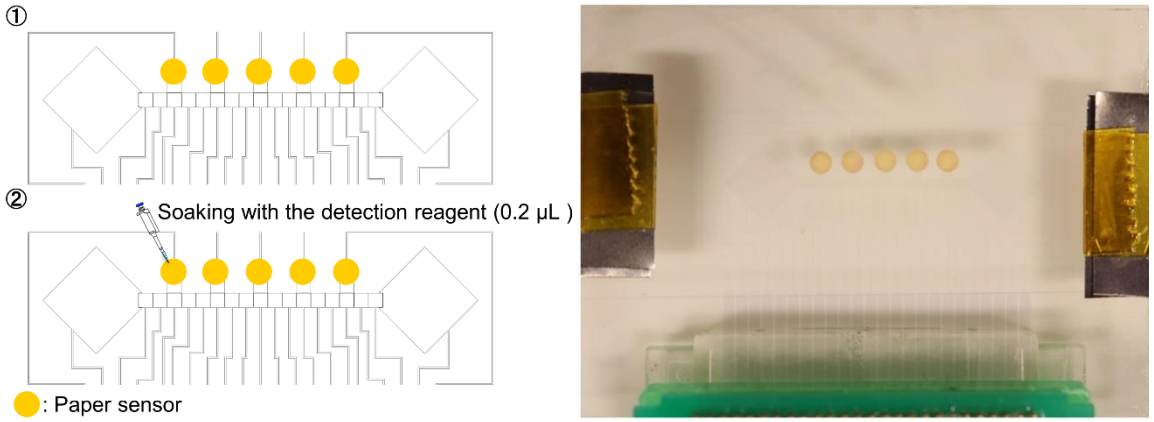

Figure 5.4 (a) Design of the electrode design for the fusion device. (b) Preparation of the fusion device: (1) deploying paper sensors on the bottom plate, and (2) loading detection reagent of 0.2 μL on all paper sensors to improve interface adherence. (c) Photograph of the complete fusion device before loading 2cSt silicone oil.

5.2.3 Manipulation of plasma separation with DMF

The instrumental setup of DMF is illustrated in Fig. 5.5a. The non-patterned electrode on the top plate was connected to the electric ground potential. To switch the electric potential of the electrodes, the contact pads of the individual electrodes on the bottom plate were connected to the common terminal of the single pole double throw (SPDT) relays (LU-5, Rayex Electronics, Taiwan). The AC electric potentials were generated from two function generators (33210A, Agilent Technologies, USA) and they were amplified with two amplifiers (A-303 and A-304, A.A. Lab Systems, Israel). The relays were switched with the digital output

signals from a data acquisition device (USB-6509, National Instruments, USA) that was programmed with the software program LabVIEW. For the plasma separation, I simultaneously applied EWOD and particle/liquid DEP (PDEP/LDEP) forces (see 5.2.2 and Fig. 5.2). As shown in Fig. 5.5b, during the separation, a low-frequency voltage (V_{LF}) for EWOD was continuously supplied to the left larger reservoir electrode. By sequentially and selectively applying the high-frequency voltage (V_{HF}) for DEP to two to three blood cells remaining in the electrodes reservoir when high-frequency voltage was applied to the driving electrodes (1 mm × 1 mm) adjacent to the reservoir electrode, sufficient particle DEP/LDEP forces were generated to drive the plasma onto the driving electrodes and to retain the blood cells in the reservoir region. The application of EWOD on the reservoir electrode helps avoid the fast migration of the plasma on the driving electrodes. If EWOD is not applied, plasma separation is not induced. Occasionally, EWOD voltages needed to be tuned when the liquid was driven across the electrode gaps. For the separation of high-purity plasma droplets, tuning EWOD is an important operation to control the plasma migration on driving electrode while maintaining the whole blood on the reservoir electrode. Finally, by switching off a connecting driving electrode next to the terminal driving electrode with the purified plasma, a plasma droplet was created, as shown in Figs. 5.5b,c.

(a) (b)

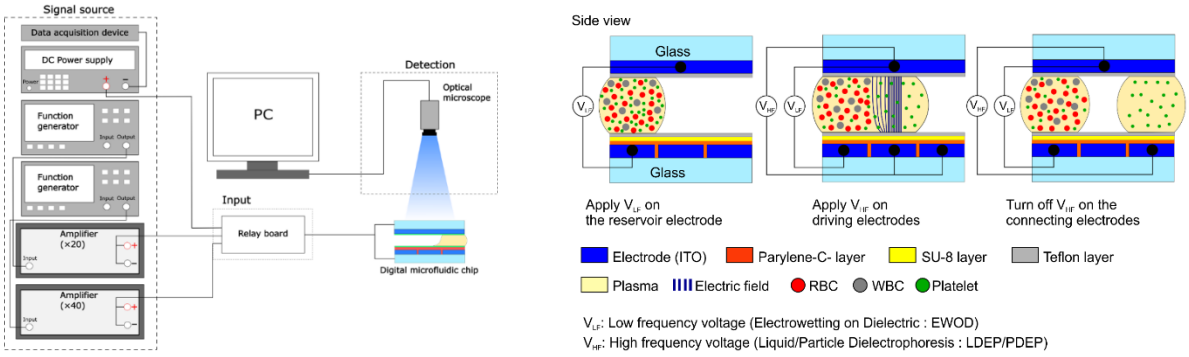

(c)

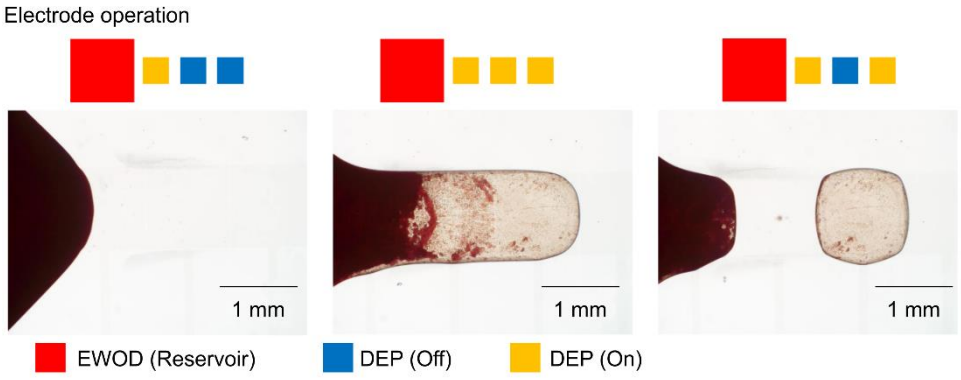

Figure 5.5 (a) Schematic of the setup of plasma separation on the DMF device with signals amplified for DEP (×20) and EWOD (×40) actuations. (b) Principle of plasma separation by EWOD/DEP. When the low-frequency EWOD voltage (V_{LF}) was applied to the reservoir electrode to hold the whole blood, the high-frequency DEP voltage (V_{HF}) was applied to several (three or four) driving electrodes to mainly drive the plasma and to retain the blood cells. After the separation, the DEP voltage was switched off of the connecting electrodes in order to split the droplet. (c) Photographs of the separation process with the DMF device (51.2 Vrms at 1.5 MHz). The gap height was 200 μm. The color squares showed the switch manipulation for the plasma separation, which is linked with the photographs. Most of the blood cells were maintained on the reservoir electrodes by the non-uniform electric field that was applied on the driving electrode to generate a plasma droplet.

5.2.4 Measuring the concentration of the blood cells

To investigate the separation ability, I measured the concentration of the blood cells, which includes red blood cells (RBCs), white blood cells (WBCs), and platelets in the original whole blood and the separated plasma droplet. The concentration of the blood cells was measured with three methods: a hematology analyzer (Sysmex XN-10 Hematology Analyzers, Sysmex, Japan), a hemocytometer (Counting chamber, Paul Marienfeld, Germany), and image analysis.

The hematology analyzer was mainly used to measure the original blood cell concentration of whole blood without dilution. It was also adopted to measure the concentration of the separated plasma. For the plasma measurements, I separated 10 plasma droplets (each volume was 0.2 μL) on a single DMF device (200 μm gap, 1.5 MHz, 51.2 Vrms) to obtain a total of 2 μL of plasma. The plasma was then diluted 100 times to 200 μL with PBS to meet the requirements of the hematology analyzer. The minimum sample volume required for measurement with the hematology analyzer is 200 μL. The hemocytometer was mainly used to measure the cell concentration of the plasma. The plasma droplet (each volume was 0.2 μL) that was separated with the DMF device (200 μm gap, 1.5 MHz, 51.2 Vrms) was diluted 100 times to 20 μL as the measured sample. The diluted plasma (20 μL) was loaded on the hemocytometer and the blood cells were counted with a microscope.

For the hematology analyzer, the concentration of the WBCs and RBCs in the diluted plasma was below the detection limit. I could only obtain the platelet concentration of the diluted plasma. For the hemocytometer and the image analysis, the platelets were too small for the microscope images. Assuming that my separation method has a low selectivity among the blood cell types and that it is based on the original concentrations of the RBCs (a few $\times 10^9$ cells/mL)[61] and WBCs (a few $\times 10^6$ cells/mL)[62] for the hundreds to thousands of blood cells that were analyzed, most cells that were observed with the hemocytometer and the image analysis were RBCs.

For the image analysis of the plasma, I used ImageJ software ver. 1.48 for cell counting and the procedures is as follows: After the generation of the plasma droplet, I captured the image of the plasma droplet at 6 parts with a 20-objective lens of a microscope (Olympus IX73 and DP71) as shown in Fig. 5.6. Next, I changed to the 8-bit version and treated the noise with "Despeckle." Then, the blood cells in the image were stained using "Threshold," and the image was processed to recognize all blood cells as independent cells. Finally, I counted the cell number with "Analyze Particles". In this study, I conducted the cell count six times for one plasma droplet using six-part images and the average cell concentration (C_{plasma}) was calculated to decide the separation efficiency. For the calculation, I either used the measured or literature value (5×10^9 cells/mL)[61] of the blood cell concentration in whole blood (C_{blood}). The separation efficiency η was calculated with the equation $\eta = (1 - C_{plasma}/C_{blood}) \times 100\%$. With the microscope resolution and concentration ratio between RBCs and WBCs, the measured cells were RBCs.

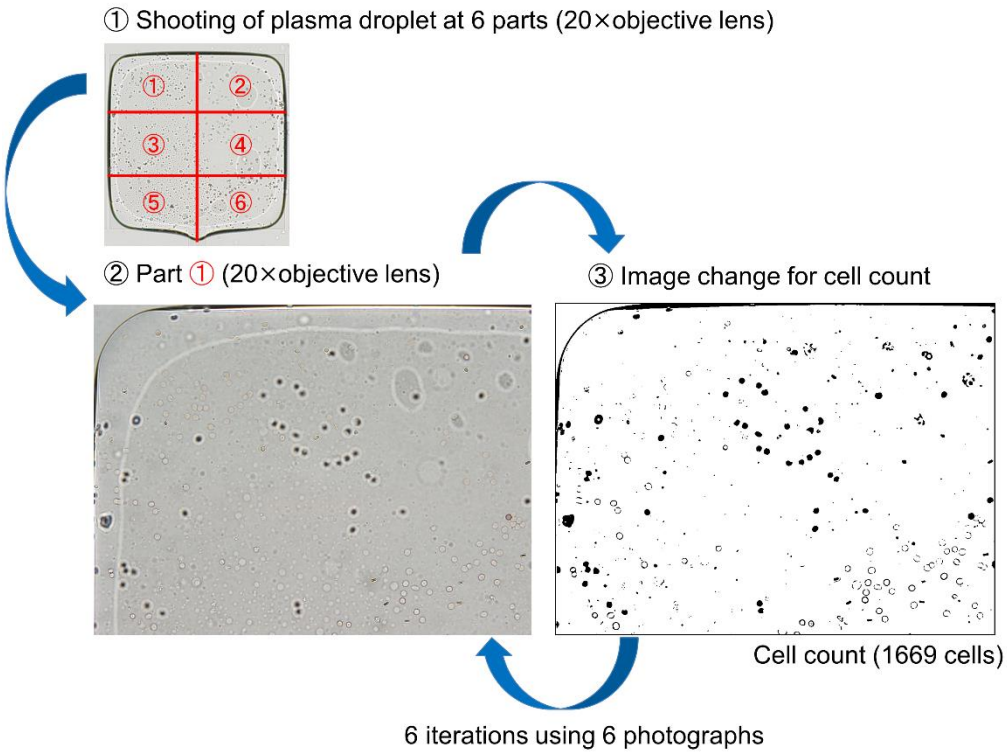

Fig. 5.6 Illustration of the cell counting procedure of blood cells using image analysis.

5.2.4 Image analysis for the PAD unit

First, the photograph of the paper sensors was taken with a digital camera (EOS Kiss X9, Canon, Japan; ISO, 1600, shutter speed, 1/100; aperture value, 5.6). The magenta intensity in each paper sensor (ROI, 17692 pixels) was obtained with ImageJ software after converting "RGB" to "CMYK" (see Fig. 5.7). The procedure was based on my previous study to maximize the measured color intensity from the image analyses of all of the samples.[60]

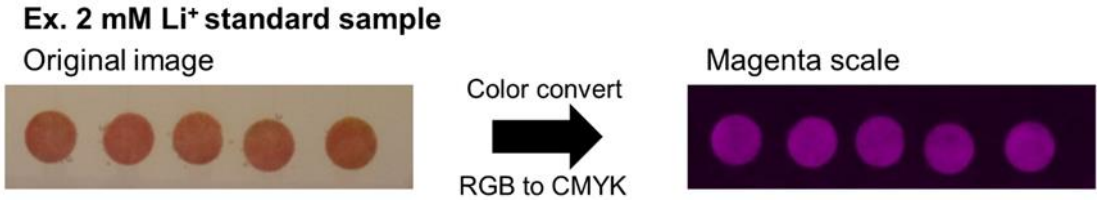

Fig. 5.7 Demonstration of image analysis with color conversion from RGB to CMYK.

5.2.5 Cell count and calculation of separation efficiency on serial separating plasma droplet

I calculated the concentration of blood cells in the whole blood on the reservoir against the volume of whole blood after the separation number of the plasma droplet. For example, the original concentration of blood cells (C_{oc}) in whole blood (5 μL) obtained by flow cytometry is used for the calculation of the separation efficiency of the first separated plasma droplet (0.2 μL). Next, the concentration of blood cells in the remaining whole blood (4.8 μL) on the reservoir (C_2) was calculated using the concentration of blood cells in first separated plasma droplet (C_1) using the cell count and original concentration as

$$C_2 = C_{oc} - C_1$$

After that, the concentration of blood cells in the remaining whole blood on the reservoir (C_2) was used for calculating the separation efficiency of the second separated plasma droplet. I repeated the above calculation process five times for calculating the separation efficiencies against the separated five plasma droplets. I note

that the concentrations of the blood cell in entire blood on the reservoir were calculated by the cell count was used for calculating the separation efficiencies of the image analysis and cell count.

5.2.6 Clarification of the importance of the plasma separation for determining the lithium-ion

To clarify the importance of the plasma separation for Li^+ detection, the blood or plasma droplet was divided with the DMF device (200-μm gap) and transported to paper sensors. Then, the image was obtained by the digital camera, and the magenta intensity was measured by image analysis.

5.3 Results and discussion

5.3.1 High-frequency voltage for blood cell separation

To examine the blood cell separation at high frequencies, I changed the frequency from 100 kHz to 2 MHz by referring to previous reports.[18, 19] Whole blood with 0.1% surfactant was loaded to one reservoir. A high-frequency DEP voltage ($70V_{pp}$) was applied to two or three driving electrodes besides the reservoir electrode to induce the driving of the plasma and to prevent the movement of the blood cells. Low-frequency EWOD voltage ($24–40V_{pp}$) was applied to the reservoir electrode simultaneously. 2 cSt silicone oil was used as an ambient liquid to fill the gap between the top and bottom plates. In this study, the gap, which was determined by spacers, was 200 μm to better accommodate the paper sensors. In the 100 to 900 kHz frequency range, the particle DEP force was not large enough to prevent the motion of the blood cells onto the driving electrodes. Instead, the liquid flow drove the blood cells toward the liquid boundaries and the corners of the driving electrodes; the plasma was not efficiently separated from the whole blood in this frequency range. On the contrary, most of the blood cells remained on the reservoir electrode when high-frequency voltages ranging from 1 to 2 MHz were applied on the driving electrodes (see Fig. 5.5c). However, some blood cells still migrated along the liquid boundaries from the driving electrodes in the flowing direction of the plasma, which decreased the separation efficiency. Owing to the force balance between the particle DEP force and Stokes'

drag force, reducing the flow rate can improve the separation efficiency and yield pure plasma. The separation efficiencies at 1.0, 1.5, and 2.0 MHz, calculated by image analysis, were 98.7 % with small standard deviations (< 0.3%) and are presented in Table 5.2. This was obtained using the image analysis method and value (5×10^9 cells/mL)[61] of RBC concentration in the whole blood reported in the literature. The present separation technique allows the separation of the pure plasma droplet from whole blood in less than 5 min.

Table 5.2 Separation efficiency for each frequency that was calculated by the image analysis (mean ± s.e.m., n = 3). The separation time was within 5 min in all experiments.

	Separation efficiency (%)	CV (%)	Applying voltage (Vrms)
1.0 MHz	98.7 ± 0.2	0.2	53.3
1.5 MHz	98.7 ± 0.3	0.3	51.2
2.0 MHz	98.7 ± 0.2	0.2	35.9

However, using high-frequency voltage is liable to triggering ruptures in the blood cells (hemolysis) due to the high temperature.[19] I measured the temperature during the separation process at 1.0, 1.5, and 2 MHz with a midwave infrared thermography camera (A6702sc, FLIR® Systems, USA). The measurement was repeatedly carried out in triplicate without sample change. The separation time was approximately 100 s, and the maximum temperature was less than 40 °C for all of the experiments with varied frequencies to obtain the plasma droplets. Note that the temperature generated owing to voltage application depends on the separation time. Therefore, choosing proper electric signals with a rapid separation procedure is beneficial to my separation technique. The heat generated during the separation process entails no significant deterioration or denaturing of the proteins in whole blood and plasma. From these results, I chose the frequency of 1.5 MHz for the plasma separation in the following studies.

I tested the plasma separation with different gaps, between 20 μm and 400 μm, at 1.5 MHz. The voltage required to generate a plasma droplet for all of the gaps was measured with an oscilloscope, and the

values were determined to be similar (Table 5.3). The time required for plasma separation decreased when the gap was increased, as shown in Fig. 5.8a. For all of the gap heights that were examined, the separation efficiency was greater than 90%, as demonstrated in Fig. 5.8b and Table 5.4. This was obtained by using the image analysis method and the value (5×10^9 cells/mL)[61] of RBC concentration in whole blood reported in the literature.

Table 5.3 Relationship between gap height and applied voltage (V_{rms}) of high/low frequency, 1.5 MHz/1 kHz. The results are corresponding to Fig. 5.8.

	Gap height (μm)					
	20	30	40	50	70	100
EWOD (Vrms)	26.9–38.7	26.9–38.7	26.9–38.7	26.9–38.7	19.7–38.7	19.7–38.7
LDEP (Vrms)	51.2–70.4	51.2–70.4	51.2–70.4	51.2–70.4	51.2–70.4	51.2

	Gap height (μm)				
	200	250	300	350	400
EWOD (Vrms)	23.0–38.7	15.6–38.7	15.6–56.0	15.6–56.0	7.92–56.0
LDEP (Vrms)	51.2	51.2	70.4	70.4	70.4

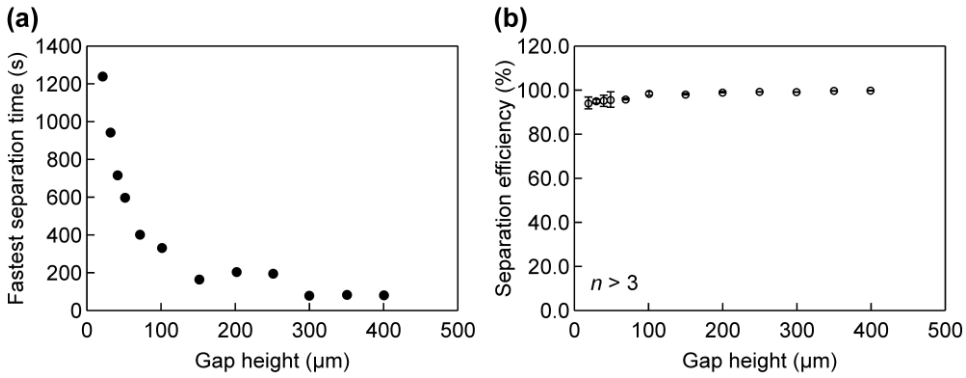

Fig. 5.8 Characteristics of the plasma separation with the 1.5 MHz DEP when using different gap heights that ranged from 20 μm to 400 μm. (a) The plots showed the fastest separation time with each gap height. In my separation technique, the decreasing trend of the separation time was confirmed with the increasing gap height. (b) The plots showed the separation efficiency with each gap height. A high separation efficiency (>90%) was achieved for all of the gap heights. The applied voltage for each gap height is described in Table 5.3.

Table 5.4 Separation efficiency (η) for each gap height in Fig. 5.8b that was calculated by the image analysis (mean ± s.e.m., n = 3).

	Gap height (μm)											
	20	30	40	50	70	100	150	200	250	300	350	400
η (%)	93.8±2.36	94.4±0.98	94.6±2.62	95.2±3.55	93.8±2.36	97.8±0.77	97.7±0.12	98.7±0.2	98.8±0.12	99.0±0.08	99.2±0.06	99.3±0.01
CV (%)	2.51	1.04	2.77	3.73	0.19	0.79	0.12	0.20	0.13	0.079	0.06	0.01

I further analyzed the separation efficiency with a gap of 200 μm for the fusion devices that contained the paper sensors. The separation efficiency was measured with a hematology analyzer, a hemocytometer, and via an image analysis. The hematology analyzer was applied to measure the original cell concentration in the whole blood and the platelet concentration in the diluted plasm droplets. Further, the hemocytometer and image analysis were adopted to measure the cell concentration in the diluted plasma droplets with the procedure described in the Methods section. In this experiment, the plasma was separated with a 51.2 Vrms and 1.5 MHz signal that was applied between the electrodes of the DMF device, which had a 200 μm gap. Table 5.5 shows

the summary of the cell concentrations obtained via the three methods. The hematology analyzer provided the cell concentration of the original whole blood as a reference for the separation efficiency. It also measured the plasma that was separated using the DMF device, but only the platelet concentrations (241×10^6 and 5×10^6 cells/mL) were measured; the concentrations of the WBCs and RBCs were below the detection limit. The hemocytometer and the image analysis provided blood cell concentrations of the plasma and the separation efficiency. The differences in the results obtained using the hemocytometer and image analysis were attributed to sampling and analyzing some of the blood cell aggregations in the plasma and the inability to obtain the number of cells along the height direction owing to the 2D nature of the images. The platelet separation efficiency determined from the hematology analyzer data was close to the image analysis results. This finding also shows that the separation was not specific to certain cell types. Note that the WBCs and platelets did not influence the assay color (yellow to red) because of their colorless characteristics.

Table 5.5 Comparison of the blood cell concentration using image analysis and conventional methods of hemocytometer and hematology analyzer. (Unit: cells/mL)

	Image analysis	Hemocytometer	Hematology analyzer	
	Plasma	Plasma	Plasma	Whole blood
WBC	-	-	-	5.1×10^6
RBC	7.39×10^7 (98.3%)*	2.25×10^8 (94.9%)*	-	4.15×10^9
Platelet	-	-	5.0×10^6 (98.0%)†	241×10^6
Total	-	-	-	4.396×10^9

()*: Separation efficiency over total cell concentration in whole blood

()†: Separation efficiency over platelet concentration in whole blood

5.3.2 Optimization of the PAD unit

For the detection of Li^+, I optimized the fabrication method of the paper sensor using a filter paper with a thickness that was the same as the gap height of the DMF device. The inspection of the Li^+ concentration in whole blood requires a 0–2 mM detection range.[50-54] My assay kit for Li^+ concentration indicates that the reaction ratio between the detection reagent (F28 tetraphenylporphyrin) and Li^+ is 1:1 mol. However, if an excessive amount of the detection reagent is concentrated on the filter paper, the background is high, and this is attributed to π-π binding.[60] To achieve the desired detection objective of up to 2 mM of Li^+, the paper sensors were designed to detect up to 3 mM of Li^+ with a 0.2 μL sample using the steps described in the Methods section. Based on my previous study [60], I concentrated a total of 350 μL of the detection reagent onto the filter paper (width: 4 cm, depth: 1 cm, thickness: 0.02 cm) considering calculations and the size of each paper sensor (diameter: 2 mm). I first tested the performance of the fusion device in the therapeutic drug monitoring range of 0.4 mM to 1.2 mM.[50-54] Each divided sample droplet (~0.2 μL) that contained standard samples with a specific concentration was loaded onto the embedded paper sensor in the DMF device, and the magenta intensity was measured via image analysis. The change in the contact angle owing to Li^+ is presented in Table 5.1. The color intensity that was obtained using the fusion device plateaued above 2.5 mM as shown in Fig. 5.9. The upper limit of the detection concentration expected based on the fabrication process of the paper sensors was 3 mM, and the obtained plot (Fig. 5.9) confirmed the concentration. The saturated concentration was slightly lower than the expected upper limit of detection because of the uneven size of the prepared filter paper, which is because scissors were used to prepare the filter paper.

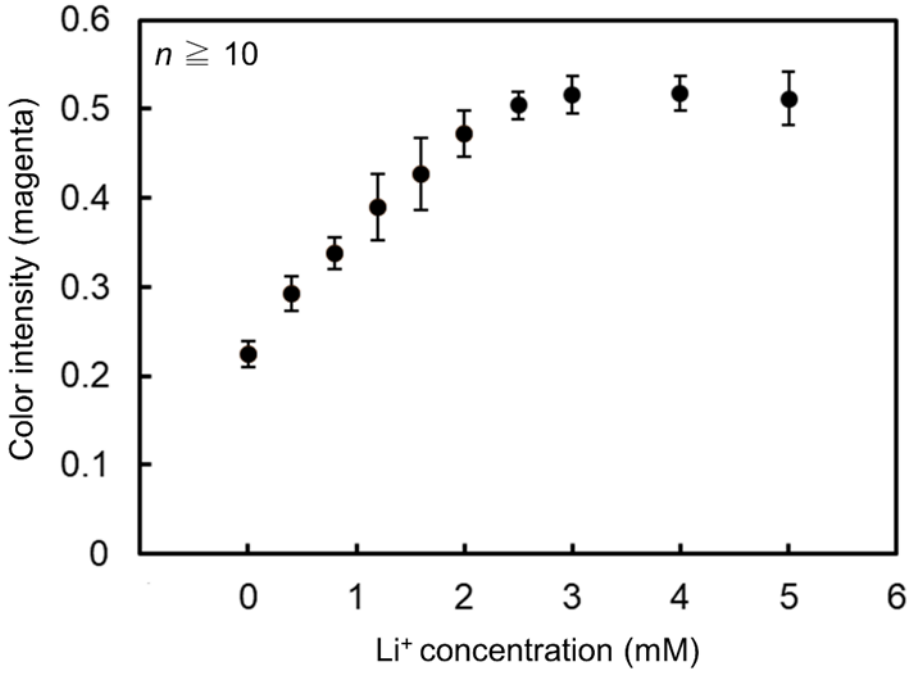

Fig. 5.9 Investigation of a saturation intensity using standard sample by my method. A linearity was obtained until 2.5 mM and the magenta intensity was saturated to 3 mM or more.

In addition, there was localization of the detection reagent during the drying process. Figures 5.10a,b and Table 5.6 show the colorimetric results that were obtained with the present method and a conventional method. The paper sensor color changed from yellow to red, and the color intensity increased with the increase in the concentration of Li^+. When comparing the detection ability, the present method was employed in accordance with the kit protocol: a standard sample solution and the detection reagent were mixed at a volume ratio of 1:60 in a well, and it was incubated at 37 °C for 10 min. The absorbance (λ = 546 nm) was measured with a microplate reader (SpectraMax i3x, Molecular Devices, Sunnyvale, CA, USA). The LOD (blank + 3σ) and the maximum coefficient of variance were 0.267 mM and 9.48%, respectively (Fig. 5.10b). Thus, the fabricated paper sensor showed sufficient detection ability for therapeutic drug monitoring in the concentration range of 0.4 to 1.2 mM.

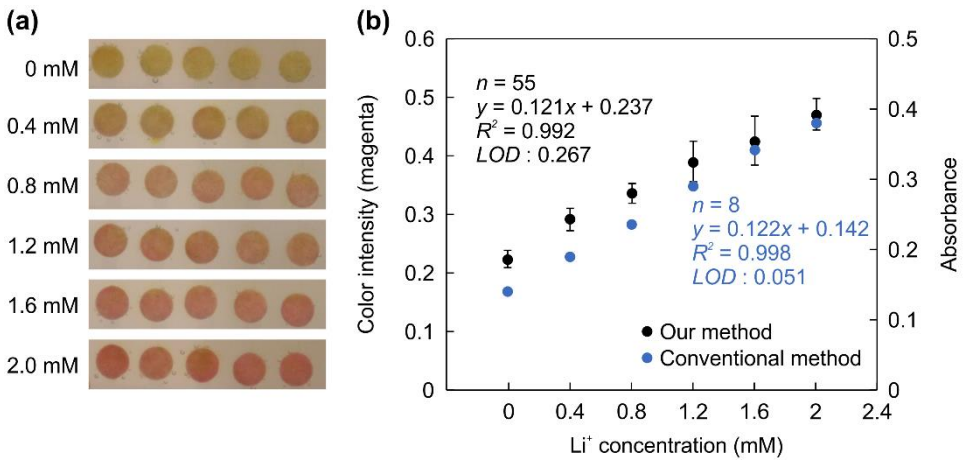

Table 5.10 Measurement of Li^+ in standard solutions for various concentrations that is based on my proposed method. (a) Photograph of the paper sensor after detecting Li^+ with my device. The color increased as the concentration of Li^+ increased. (b) Calibration curve with the proposed method and the conventional methods: black plot represents the proposed method, and the blue plot denotes the conventional method. The calibration curve that was obtained by my method displays good linearity and a high reproducibility in comparison to the conventional method according to the kit protocol.

Table 5.6 Measurement of Li^+ standard sample by my method/the conventional method (mean ± s.e.m.)

	This work's method (DMF-Paper sensor, n = 55)		Conventional method (Microplate reader, n = 8)	
Li^+ conc.	Color intensity	CV (%)	Absorbance	CV (%)
0 mM	0.225 ± 0.01	6.53	$0.141 \pm 2.4\times10^{-3}$	1.69
0.4 mM	0.293 ± 0.02	6.80	$0.191 \pm 4.8\times10^{-3}$	2.51
0.8 mM	0.337 ± 0.02	5.25	$0.237 \pm 3.6\times10^{-3}$	1.51
1.2 mM	0.390 ± 0.04	9.48	$0.292 \pm 4.5\times10^{-3}$	1.55
1.6 mM	0.427 ± 0.04	9.50	$0.343 \pm 4.6\times10^{-3}$	1.33
2.0 mM	0.472 ± 0.03	5.51	$0.381 \pm 5.9\times10^{-3}$	1.54

Further, I investigated the influence of the reaction time and silicone oil on the color intensity. Before assembling the top and bottom plates, 0.2 μL of the detection reagent was preloaded onto the pre-dried paper sensors to enhance their stiction on the bottom plate. A 2 mM Li^+ solution was immediately loaded onto the paper sensors after loading the silicone into the gap in the DMF device, and photos was captured at different times (0–10 min). As shown in Fig. 5.11a, the color intensity after the sample loading reached the maximum intensity within 30 s (the first data point), and it remained consistent within the range of standard deviation during the measuring period. This result indicated that Li^+ in the sample droplet immediately reacted with F28 tetraphenylporphyrin in the paper sensor and the Li^+-F28 tetraphenylporphyrin complex was retained in the cellulose fibers without being affected by the silicone oil environment. I further changed the loading time of the sample droplet to study the influence of the pre-loading immersion of the paper sensors in the silicone oil environment on the color intensity. The silicone oil was first dispensed into the gap of the DMF device to immerse the paper sensors for 5–60 min before loading the sample. The 2 mM Li^+ solution droplets were subsequently loaded onto the paper sensors after the time delay. Figure 5.11b shows the relationship between the color intensity and the pre-loading immersion time of the paper sensor. The color intensity had a constant value for pre-loading immersion up to 20 min, and it started to decrease subsequently. This is because the absorption of the silicone oil onto the paper sensors started to limit the absorption of the incoming samples. Therefore, in the following studies, all the DMF processes for the whole blood had to be completed within 20 min.

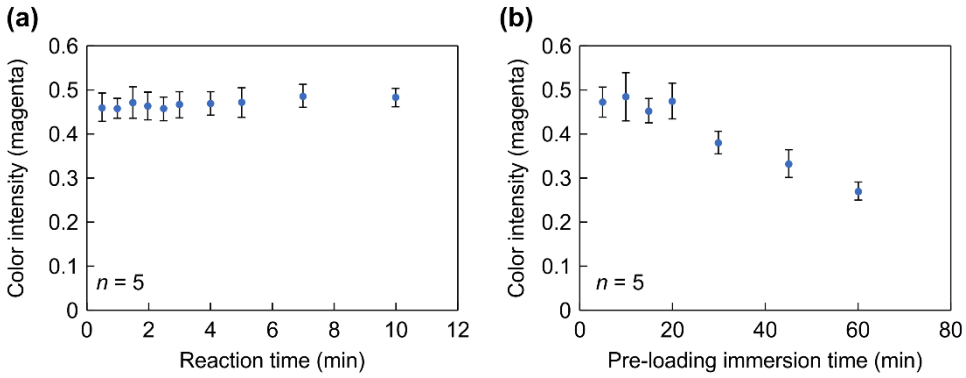

Figure 5.11 Influence of the silicone oil ambient on the paper sensor. Influence on the magenta intensity: (a) with time after loading the droplet of the 2 mM standard sample in the silicone oil ambient, (b) and with a different pre-loading immersion time in the silicone oil ambient that ranged from 5 min to 60 min before the sample loading. The paper sensor immediately reacted with Li^+ and it reached the maximum intensity. In addition, the intensity maintained a steady value for at least 10 min since there is no empty space in the paper sensors for the penetration of the silicone oil. However, the paper sensor before loading the 2 mM standard droplet sample was vulnerable to the silicone oil absorption after 20 min of the pre-loading immersion.

5.3.3 Analysis for detecting Li^+ in whole blood

I was able to determine the Li^+ concentration in whole blood with the proposed method. To compare the measurement ability, I separated the plasma from whole blood with Li^+ and 0.5% Pluronic® F-127 using a centrifuge. For this demonstration, I used the centrifuged separated plasma and the whole blood with Li^+/0.5% Pluronic® F-127. The changes in the contact angle for the standard sample, the plasma sample, and the whole blood with Li^+ are shown in Table 5.1. For the conventional method, 3 μL of the plasma that was separated with a centrifuge was mixed with 180 μL of the detection reagent. Afterwards, the absorbance (λ = 546 nm) was measured after incubation at 37 °C for 10 min in the microplate reader. For my method, 5 μL of plasma was separated with the centrifuge from the whole blood and 0.5% Pluronic® F-127 was introduced to the bottom plate's reservoir, in which five paper sensors were placed at the specified positions. The silicone oil was then introduced to the gap of the DMF device after assembling the top and bottom plates. I repeated the plasma

separation and paper sensor introduction five times within 20 min with a constant frequency of 1.5 MHz and voltage of 51.2 Vrms. The plasma sample measurement was carried out with the same procedure that was used for the standard samples (Fig. 5.10). To prove the reproducibility, I carried out intra-day and inter-day assays using varied whole bloods. The plasma droplet was separated from whole blood in the DMF device, and it was moved to the paper sensors as shown in Fig. 5.11.

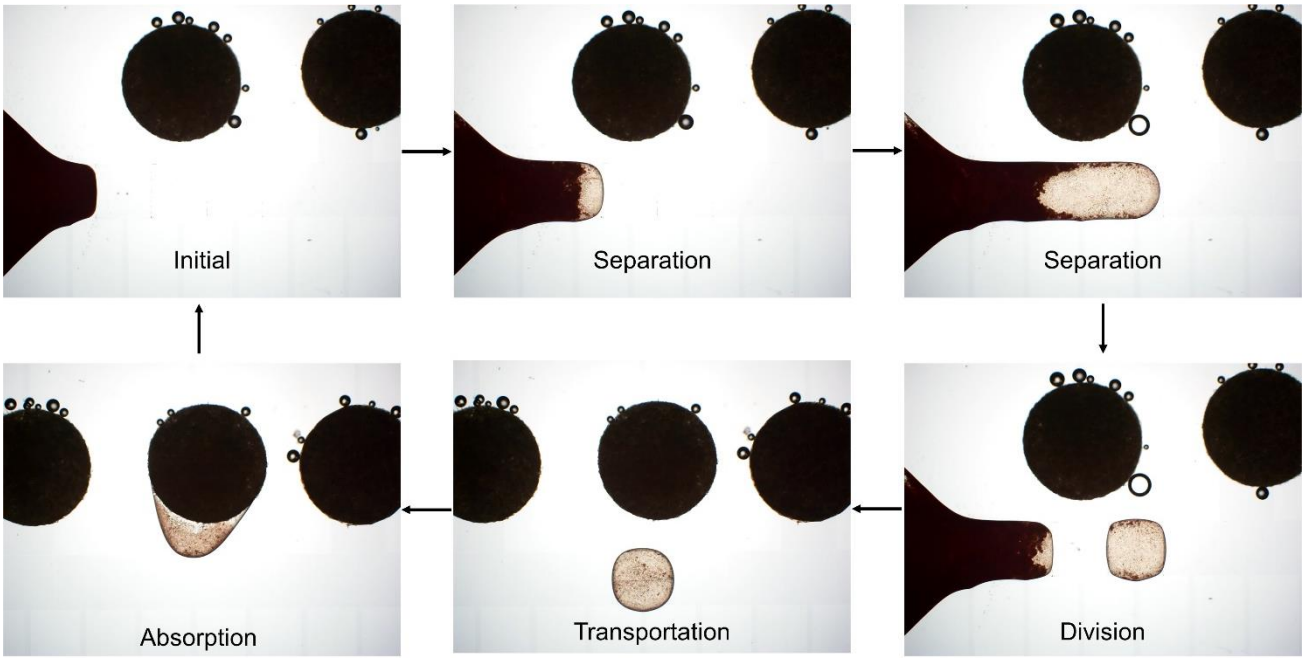

Fig. 5.11 Photograph of all of the processes for detecting Li^+ in whole blood with the fusion device.

In a single fusion device, five plasma droplets (total 1 μL) were separated in series from the same whole blood (original 5 μL) in the reservoir; thus, the blood cell concentration of the whole blood in the reservoir was expected to increase during the separation process. I considered the concentration increase in the reservoir and analyzed the cell concentration with a hematology analyzer (for the original whole blood), a hemocytometer, and image analysis, as shown in Table 5.7 and Figs. 5.12a,b. Figure 5.12a shows the images of the five plasma droplets separated from the same whole blood, and the number of blood cells in the separated plasma droplets increases according to the number of separations. Table 5.7 lists the blood cell concentration of the whole blood in the reservoir that was first measured by the hematology analyzer (data points for Plasma 1) and then

blood cell concentrations (Plasma 2 to 5) were calculated by considering the concentration of the previously separated plasma droplets. The measured blood cell concentration and the separation efficiency obtained from the hemocytometer and image analysis are presented in Table 5.7 and Fig. 5.12b. This was obtained by using the RBC concentration in the whole blood using the hematology analyzer. Although there is a variation in the measurement results between the hemocytometer and the image analysis, the results demonstrate that my method separated the plasma droplets with a high purity until five separations, in which 1/5 of the whole blood was consumed. The differences in the results obtained using the hemocytometer and image analysis were attributed to sampling and analyzing some of the blood cell aggregations in the plasma and the inability to obtain the number of cells along the height direction owing to the 2D nature of the images. To improve the quality of cell count using image analysis, I need to consider the dilution of the separated plasma droplet so that the cells exist individually or use the low thickness of the gap height for avoiding the lack of cell information in the height direction.

(a) (b)

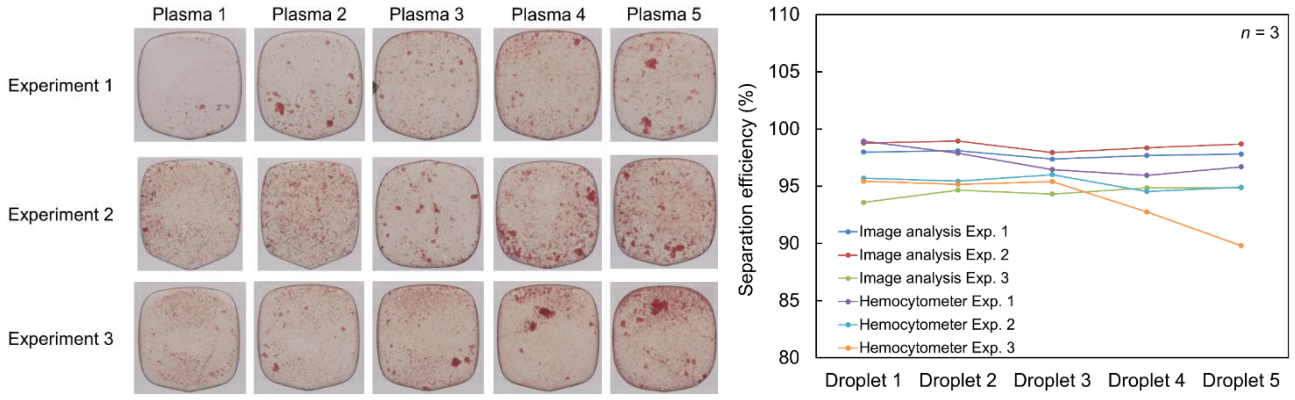

Fig. 5.12 (a) Photographs of separated droplets from whole blood on the reservoir. The experimental conditions were 1.5 MHz (51.2 Vrms) and 200 μm gap. The separation time was within 5 min for each separation. (b) Relationship between the separation efficiency of blood cells and separated plasma droplet from whole blood on the reservoir.

Table 5.7 Cell concentration and separation efficiency in each plasma droplet with five serial separations from whole blood (5 μL) in the reservoir (corresponding to Fig. 5.12). The experiments were repeated in triplicate. (Unit: $\times 10^7$ cells / mL)

	Image analysis			Hemocytometer			Hematology analyzer and calculation		
	Exp. 1	Exp. 2	Exp. 3	Exp. 1	Exp. 2	Exp. 3	Exp. 1	Exp. 2	Exp. 3
Plasma 1	9.15 (98.0%)*	5.56 (98.8%)	19.0 (93.6%)	4.80 (98.9%)	19.5 (95.7%)	13.5 (95.4%)	453	453	296
Plasma 2	8.97 (98.1%)	4.94 (99.0%)	16.4 (94.7%)	9.96 (97.9%)	21.5 (95.4%)	14.9 (95.2%)	472	471	308
Plasma 3	12.9 (97.4%)	10.1 (97.9%)	18.2 (94.3%)	17.4 (96.5%)	19.6 (96.0%)	14.7 (95.4%)	492	491	321
Plasma 4	11.9 (97.7%)	8.43 (98.4%)	17.1 (94.9%)	20.8 (95.9%)	28.0 (94.5%)	24.2 (92.8%)	513	512	334
Plasma 5	11.7 (97.8%)	7.00 (98.7%)	17.9 (94.9%)	17.7 (96.7%)	27.3 (94.9%)	35.5 (89.8%)	537	535	349

()*: Separation efficiency

Fig. 5.13a shows the photographs of the paper sensors after detecting Li^+ in the whole blood with the fusion device. The color intensity increased with an increase in the concentration of Li^+ in the whole blood as well as the standard sample. The plots corresponding to each experiment are displayed in Figs. 5.13b,c (and the summarized data in Table 5.8). For both demonstrations, all of the plots for each concentration of whole blood are in good agreement with those of the plasma obtained via the proposed method.

(a)

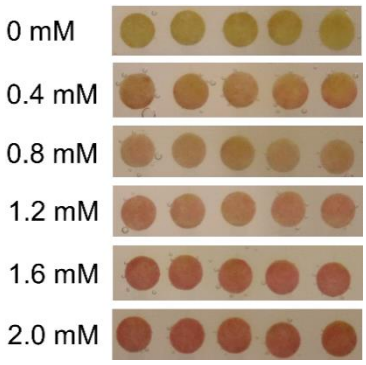

(b)

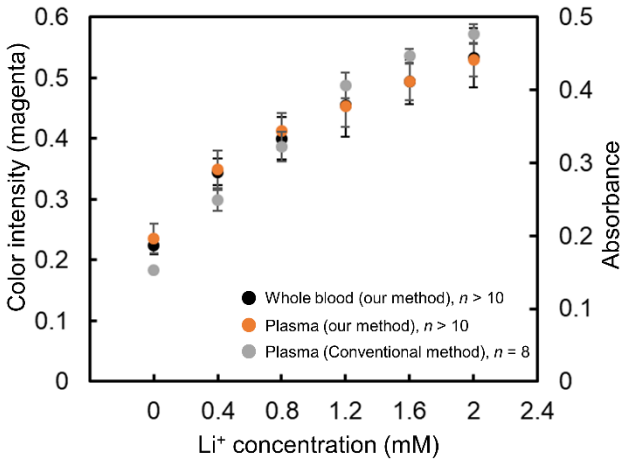

(c)

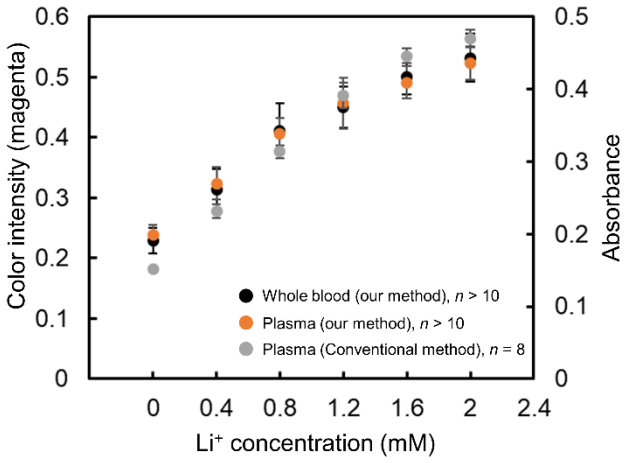

Fig. 5.13 Demonstration of the total analysis for determining the lithium-ion in whole blood (Movie S5). (a) Photograph after detecting Li^+ in whole blood. The color increased with an increase in the concentration of Li^+ in the whole blood without the influence of color from the blood cells. (b, c) The calibration plot when using the plasma/blood samples with my method and the conventional method (see Table 5.8). The plasma samples were prepared from the same blood sample by the centrifuge. The samples in (b) and (c) were prepared on a different day. The numbers of each trial are in the ascending order of Li^+ concentration; (b) n = 30, 35, 35, 20, 35, and 20 for plasma; n = 30, 15, 15, 15, 20, and 10 for blood; (c) n = 35, 20, 40, 40, 35, and 25 for plasma; n = 30, 35, 20, 10, 20, and 15 for blood. All plots for the proposed method are in good agreement with the plot that was obtained by the conventional method.

Table 5.8 Measurement of the Li^+ concentration in whole blood by my method and the conventional method related with Fig 5.13b, c (mean ± s.e.m.)

Fig. 5.13b	This work's method (Separated plasma)		This work's method (Whole blood)		Conventional method (Separated plasma, n = 8)	
Li^+ conc.	Color intensity	CV (%)	Color intensity	CV (%)	Absorbance	CV (%)
0 mM	0.235 ± 0.02	10.4	0.224 ± 0.02	6.70	0.153 ± 2.5 × 10^{-3}	1.65
0.4 mM	0.351 ± 0.03	9.36	0.345 ± 0.02	6.34	0.249 ± 1.4 × 10^{-2}	5.78
0.8 mM	0.409 ± 0.04	8.84	0.401 ± 0.04	8.74	0.332 ± 2.0 × 10^{-2}	6.14
1.2 mM	0.453 ± 0.03	7.52	0.456 ± 0.05	11.5	0.407 ± 1.7 × 10^{-2}	4.26
1.6 mM	0.494 ± 0.03	6.31	0.494 ± 0.04	7.46	0.446 ± 1.0 × 10^{-2}	2.32
2.0 mM	0.531 ± 0.03	5.21	0.533 ± 0.05	9.12	0.476 ± 1.4 × 10^{-2}	2.83
Fig. 5.13b	This work's method (Separated plasma)		This work's method (Whole blood)		Conventional method (Separated plasma, n = 8)	
Li^+ conc.	Color intensity	CV (%)	Color intensity	CV (%)	Absorbance	CV (%)
0 mM	0.239 ± 0.02	6.52	0.229 ± 0.02	8.92	0.152 ± 4.7 × 10^{-4}	0.312
0.4 mM	0.324 ± 0.03	8.27	0.313 ± 0.04	11.3	0.232 ± 9.5 × 10^{-3}	4.11
0.8 mM	0.406 ± 0.03	6.54	0.411 ± 0.05	11.1	0.314 ± 9.0 × 10^{-3}	2.85
1.2 mM	0.456 ± 0.04	9.19	0.451 ± 0.03	7.59	0.392 ± 1.8 × 10^{-2}	4.62
1.6 mM	0.491 ± 0.03	5.37	0.501 ± 0.03	6.00	0.446 ± 9.8 × 10^{-3}	2.21
2.0 mM	0.523 ± 0.03	5.18	0.532 ± 0.04	7.38	0.470 ± 1.2 × 10^{-2}	2.61

Although the blood cell concentration of the whole blood in the reservoir increased with the number of separation iterations in my method, the obtained results were close for the whole blood (black circles, separation

on-chip) and plasma (orange circles, separation with a centrifuge) samples. Fig. 5.14a and b illustrate the magenta intensity of the paper sensors with the whole blood and plasma samples. The left panels in Fig. 5.14a and b show the results obtained using the plasma samples separated with the centrifuge before loading the fusion device's reservoir, and the right panels display the results obtained using whole blood; note that Li^+/0.5% Pluronic® F-127 was employed in both cases. In all cases, the magenta intensity remained stable with respect to the serial separation of the plasma. The cause of the inconsistent intensity variation will be investigated subsequently. My future work will focus on improving the results obtained via the paper sensor, and these improved results could then be used for clinical diagnostic applications. The results indicate that the DMF device can offer a separation performance that is compatible with that of centrifugal separation without the influence of the concentration of the red blood cells in the reservoir.

(a)

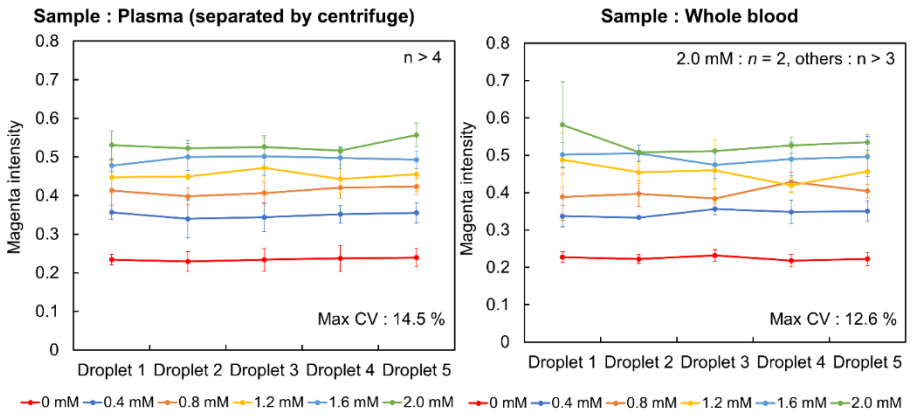

(b)

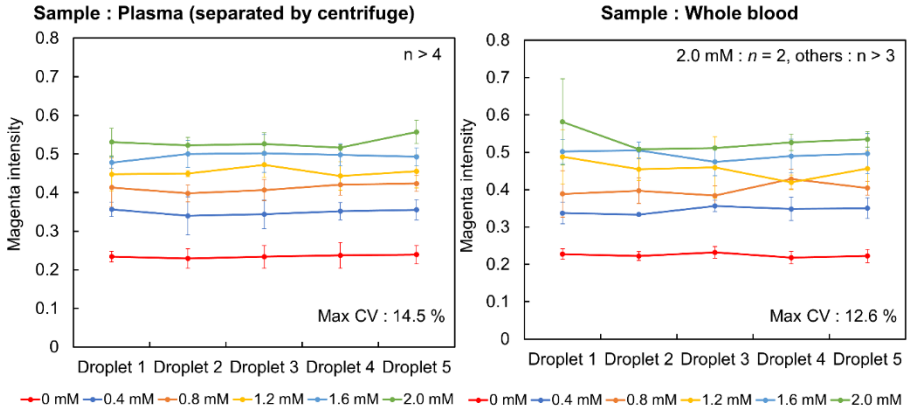

Fig. 5.14 (a, b) Investigation of the influence to the intensity with contentious separated plasma droplet from one reservoir. The left and right panels show the results using the plasma separated centrifuge and whole blood with lithium-ion/0.5% Pluronic® F-127, respectively. These experiments carried out the intra-day and inter-day assay using different whole blood.

The temperature during all of the processes for separating the five samples was monitored with midwave infrared thermography. The total time for separating the five samples ranged between 15 min and 18 min, and the highest recorded temperature was 39 °C. To clarify the importance of the plasma separation for identifying Li^+, I measured the magenta intensity without plasma separation using a 0 mM blood sample, as shown in Fig. 5.15. The magenta intensity was approximately 0.9, higher than that in all of the results obtained with plasma separation. Moreover, the variation coefficients in all of the demonstrated experiments were 11.5% or less.

This indicates that the present separation technique achieves a sufficient separation performance, and it can be applied in clinical practice for blood separations with a high efficiency rate and low cost. If only a data point of the Li^+ concentration in whole blood is required, the required time for detection can be reduced to 4 min or less.

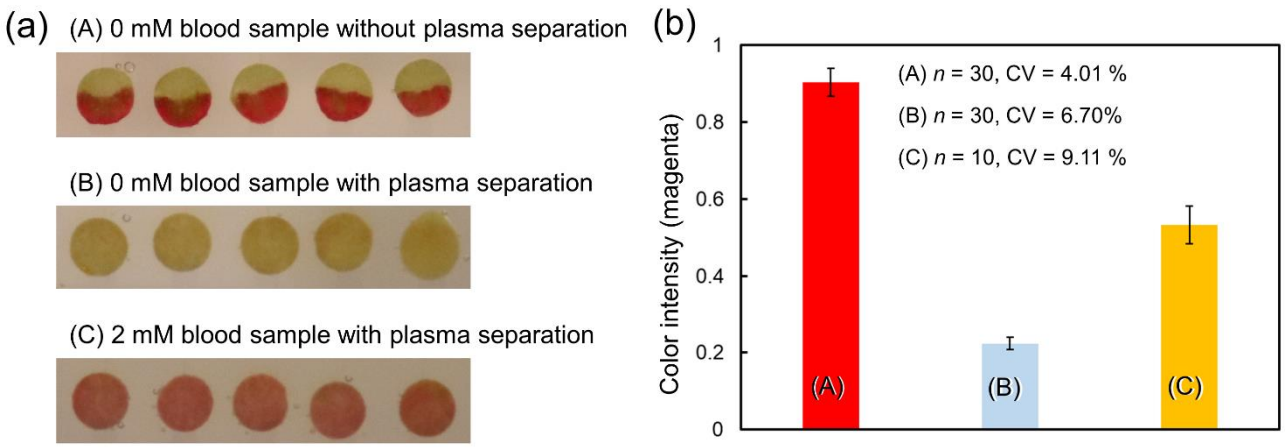

Fig. 5.15 Clarification of the importance of plasma separation for determining lithium-ion in whole blood. (a) Photography of paper sensors after loading blood or plasma droplet. The result of without plasma separation stained with the color of blood about the half of the paper sensor. I consider two reasons: paper sensors have a large area for wet over 0.2 μL-droplet. Second, the blood did not diffuse into the paper sensor because of the high viscosity. (b) The magenta intensity on each sample. The intensity of 0-mM blood sample without plasma separation was higher than that of with plasma separation. This result indicated that the concentration of lithium-ion cannot be measure without plasma separation.

5.4 Conclusions

In this study, a fusion device that employs DMF unit and PAD unit to determine the lithium ion concentration in whole blood was developed. By using DEP and EWOD, the plasma droplets with different volumes were separated from a few microliters of whole blood within a few minutes. Under the experimental

conditions of the fusion device (200 μm gap), the maximum temperature that was generated by the applied voltage was less than 39 ℃ for five serial plasma separations. Therefore, my separation technique can be applied for protein detection in whole blood and it can be extended to total analysis systems that have a digital microfluidic platform. The paper sensor, which contained the detection reagent, was integrated with the digital microfluidic platform, and a good performance for clinical applications was achieved with the colorimetric method. This is the first report on the application of colorimetry in a digital microfluidic platform. Nevertheless, the paper sensor was influenced by the typical ambient environment in the digital microfluidic platform—silicone oil. In contrast with the conventional method, my fusion device employed a low sample volume (5 μL) and achieved rapid detection within 4 min. The measurement performance was in good agreement with that of the conventional method; however, there is room for improvement in order to apply it to clinical diagnoses. According to these results, I succeeded in the development of fusion device for determining blood lithium ion concentrations. Finally, I believe that my fusion device can determine the concentrations of other components/multiple-targets in whole blood, and this can be achieved by preparing different paper sensors.

5.5 Reference

[1] C. H. Liu, C. A. Chen, S. J. Chen, T. T. Tsai, C. C. Chu, C. C. Chang, and C. F. Chen, *Anal. Chem.*, **91**, 1247-1253 (2019).

[2] S. Vemulapati, and D. Erickson, *Anal. Chem.*, **91**, 14824-14828 (2019).

[3] C. Dixon, J. Lamanna, and A. R. Wheeler, *Lab. Chip*, **20**, 1845-1855 (2020).

[4] Z. T. F. Yu, K. M. A. Yong, and J. P. Fu, *Small*, **10**, 1687-1703 (2014).

[5] M. Kersaudy-Kerhoas, and E. Sollier, *Lab. Chip*, **13**, 3323-3346 (2013).

[6] M. Rafeie, J. Zhang, M. Asadnia, W. H. Li, and M. E. Warkiani, *Lab. Chip*, **16**, 2791-2802 (2016).

[7] S. Haeberle, T. Brenner, R. Zengerle, and J. Ducree, *Lab on a Chip*, **6**, 776-781 (2006).

[8] T. H. Kim, M. Lim, J. Park, J. M. Oh, H. Kim, H. Jeong, S. J. Lee, H. C. Park, S. Jung, B. C. Kim, K. Lee, M. H. Kim, D. Y. Park, G. H. Kim, and Y. K. Cho, *Anal. Chem.*, **89**, 1155-1162 (2017).

[9] V. VanDelinder, and A. Groisman, *Anal. Chem.*, **78**, 3765-3771 (2006).

[10] T. Tachi, N. Kaji, M. Tokeshi, and Y. Baba, *Anal. Chem.*, **81**, 3194-3198 (2009).

[11] E. C. Yeh, C. C. Fu, L. Hu, R. Thakur, J. Feng, and L. P. Lee, *Sci. Adv.*, **3**, e1501645, (2017).

[12] X. X. Yang, O. Forouzan, T. P. Brown, and S. S. Shevkoplyas, *Lab. Chip*, **12**, 274-280 (2012).

[13] T. Songjaroen, W. Dungchai, O. Chailapakul, C. S. Henry, and W. Laiwattanapaisal, *Lab. Chip*, **12**, 3392-3398 (2012).

[14] A. Nilghaz, and W. Shen, *RSC Adv.*, **5**, 53172-53179 (2015).

[15] K. K. Lee, and C. H. Ahn, *Lab. Chip*, **13**, 3261-3267 (2013).

[16] C. C. Chen, P. H. Lin, and C. K. Chung, *Lab. Chip*, **14**, 1996-2001 (2014).

[17] S. Yan, J. Zhang, G. Alici, H. P. Du, Y. G. Zhu, and W. H. Li, *Lab. Chip*, **14**, 2993-3003 (2014).

[18] U. Lei, C. W. Huang, J. Chen, C. Y. Yang, Y. J. Lo, A. Wo, C. F. Chen, and T. W. Fung, *Lab. Chip*, **9**, 1349-1356 (2009).

[19] S. H. Liao, C. Y. Chang, and H. C. Chang, *Biomicrofluidics*, **7**, 024110 (2013).

[20] P. C. Chen, C. C. Chen, and K. C. Young, *Biomicrofluidics*, **10**, 054112 (2016).

[21] A. Kalantarifard, A. Saateh, and C. Elbuken, *Chemosensors*, **6**, 23 (2018).

[22] J. S. Barea, J. Lee, and D. K. Kang, *Micromachines*, **10**, 412 (2019).

[23] S. K. Cho, H. J. Moon, and C. J. Kim, *J. Microelectromech. Syst*., **12**, 70-80 (2003).

[24] K. Choi, A. H. C. Ng, R. Fobel, and A. R. Wheeler, *Annu. Rev. Anal. Chem.*, **5**, 413-440 (2012).

[25] J. Gong, and C. J. Kim, *Lab. Chip*, **8**, 898-906 (2008).

[26] S. Kalsi, M. Valiadi, M. N. Tsaloglou, L. Parry-Jones, A. Jacobs, R. Watson, C. Turner, R. Amos, B. Hadwen, J. Buse, C. Brown, M. Sutton, and H. Morgan, *Lab. Chip*, **15**, 3065-3075 (2015).

[27] L. Malic, D. Brassard, T. Veres, and M. Tabrizian, *Lab. Chip*, **10**, 418-431 (2010).

[28] H. Norian, R. M. Field, I. Kymissis, and K. L. Shepard, *Lab. Chip*, **14**, 4076-4084 (2014).

[29] S. K. Fan, P. W. Huang, T. T. Wang, and Y. H. Peng, *Lab. Chip*, **8**, 1325-1331 (2008).

[30] S. K. Fan, W. J. Chen, T. H. Lin, T. T. Wang, and Y. C. Lin, *Lab. Chip*, **9**, 1590-1595 (2009).

[31] S. K. Fan, T. H. Hsieh, and D. Y. Lin, *Lab. Chip*, **9**, 1236-1242 (2009).

[32] S. K. Fan, Y. W. Hsu, and C. H. Chen, *Lab. Chip*, **11**, 2500-2508 (2011).

[33] M. Y. Chiang, Y. W. Hsu, H. Y. Hsieh, S. Y. Chen, and S. K. Fan, *Sci. Adv.*, **2**, e1600964 (2016).

[34] S. K. Fan, H. P. Lee, C. C. Chien, Y. W. Lu, Y. Chiu, and F. Y. Lin, *Lab. Chip*, **16**, 847-854 (2016).

[35] X. Y. Zeng, K. D. Zhang, J. Pan, G. P. Chen, A. Q. Liu, S. K. Fan, and J. Zhou, *Lab. Chip*, **13**, 2714-2720 (2013).

[36] S. Abdulwahab, A. H. C. Ng, M. D. Chamberlain, H. Ahmado, L. A. Behan, H. Gomaa, R. F. Casper, and A. R. Wheeler, *Lab. Chip*, **17**, 1594-1602 (2017).

[37] D. G. Rackus, R. P. S. de Campos, C. Chan, M. M. Karcz, B. Seale, T. Narahari, C. Dixon, M. D. Chamberlain, and A. R. Wheeler, *Lab. Chip*, **17**, 2272-2280 (2017).

[38] M. C. Husser, P. Q. N. Vo, H. Sinha, F. Ahmadi, and S. C. C. Shih, *ACS Synth. Biol.*, **7**, 933-944 (2018).

[39] J. J. Guo, L. Lin, K. F. Zhao, Y. L. Song, M. J. Huang, Z. Zhu, L. J. Zhou, and C. Y. Yang, *Lab. Chip*, **20**, 1577-1585 (2020).

[40] M. D. M. Dryden, D. D. G. Rackus, M. H. Shamsi, and A. R. Wheeler, *Anal. Chem.*, **85**, 8809-8816 (2013).

[41] D. G. Rackus, M. D. M. Dryden, J. Lamanna, A. Zaragoza, B. Lam, S. O. Kelley, and A. R. Wheeler, *Lab. Chip*, **15**, 3776-3784 (2015).

[42] R. P. S. de Campos, D. G. Rackus, R. Shih, C. Zhao, X. Y. Liu, and A. R. Wheeler, *Anal. Chem.*, **91**, 2506-2515 (2019).

[43] A. H. C. Ng, R. Fobel, C. Fobel, J. Lamanna, D. G. Rackus, A. Summers, C. Dixon, M. D. M. Dryden, C. Lam, M. Ho, N. S. Mufti, V. Lee, M. A. M. Asri, E. A. Sykes, M. D. Chamberlain, R. Joseph, M. Ope, H. M. Scobie, A. Knipes, P. A. Rota, N. Marano, P. M. Chege, M. Njuguna, R. Nzunza, N. Kisangau, J. Kiogora, M. Karuingi, J. W. Burton, P. Borus, E. Lam, and A. R. Wheeler, *Sci. Transl. Med.*, **10**, eaar6076 (2018).

[44] A. K. Yetisen, M. S. Akram, and C. R. Lowe, *Lab. Chip*, **13**, 2210-2251 (2013).

[45] J. Hu, S. Q. Wang, L. Wang, F. Li, B. Pingguan-Murphy, T. J. Lu, and F. Xu, *Biosens. Bioelectron.*, **54**, 585-597 (2014).

[46] K. Yamada, H. Shibata, K. Suzuki, and D. Citterio, *Lab. Chip*, **17**, 1206-1249 (2017).

[47] Y. Yang, E. Noviana, M. P. Nguyen, B. J. Geiss, D. S. Dandy, and C. S. Henry, *Anal. Chem.*, **89**, 71-91 (2017).

[48] E. A. Youngstrom, *Clin. Psychol. Sci Pract.*, **16**, 140-160 (2009).

[49] E. Severus, N. Kleindienst, F. Seemuller, S. Frangou, H. J. Moller, and W. Greil, *Bipolar Disord.*, **9**, 96-96 (2007).

[50] A. Coppen, M. Abousaleh, P. Milln, J. Bailey, and K. Wood, *J. Affective Disord.*, **5**, 353-362 (1983).

[51] A. J. Gelenberg, J. M. Kane, M. B. Keller, P. Lavori, J. F. Rosenbaum, K. Cole, and J. Lavelle, *New England J. Med.*, **321**, 1489-1493 (1989).

[52] W. Greil, W. LudwigMayerhofer, N. Erazo, C. Schochlin, S. Schmidt, R. R. Engel, A. Czernik, H. Giedke, B. MullerOerlinghausen, M. Osteheider, G. A. E. Rudolf, H. Sauer, J. Tegeler, and T. Wetterling, *J. Affective Disord.*, **43**, 151-161 (1997).

[53] R. H. Perlis, G. S. Sachs, B. Lafer, M. W. Otto, S. V. Faraone, J. M. Kane, and J. F. Rosenbaum, *Am. J. Psychiatry*, **159**, 1155-1159 (2002).

[54] J. Baird-Gunning, T. Lea-Henry, L. C. G. Hoegberg, S. Gosselin, and D. M. Roberts, *J. Intensive Care Med.*, **32**, 249-263 (2017).

[55] W. M. Glazer, J. G. Sonnenberg, M. J. Reinstein, and R. F. Akers, *J. Clin. Psychiatry*, **65**, 652-655 (2004).

[56] E. X. Vrouwe, R. Luttge, W. Olthuis, and A. van den Berg, **26**, 3032-3042 (2005).

[57] E. X. Vrouwe, R. Luttge, I. Vermes, and A. van den Berg, *Clin. Chem.*, **53**, 117-123 (2007).

[58] A. Floris, S. Staal, S. Lenk, E. Staijen, D. Kohlheyer, J. Eijkel, and A. van den Berg, *Lab. Chip*, **10**, 1799-1806 (2010).

[59] M. Novell, T. Guinovart, P. Blondeau, F. X. Rius, and F. J. Andrade, *Lab. Chip*, **14**, 1308-1314 (2014).

[60] T. Komatsu, M. Maeki, A. Ishida, H. Tani, and M. Tokeshi, *ACS Sens.*, **5**, 1287-1294 (2020).

[61] P. C. Chen, F. C. Sung, K. L. Chien, H. C. Hsu, T. C. Su, and Y. T. Lee, *Am. J. Epidemiol.*, **171**, 214-220 (2010).

[62] H. V. Barron, C. P. Cannon, S. A. Murphy, E. Braunwald, and C. M. Gibson, *Circulation*, **102**, 2329-2334 (2000)

CHAPTER 6 Conclusion and Future Prospects

Conclusions

In this thesis, the main objective was the development of a paper-based analytical device (PAD) for low-cost, rapid, and straightforward measurement of components in human blood via colorimetry. The problems of paper-based analytical devices toward blood tests include a selection of the best fabrication methods of PADs, image analysis methods for detecting multi-analytes in the whole blood, achieving plasma separation, and accurate volume control of the separated plasma. To overcome these problems of conventional PADs toward blood tests, the fabrication and image analysis methods were first evaluated as the basic study. Subsequently, I developed a PAD and fusion device for determining the lithium ion concentration in human blood as a model target. The summary of each chapter is described below.

In chapter 2, a common PAD design was fabricated by four common methods, including craft cutting, wax printing, screen printing, and photolithography, and revealed the characteristics of each device, such as economic efficiency, fabrication accuracy, wicking rate, and influence on the measurement performance by colorimetry. This is because the selection of the best PAD fabrication method is required but there is no information concerning which is best. As a result, each fabrication method provides high-cost performance; however, the ease of fabrication and fabrication accuracy differ in these methods. Additionally, PADs that are fabricated by employing different fabrication process and hydrophobic materials for patterning have different characteristics of wicking rate and affect the color development and measurement performance. This study offers supporting information to researchers for the development of PADs. According to the results obtained in this study, I concluded cutting and screen printing are better for developing colorimetric PAD.

In Chapter 3, I considered the image analysis method with CIE $L^*a^*b^*$ color system for achieving multi-color detection on the PAD. As a model of multi-color changes, pH detection (pH 2–9) with a universal pH indicator was demonstrated using the PAD with the typical design and quantitative analysis by image analysis via the CIE $L^*a^*b^*$ color system. When measured by image analysis via a single color scale (Red, Green, Blue), the Red, Green, Blue, and Gray intensities did not exhibit a good relationship between pH as RGB analysis obtains single-color information. In contrast, the CIE $L^*a^*b^*$ color system has three coordinates, i.e.,

L^*, a^*, and b^*. The L* value indicates lightness and $(a^* + b^*)^{1/2}$ and $\tan^{-1}(b^*/a^*)$ indicate chroma (C_{ab}) and hue angle (h_{ab}), respectively. Based on L^*, a^*, and b^* values, the color difference (ΔE) between an objective color (pH 3–9) and a reference color (pH 2) demonstrated that the ΔE value increased monotonously with increasing pH value, with small standard deviations. Additionally, a wide detectable pH range and high reproducibility were achieved and, when compared to results obtained via the RGB-based image analysis, the single-channel value of L^*, a^*, and b^*, and $\tan^{-1}(b^*/a^*)$ contains the hue information, as well as ΔE. Therefore, I succeeded in the pH measurement by image analysis method with the CIE $L^*a^*b^*$ color system. This image analysis method is expected to be applied to the quantitative analysis of multiple components in whole blood.

In Chapter 4, a PAD for determining the lithium ions in human blood was developed for application to blood tests. Lithium carbonate is widely used as a medicine in bipolar disorder therapy; however, regular monitoring of the lithium-ion concentration in blood is required for proper treatment. To overcome the drawbacks of using conventional PADs in blood tests, this PAD was designed and composed of separation assisting polymer substrates and two inter-linked paper-based elements: a blood cell separation unit and a colorimetric detection unit that concentrated F28 tetraphenyl porphyrins as the detection reagent. After a portion of the entire blood has been applied to the end of the separation unit, plasma in the sample is automatically transported to the detection unit, which is then displayed as a diagnostic color. The key feature of this PAD is its simple and user-friendly operation. The LOD is 0.054 mM and the coefficient of variance is below 6.1 %, which are comparable to those of conventional instruments using the same colorimetric reaction. Furthermore, I achieved a high recovery (> 90 %) and reproducibility (< 9.8 %) with spiked human blood samples. Thus, the presented device provides an alternative method for the regular monitoring of lithium concentrations in the treatment of bipolar disorder by augmenting the coefficient of variation (maximum value, 6.1 %). According to the results obtained in this study, I succeeded in developing a PAD for determining the lithium-ion concentration in human blood.

In Chapter 5, a fusion device for determining lithium ions in human whole blood was developed by combining digital microfluidics (DMF) and the paper-based device. The developed PAD in Chapter 4 still

requires the improvements: (i) more reduction of required blood volume and (ii) non-requirement of the blood introduction of a certain volume. To achieve (i) and (ii), I invented a fusion device comprised of a DMF unit and five circle paper-based devices, PAD unit. The DMF unit was used for the pretreatment procedure, including plasma separation, dividing an accurate volume of the plasma droplet, transporting the plasma droplet, and introducing the plasma droplet to the PAD unit. For plasma separation with DMF, EWOD and DEP are simultaneously performed on the DMF platform. A high-frequency voltage (above 1 MHz) induced the plasma separation by dielectrophoresis and the required time of the plasma separation was from 1 to 5 min while generating a temperature lower than 40 °C. Additionally, this separation method can accurately separate different volumes of the plasma droplet (20–400 nL) to form a few microliters of whole blood with a separation efficiency greater than 90 % using different gap heights (20–400 μm). For Li^+ detection, the PAD unit was fabricated by drying and concentrating the detection reagent (F28 tetraphenylporphyrin) on a filter paper, based on my previous study (Chapter 4). In a proof-of-concept study, as expected, the fusion device achieved the required measurement performance for the lithium ion test in ambient silicone oil. The LOD was 0.267 mM and the coefficients of variation (CVs) in the measuring range were less than 9.5 %. To determine the lithium ion concentration in whole blood, the developed fusion device completed five serial replications within 20 min while maintaining a generated temperature lower than 39 °C. The data plots obtained by the device presented herein are in good agreement with those obtained via a conventional method when the corresponding kit protocol is used. This indicates that the developed fusion device can be a potent therapeutic tool for rapidly detecting lithium ions in whole blood. According to these obtained results, I succeeded in the development of the fusion device for determining lithium ions in human blood, addressing the drawbacks of the developed PAD in Chapter 4.

In conclusion of this thesis, I developed novel techniques for overcoming the problems of using conventional PADs in blood tests.

Future prospects

Paper-based analytical devices (PADs) show great potential as an alternative method of blood testing owing to their low-cost, biocompatibility, and portability (see Fig. 1.16). Generally, blood tests require the separation of plasma or serum from the whole blood. In addition, accurately controlling the volume of serum or plasma is essential manipulation for quantitative analysis of a target concentration by blood tests as the regulation of blood tests is defined by the amount of substance per unit volume of the serum or plasma. Therefore, PADs for blood tests should be integrated with separation and pipette manipulation (conducted by a trained person) to provide a user-friendly, reliable, and on-site analysis at any location. The PAD for determining the lithium ion concentration in whole blood was developed for use in blood tests. This device can detect lithium ion in whole blood by two-steps: introduction of whole blood and pressing the detection unit to the separation unit. This method controls the plasma volume by using a determined detection area (hydrophilicity) to absorb the plasma. However, micro-pipetting is still required for loading the whole blood (10–20 μL). Therefore, the relationship between color intensity and blood volume lower than 10 μL was investigated and developed for the smartphone application of image analysis and to achieve user-friendly and on-site analysis. Moreover, to prevent biohazards from users, the paper-based device should be embedded into an optimized container. Most importantly, my device design has overcome the problems of PADs toward blood tests and can contribute to the development of PADs for detecting a single analyte or multi-analytes in human blood to achieve on-site analysis.

As other approaches for blood tests with the PAD, the fusion device consists of a DMF unit and the PAD unit for determination of lithium ion in human whole blood was developed. This device achieved automatic determination of lithium ions in whole blood, integrated with plasma separation, accurate volume division of the separated plasma into droplets, transportation of a plasma droplet, and introduction of the plasma droplet to the paper-based device for lithium ion detection. Moreover, the advantage of this device is that it only requires a low blood volume (5 μL), five simultaneous detections within 20 min, and a low generated temperature (< 39 °C). Thus, my fusion device has the potential for determining multiple components in whole

blood by embedding several paper sensors, which are retained different detection reagents. Furthermore, my electrode design of a DMF device can be easily parallelized and resized for achieving a high-throughput. By combining the image analysis method described in Chapter 3, I will, in the future, present an automatic analytical system for determining multiple components in whole blood. In this thesis, I could not demonstrate the detection of multi-analytes in whole blood. However, the PAD unit is embedded into the DMF unit; hence, a cartridge-type fusion device that can be inserted into the PAD unit from outside is preferred for improved versatility. More importantly, the DMF that can quickly separate the plasma of the accurate volume from low blood volume (< a few microliters) will allow application to the detection of various targets in human blood as it is easy to parallelize the electrodes constructed in the DMF. With the freedom to choose liquid-based chemical detection, this technology has the potential to enable multi-target simultaneous quantification of blood components in the future. To achieve further developed automatic systems, the external instrument, including the supply of voltages to electrodes of DMF, storage tanks of the liquid sample (reagents and washing buffer), and measurement parts (such as optical parts and analysis algorithms), should be used for an on-site analysis in developing countries.

Figure 6.1 illustrates the future prospects of the PADs. The demand for on-site analysis of medical tests is raised in many situations, such as not only common blood tests but also a home-based test and emergency inspection in disasters and emergency medicine. For example, the blood collected from a child's finger is (at the most) a few microliters; hence, there is a strong need to develop novel analytical methods in pediatric care that can be conducted using very low blood volume to minimize invasive diagnostics. Moreover, home-based tests and emergency inspections, e.g., when a natural disaster occurs, have some requirements, such as low-cost, minimally invasive, rapid detection, user-friendless, and portability. The PADs can provide medical test tools that meet these needs owing to the advantages described in the General Introduction. The developed prototype in this thesis can support academic research of PADs for blood tests and also other medical tests, including device design and performance evaluation. After developing end-user PADs for medical tests, the PADs will be commercialized through industry-academia collaboration. Finally, through the realization of a society

where anyone can easily perform medical tests (e.g., in the home, working place, or ill-equipped locations, such as developing countries or in the case of natural disasters), it will be possible to make a significant contribution to the medical field. Furthermore, the PADs can contribute to realizing Society 5.0 for telemedicine and an improvement of quality-of-life with on-site medical tests by combining the technologies of novel diagnostic systems related to the Internet-of-Things (IoT).

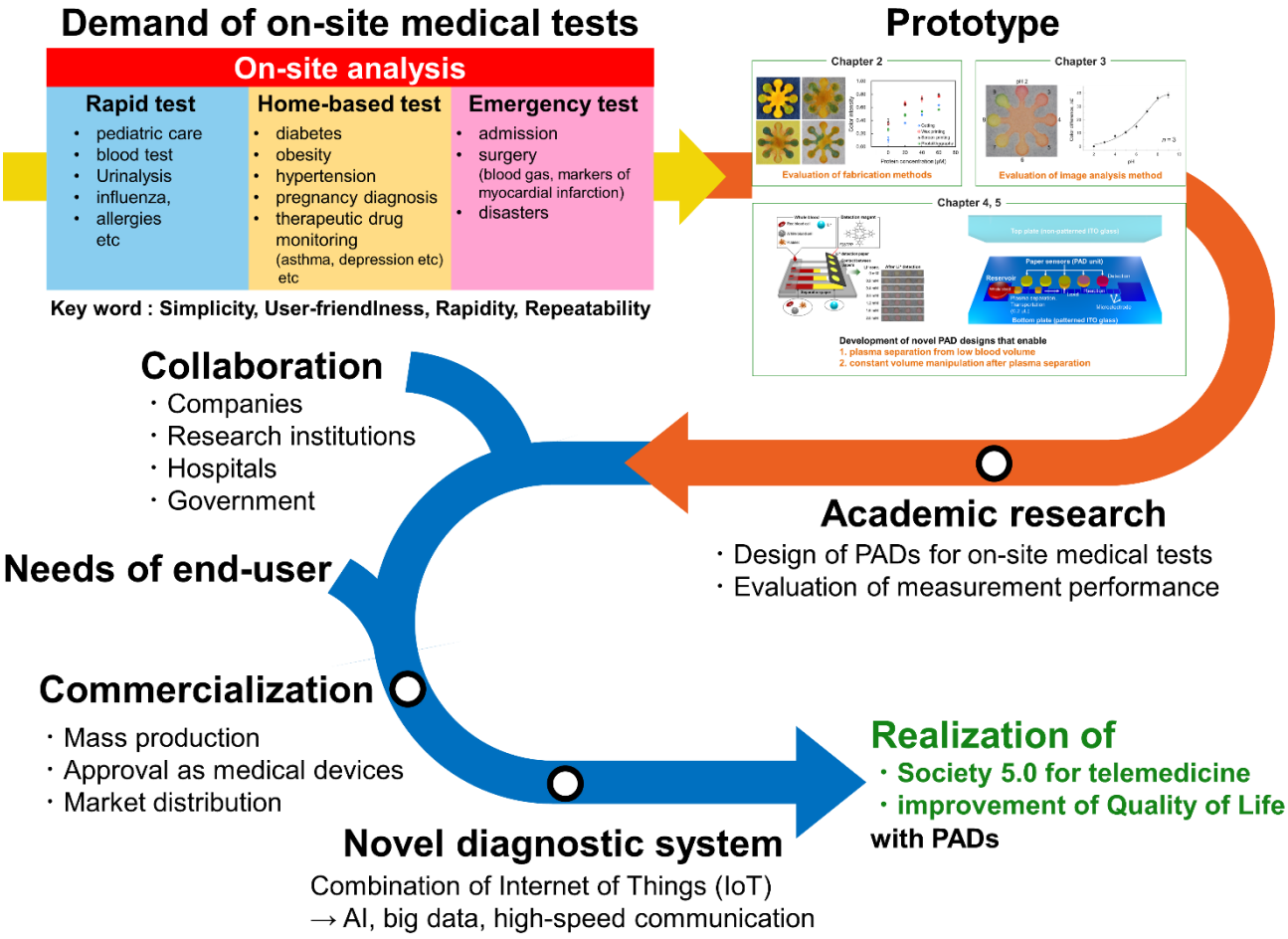

Fig. 6.1 Illustration of the future prospects of PADs.

List of Publications

[1] Lori Shayne Alamo Busa, **Takeshi Komatsu**, Saeed Mohammadi, Masatoshi Maeki, Akihiko Ishida, Hirofumi Tani and Manabu Tokeshi, 3,3',5,5'-Tetramethylbenzidine Oxidation on Paper Devices for Horseradish Peroxidase-Based Assays, *Analytical Sciences*, 32, 815-818 (2016). https://doi.org/10.2116/analsci.32.815

[2] **Takeshi Komatsu**, Saeed Mohammadi, Lori Shayne Alamo Busa, Masatoshi Maeki, Akihiko Ishida, Hirofumi Tani and Manabu Tokeshi, Image Analysis for Microfluidic Paper-Based Analytical Device Using the CIE *L*a*b** Color System, *Analyst*, 141, 6507-6509 (2016). https://doi.org/10.1039/C6AN01409G

[3] **Takeshi Komatsu**, Masatoshi Maeki, Akihiko Ishida, Hirofumi Tani and Manabu Tokeshi, Characteristics of Microfluidic Paper-Based Analytical Devices Fabricated by Four Different Methods, *Analytical Sciences*, 34, 34-39 (2018). https://doi.org/10.2116/analsci.34.39

[4] Yu Hiroki, **Takeshi Komatsu**, Youka Bunno, Takuro Tsutsumi and Yudai Ogawa, A Report of the Science Experimental Lecture at Okinawa Institute of Science and Technology Graduate University: pH Measurement Experiment Using Paper Device, *Japanese Journal of Science Communication*, 26, 17-28 (2020). http://doi.org/10.14943/92750

[5] **Takeshi Komatsu**, Masatoshi Maeki, Akihiko Ishida, Hirofumi Tani and Manabu Tokeshi, Paper-Based Device for Facile Colorimetric Determination of Lithium-Ion in Human Whole Blood, *ACS Sensors*, 5, 1287-1294 (2020). https://doi.org/10.1021/acssensors.9b02218

[6] **Takeshi Komatsu**, Yuki Sato, Masatoshi Maeki, Akihiko Ishida, Hirofumi Tani and Manabu Tokeshi, Rapid, Sensitive Universal Paper-Based Device Enhances Competitive Immunoassays of Small Molecules, *Analytica Chimica Acta*, 1144, 85-95 (2021). https://doi.org/10.1016/j.aca.2020.12.003

[7] **Takeshi Komatsu**, Ryoga Maeda, Masatoshi Maeki, Akihiko Ishida, Hirofumi Tani and Manabu Tokeshi, Dip-Type Paper-Based Analytical Device for Straightforward Quantitative Detection without Precise Sample Introduction, *ACS Sensors*, accepted (2021).

[8] **Takeshi Komatsu**, Manabu Tokeshi and Shih-Kang Fan, Determination of Lithium Ion with Digital Microfluidic Whole Blood Separation and Preloaded Small Paper Sensors, submitted.

[9] **Takeshi Komatsu**, Ryan Russel Gabatino, Harrienica Hofileña, Masatoshi Maeki, Akihiko Ishida, Hirofumi Tani and Manabu Tokeshi, Paper-Based Device Format for Simple Quantitative Colorimetry without Micropipettes Toward Online and Field Studies, submitted.

[10] **Takeshi Komatsu**, Osamu Wakao, Masatoshi Maeki, Akihiko Ishida, Hirofumi Tani and Manabu Tokeshi, Development of Microfluidic Device Integrated with Pillar Structures Enabling Precise Volume Dispensing of Liquid Samples for Therapeutic Drug Monitoring, *Proceedings of Microprocesses and Nanotechnology Conference 2017*, 1, 8P-7-68 (2017).

[11] **Takeshi Komatsu**, Manabu Tokeshi and Shih-Kang Fan, Micro Total Analysis System for Lithium Ion in Human Whole Blood with Hybrid Device of DMF and Tiny Paper Sensors, *Proceedings of Micro Total Analysis System 2019*, 1, 84-85 (2019).

[12] **Takeshi Komatsu**, Masatoshi Maeki, Akihiko Ishida, Hirofumi Tani and Manabu Tokeshi, Novel Format of a Paper-Based Device for Competitive Immunoassays, *Proceedings of Micro Total Analysis System 2020*, 1, 494-495 (2020).

Patent

[1] Detecting Device of Molecules,

Manabu Tokeshi, Akihiko Ishida, Takeshi Komatsu, Yuki Sato, JP2018-142651.

Acknowledgement

This thesis is the result of the author's research in the Bioanalytical Chemistry Laboratory, Graduate School of Chemical Sciences Engineering, Hokkaido University. Getting to this point in my life would have been impossible without the many important people who have supported me along the way. My deepest gratitude goes out to all of them.

First, I would like to express my sincerest respect and gratitude to my supervisor, Professor Manabu Tokeshi of the Division of Applied Chemistry, Faculty of Engineering, Hokkaido University for his guidance and wisdom, meaningful advice, and continuous support and encouragement as I took on the challenges of pursuing my Ph.D. degree. He imparted to me perspectives regarding not just research, but also life. I doubt that I will ever be able to convey my appreciation fully but I owe him my eternal gratitude.

I am deeply grateful and proud that I am part of the Bioanalytical Chemistry Laboratory (Tokeshi Lab). I am especially grateful to Associate Professor Hirofumi Tani, Assistant Professor Akihiko Ishida, and Assistant Professor Masatoshi Maeki of the lab for all the assistance, advice, and valuable discussions. Very special thanks go out to Prof. Ishida for providing me with his precious advice and father-like words. Also, very special thanks go to Prof. Maeki for providing me with his precious technical advice and our journeys together to many academic conferences.

I would like to acknowledge Associate Professor Hirofumi Tani and Professor Toshifumi Satoh of Faculty of Engineering, Hokkaido University, and Professor Kazuki Sada of the Faculty of Science, Hokkaido University for accepting the responsibility of being my official co-supervisors.

For his extraordinary technical advice and collaboration in this research, I must acknowledge Professor Shih-Kang 'Scott' Fan of the Department of Mechanical and Nuclear Engineering, Kansas State University, USA. He provided me with precious technical advice concerning digital microfluidics, which is the essence of this research and thus I am deeply grateful to him.

I would also like to thank my lab-mates in the National Taiwan University, Ms. Chia-Chann Shiue (Ph. D), Ms. Szu-Chia Hsieh (Ph.D.), Mr. Chiang-Yu Chien Ph. D), Mr. Jyong-Huei Lee, Mr. Jing-Zhe Gao, Mr. Jia-Tai Liao, Mr. Siang-Lin Wang, Mr. Kai-Mao Cheng, Mr. Kuan-Lun Ho, Mr. Yu-Hsuan Yang, Mr. Shaw-Yuan Fang, Mr. Chu-Chi Lin, Mr. Ding-Yang Tsai, Mr. Sheng-Jie Jian, Mr. Sheng-Chun Lin, Mr. Jia-Lian Cheng, Ms. Tzu-Hsuan Huang, and Mr. Hong-Yu Liao of Fan-tasy Lab in Taiwan. Ms. Chia-Chann Shiue, Mr. Chien-Chiang Yu, and Mr. Chu-Chi Lin supported my study abroad in Taiwan and made my Taiwanese life especially happy. I also extremely grateful for my good relationship with my other lab-mates in my daily life in Taiwan and I wish them future happiness and research success.

I would like to acknowledge the Grant-in-Aid for the Japan Society for the Promotion of Science Fellows, Overseas Challenge Program for Young Researchers for the Japan Society for the Promotion of Science, cotutelle program signed between National Taiwan University and Hokkaido University, and also acknowledge the support by the Ambitious Leaders' Program for Fostering Future Leaders to Open New Frontiers in Materials Science for Hokkaido University.

Through my research, I attended many academic conferences. Thanks to all professors, students, and participants, I received great stimulation and experiences through conference presentations and traveling for international conferences. Especially, my deep thanks to each member of the Baba Lab of Nagoya Nagoya University, Kitamori Lab of the University of Tokyo, Hisamoto Lab of Osaka Prefecture University, Xu Lab of Osaka Prefecture University, and to so many people with whom we had delightful dinners; these are lovely memories of the conferences.

I would also like to thank my lab-mates, Nishiyama and Niko, who worked together in the lab like brothers and made my lab life especially happy, along with Yuto Kikuchi, Seiya Nakamata, Daichi Fujii, Shohei Yamazaki, Taiga Ajiri, Yuusuke Nakatani, Osamu Wakao, Donny Nugraha Mazaafrianto, Lori Shayne A. Busa, Saeed Mohammadi, Yuka Fujishima, Fumiya Sakai, Kastuki Fukamachi, Kota Kikuchi, Yuki Kudo, Saya Sato, Ryohei Mizukami, Yi Bao, Yuri Moratelli Piske, Shingo Ikeda, Kazuki Shimizu, Ayano Nakamura, Koki Hoshikawa, Yang Yi, Issei Takata, Reo Takeda, Takuma Nishimura, Ryoga Maeda, Po-Sheng Chen,

Akinori Yamaguchi, Yuka Matsuura, Yuto Okada, Shizuka Kuki, Kazuki Takahashi, Yasunobu Nonaka, Tomoaki Funakubo, Syuya Uno, Asuka Koza, Rikuro Saiki, Ayuka Niwa, and our lab secretaries Michiko Tani-San and Kokoro Haruki-San.

I would like to thank all my friends who have made me think of Hokkaido as a second home. Finally, I would like to offer a big thank you to my family. My family provided me with the opportunity to study far from my original hometown and my family continuously supported me.